

Alma Mater Studiorum – Università di Bologna

DOTTORATO DI RICERCA IN

Meccanica e scienze avanzate dell'ingegneria

Ciclo XXXII

**Settore Concorsuale: 09/A1**

**Settore Scientifico Disciplinare: ING-IND/06**

High Reynolds Number Experiments in the Long Pipe at CICLoPE

**Presentata da:** Lucia Mascotelli

**Coordinatore Dottorato**

**Supervisore**

**Marco Carricato**

**Alessandro Talamelli**

**Esame finale anno 2020**

©Lucia Mascotelli 2020

Lucia Mascotelli 2020, **High Reynolds Number Experiments in the Long Pipe at CICLoPE**

Università di Bologna, Scuola di Ingegneria e Architettura, 47121 Forlì, Italy

## Abstract

In aerospace applications 50% of the drag is due to the friction experienced in the turbulent boundary layer. In a perspective of drag reduction, it is important to rely on numerical codes accurate enough to correctly predict friction. The logarithmic-law, the wall function describing the flow in the near-wall region, and in particular its governing parameter  $\kappa$  (Von Kármán constant), are still object of intense debate. If throughout the years a consensus on the value of  $\kappa$  for pipes has been reached around the value of 0.39, the same for other canonical flows, the matching of wake discussed by Coles, has not received the attention it deserves for its high impact on friction prediction. It requires that, given the evolution of the centerline velocity over a range of Reynolds numbers described by the logarithmic law  $U_{CL}^+ = 1/\kappa_{CL} \ln(Re_\tau) + C$ , with  $\kappa_{CL}$  being its Von Kármán constant,  $\kappa = \kappa_{CL}$ . The requirement is violated for pipes, where  $\kappa_{CL}$  has consistently remained higher than 0.42, a behaviour not accounted for in numerical models. This thesis is aimed at shedding light on the anomalies in the estimation of  $\kappa_{CL}$ . Centerline measurements were performed in Long Pipe at CICLoPE in a Reynolds number range from  $8.1 \times 10^3$  to  $3.9 \times 10^4$ , together with a detailed uncertainty analysis. Guaranteeing the highest accuracy experimentally available, the Long Pipe is perfectly suited to assess if the observed differences between  $\kappa$  and  $\kappa_{CL}$  are due to experimental uncertainties, as believed so far, or rooted in physics. As matter of facts, the controversies around the correct value of  $\kappa_{CL}$  might be due to an incomplete knowledge of the physical phenomena occurring inside the boundary layer. Despite being quintessentially chaotic, it hides a hierarchy of different-size eddies whose interaction are still not clear but challenges the classical view. Single-wire measurements were performed at 5 Reynolds numbers in the range from  $9.9 \times 10^3$  to  $3.9 \times 10^4$ , covering wall-normal distances from beneath the variance inner-peak ( $y^+ \approx 10$ ) up to  $y/R \approx 0.93$ . First, the inner-scaled variance is analysed. After confirming the Reynolds dependence, not contemplated in the classical turbulence theory, the contributions to the broadband turbulence intensity for the different scales is quantified. Using a spectral cut-off filter, the large scales showed a growing streamwise variance with increasing Reynolds numbers, while the small scales exhibited the universality stated by the classical theory. 2-point measurements, fixing a single-wire probe at the edge of the log-region at  $y/R \approx 0.2$  and making another one covering the distance from the wall, allowed to investigate the nature of the turbulent eddies. The wall-attached and self-similar behaviour postulated by the Townsend's attached eddy hypothesis is observed for the coherent structures, characterised by an aspect ratio of  $\approx 20$ .

**Key-words:** Wall turbulence, pipe flow, high Reynolds number, hot-wire, coherent structures, logarithmic law, von Kármán constant, friction.

# Contents

## Abstract

<b>Chapter 1. Introduction</b>	1
1.1. Background	1
1.2. Present work: objective and outline of the thesis	5
<b>Chapter 2. Theoretical background</b>	1
2.1. Statistical principles	1
2.1.1. Velocity averaging	1
2.1.2. Probability density function	2
2.1.3. Statistical moments	3
2.1.4. Correlations	4
2.1.5. Taylor's hypothesis	6
2.1.6. Spectral analysis	6
2.2. Pipe flow	11
2.3. Wall-bounded flows	13
2.3.1. Turbulence scaling and mean velocity profile	13
2.4. The scales of turbulence	17
2.5. Hot-wire anemometry	18
2.5.1. Basic principles	19
2.5.2. Limitations	21
2.6. Background	23
2.6.1. The log-law	23
2.6.2. Organised motions in turbulence	25
2.6.3. Attached eddy model	27
2.6.4. Interaction of turbulence scales	30
<b>Chapter 3. Facility and experimental set-up</b>	33
3.1. The need of a high Reynolds facility	33

3.2. General construction	35
3.3. Instrumentation	36
3.3.1. Hot-wire anemometry	40
<b>Chapter 4. Scaling of centerline velocity</b>	<b>43</b>
4.1. Experimental set-up	43
4.1.1. Choice of the ports	43
4.2. Centerline velocity measurements	45
4.2.1. Pitot probes	47
4.3. Uncertainty analysis	53
4.3.1. Experimental data	53
4.3.2. Influence of transducer accuracy and Reynolds number range	61
<b>Chapter 5. Structures interaction</b>	<b>71</b>
5.1. Experimental set-up	71
5.2. Filtering procedure	72
5.3. Correction scheme	76
5.4. Data validation	79
5.5. Small-scale variance	81
5.6. Large-scale variance	84
<b>Chapter 6. Linear Coherence Spectra analysis</b>	<b>89</b>
6.1. Experimental set-up	89
6.2. Linear coherence spectrum	90
6.3. The influence of probe distance	91
6.4. Influence of Reynolds number	97
<b>Chapter 7. Conclusions</b>	<b>101</b>
<b>Acknowledgements</b>	<b>106</b>
<b>Bibliography</b>	<b>108</b>





## CHAPTER 1

# Introduction

### 1.1. Background

In the classic text "An introduction to turbulence and its measurements", Peter Bradshaw defined turbulence as "*the most common, the most important and the most complicated kind of fluid motion*" (Bradshaw 1971). Everyone is in fact familiar with the wake behind a boat, the smoke coming out of a chimney or the clouds passing in the sky on a windy day. Everyone has at least once taken the plane, driven a car or sat on a train: their fuel consumption is directly influenced by turbulence itself. Turbulence is ubiquitous in numerous industrial applications, such as nozzles, pipelines, heat exchangers, combustion engines and turbo machinery, but not only. Turbulence characterises also many natural mechanisms, such as the dynamics of the atmosphere (think about the distribution of air pollution, linked to turbulent diffusion), of the oceans or astrophysical phenomena, like planetary interiors for example.

The first systematic study on the onset of turbulence dates back to 1883, when Osborne Reynolds performed the first observations. With his pioneering experiment, he observed the transition to turbulence of water flowing inside a glass pipe, using black ink as tracer. He discovered that the process of transition is governed by a specific dimensionless parameter, later named Reynolds number and defined as:

$$Re = \frac{UL}{\nu} \quad (1.1)$$

where  $U$  is the flow velocity,  $L$  the characteristic length and  $\nu$  the kinematic viscosity of the flow considered. As the Reynolds number increases past a critical value (*critical Reynolds number*), the flow becomes more and more turbulent.

Despite being object of noticeable research effort for more than a century, its wide application and its everyday-life importance, many questions regarding turbulence are left unanswered and the theory behind it is still not so trivial. First, it still lacks a clear-cut definition: it appears as an irregular three-dimensional system of eddies of different sizes continuously growing and interacting with each other. In particular, high Reynolds numbers wall-bounded turbulence is characterised by an incredibly wide variety of scales, ranging from

the big eddies, whose size is fixed with the external geometry and are dominated by inertial forces, to the smallest eddies, dominated by viscosity instead. Differently from the largest scales, the smallest ones, called *Kolmogorov scales* from the scientist who first theorised them in 1941, have a size that is not fixed with geometry. As matter of facts, the variety of turbulent scales and dimensions vary with the Reynolds number: as it increases, the dissipation scales become smaller and smaller compared to the large ones. This phenomenon, characteristic of the high Reynolds number regimes, is called scale separation. The interaction between the scales is particularly crucial for turbulence to be sustained, according to the classical turbulence theory: energy must be fed to the largest scales from the mean flow, and transferred to the smaller eddies in a mechanism called energy cascade. This process continues until the viscous effects dominate over the inertia: the smaller eddies reach their minimum size and turbulent kinetic energy starts to dissipate into heat.

Additional difficulties are due to the dynamics of turbulence, so rich and complex that a detailed understanding of turbulent flows and a prediction of their behaviour is nowadays only possible for extremely simplified cases, often obtained with unrealistic assumptions. This is a consequence of the so-called *closure problem* of turbulence. The behaviours of all fluid flows are, as matter of facts, embodied by the Navier-Stokes equations, a set of non-linear partial differential equations very difficult to solve with only few exact solutions for simplified cases, as previously mentioned. As the governing equations are averaged with the traditional approach of the Reynolds averaging, the nonlinear terms give rise to new terms aside the mean velocity component and the mean pressure. This leads to an unbalanced system (with more unknowns than equations), since for every equation derived for each additional unknown, more variables appear. In other words, a complete statistical description of turbulence requires an infinite numbers of equations. Only numerically, with the Direct Numerical Simulations (DNS), the Navier-Stokes equations can be fully solved without invoking any sort of simplification. Unfortunately, available technology is still not powerful enough to solve cases that can be interesting from the engineering point of view, namely complex geometries and high Reynolds numbers regimes (think of the air flowing past the wing of an airplane). High Reynolds number turbulent regimes are not interesting only for industrial applications, but also theoretically since most of widely accepted results on turbulence are valid in the infinite Reynolds number limits. Therefore, gaining a deeper insight on the physics underpinning the high Reynolds numbers flows, has a two-fold advantage. First, it will lead to general conclusions about the behaviour of turbulent flows, their nature and dynamics. Secondly, it will benefit the development of more accurate models and predictions, favouring a great variety of applications, for instance, friction control.

Friction becomes particularly interesting when the flow interacts with one or more surfaces. In the case of wall-bounded turbulent flows, in fact, turbulence is produced in a thin layer attached to the wall, whose existence was first suggested by Prandtl in 1904: the boundary layer. In this region, where viscous effects are dominant, the fluid's velocity will quickly decrease to zero as the wall is approached. Despite being very thin, the importance of the boundary layer is unequivocal, since it is where the friction between the wall and the fluid starts to develop. Friction is not only the main responsible for energy consumption in the vast majority of everyday cases, but also the driving mechanism of wall-bounded turbulence, making it a key parameter for the scaling of this type of flows. Therefore, it is clear how a deep understanding of the phenomena occurring inside the boundary layer have great consequences on key topics, like drag reduction. As matter of facts, in aerospace applications, where the Reynolds numbers are high and the boundary layer developing on the surface is turbulent, the theme of drag reduction is particularly relevant. For instance, at subsonic cruising speed, around 50% of the total drag experienced by an aircraft during landing or take-off, is due to friction, and this figure can go up to 70% when considering cruise. This figure makes friction the main responsible not only of fuel consumption, but consequently for the total emissions dispersed in the atmosphere. In terms of topical interests, saving 1% in friction may save a typical long-range aircraft 4000000 litres of fuel per year. This will benefit not only the financial side, but also the environmental one, with 5000 kg less of emissions produced. In a context where we are asked to reduce by 40% the CO<sub>2</sub> emissions by 2030, it is of foremost importance to delve into the physical root of friction. On one hand, this will boost the development of devices and technologies aimed at friction control. On the other, it will improve the accuracy of the models used for friction prediction.

Nowadays friction is predicted using numerical codes. Although the undeniable advantage of DNSs to solve up to the finest spatial and temporal scales without making any simplifying assumption, the grid points needed as the Reynolds number increases, make them incredibly time-consuming and cost-effective. Therefore, nowadays it is preferred to use numerical approaches such as the Reynolds-averaged Navier-Stokes (RANS) and Large-Eddies simulations (LES) based on wall-functions to approximate the behaviour of the flow in the near-wall region. The wall-functions are governed by parameters whose values are set by classical theory. In the particular case of wall-bounded turbulent flow, the most widely accepted equation governing the mean-flow behaviour in the near-wall region, has a logarithmic form and its characterising parameter is  $\kappa$ , the Von Kármán constant, typically set at 0.40 by classical turbulence theory, regardless of the flow considered.

As the measuring techniques and the computational power has evolved, it seems that the consensus on the universal nature of  $\kappa$  has been lost. It has been suggested (Nagib and Chauhan 2008) that  $\kappa$  has different values for different

geometries and pressure gradients. The exact value of  $\kappa$  will greatly affect the power of friction prediction in wall-bounded flows. As matter of fact, the value of this parameter is delicate to the extent that a variation of 6% in  $\kappa$  would lead to errors up to 2% in the prediction of skin friction coefficient (Smits, McKeon, and Marusic 2011).

The accuracy to determine the constants of the log-law depends on two factors. First, a higher Reynolds number allows a larger extent of the logarithmic region, simplifying the estimation of the parameter. Second, it depends on how accurately we can measure the friction velocity  $u_\tau$ , a key parameter for the scaling of the variables in the log-law. In the case of boundary layer, the procedure to measure the friction velocity involves indirect methods, such as oil-film interferometry, at the expenses of the accuracy of the results. On the other hand, in pipe and channel flows the wall friction can be estimated just by acquiring the static-pressure drop, guaranteeing a greater precision. Therefore, highly accurate measurements in the high Reynolds numbers regime are key to assess if the observed differences are due to uncertainties or are rooted in physics. Clarifying the anomalies encountered in the estimation of  $\kappa$  can not disregard a thorough description of the phenomena occurring inside the turbulent boundary layer. This is not a trivial task, since the physics underpinning the turbulent boundary layer is complex.

Despite being quintessentially chaotic, it hides a hierarchy of structures whose dynamics is still not completely clear. These structures typically develop in the streamwise direction for distances of the order of magnitude of the boundary layer thickness (large-scale motions or LSM) or 10 times that (very-large-scale motions or VLSM) and are seen to be one of the major contributors to friction production (Ganapathisubramani et al. 2005). To add complexities to an already rich dynamics, the LSMs interact with the small-scale structures inhabiting the near-wall region, superimposing their energy (Marusic and Kunkel 2003), challenging again the classical turbulence theory that does not take this interaction into account. Hence, characterising the dynamics and the nature of the LSMs and VLSMs is key to deepen the knowledge about the phenomena in the boundary layer, especially those ones connected to friction production, and therefore useful to shape new control technologies.

For these reasons, the Long Pipe at the CICLoPE (Centre for International Cooperation for the Long Pipe Experiment) laboratory is particularly suited for investigating these kind of problems, where high resolution and high Reynolds numbers need to coexist. As extensively reported in Talamelli et al. 2009, the fundamental idea behind the construction of this facility is to achieve high Reynolds by an increase of  $L$  (in eq.(1.1)) instead of the flow speed  $U$  or the density, as opted in other facilities. The creation of a large-scale facility, with a 111.5 m long test section and 0.9 m diameter, allowed to explore the high Reynolds numbers regime while fully resolving all turbulent scales by using standard tool of measurements, such as hot-wires, limiting the spatial resolution

issues, which is a common problem encountered when measuring at high  $Re$ . Given a fixed size experiment, the large scales will keep their size, fixed by the external geometry, while the small scales will grow smaller as the Reynolds number increases. Eventually, they will become smaller than the sensing length of the instrument, causing an artificial attenuation of the small-scale turbulent fluctuations. Given the size of the facility, finding a convenient location was challenging. The two tunnels of the ex-Caproni industry in Predappio, were found to be a very suitable installation.

### 1.2. Present work: objective and outline of the thesis

A more detailed delineation of the objectives of this thesis can be now outlined. In order to investigate the high Reynolds numbers regimes of topical interest for a wide range of applications, the experimental approach is the only option available. The intrinsic challenges, specifically guaranteeing a good spatial resolution for the whole range of  $Re$  investigated, are overcome by the unique characteristics of the Long Pipe that allow the use of standard hot-wire anemometry. The general aim of this investigation is to highlight some of the physical phenomena occurring in a fully developed turbulent pipe flows, in particular those that are related to friction prediction. Deepening the knowledge on such phenomena, characterised by a complex dynamics, is especially useful when developing friction control technologies. In particular the objective of the thesis can be classified as follows:

- **Estimate of the von Karman constant at the centerline.** A key input of the CFD models to predict friction for wall-bounded turbulent flows is the von Kármán constant,  $\kappa$  and the logarithmic-law it governs. The von Kármán parameter is set as constant (typically around 0.40) and universal by classical turbulence theory. Moreover, the asymptotic matching of the wake, in other words extending the log-law to the centerline of the pipe governed by  $\kappa_{CL}$ , requires  $\kappa_{CL} = \kappa$ . This is in contrast with experimental evidence, and therefore high-resolution data are needed to understand if this difference is rooted in physics or just due to experimental uncertainty, given the high impact it has on friction prediction. The main objective is to accurately estimate  $\kappa_{CL}$  for a fully developed turbulent pipe flow, to verify its statistical difference from  $\kappa$ .
- **Investigate the interaction between small- and large scales.** Recent numerical and experimental work show a failure of the classical scaling of streamwise turbulence intensity, highlighting a Reynolds number dependence that suggests an interaction between the turbulent scales. In this work we want to show that the growth of the near-wall turbulence intensity, with increasing Reynolds number, is in fact due to an increasing energy of the large scales, while the small-scale structures still follow the classical scaling. Moreover, if the behaviour of the large-scale structures in the outer region can be somehow related to their behaviour near

the wall, quantities in this region could be estimated by measuring in much more accessible locations (like the outer region). The challenge here is to provide high resolution data, since small-scale fluctuations in the near-wall region can be source of spatial resolution issues.

- **Assessment of turbulent pipe flow coherent structures.** Starting from Townsend's attached eddy hypothesis, the self-similar and wall-attached nature of the turbulent structures coherent with the near-wall region is investigated through a spectral analysis. The method is applied to a set of data resulting from simultaneous acquisition from two single-wire hot-wire probes; one is fixed at the edge of the log-region while the other is spanning the distance from the wall.

The thesis is outlined as follows: after a brief overview on the theoretical background and state of the art, presented in Chapter 1, the mathematical tools and fundamental equations for the fully developed turbulent pipe flows are given in Chapter 2. Chapter 3 is instead focused on the characteristics of the CICLoPE laboratory and a detailed description of the experimental set-up and instruments used during the experimental campaigns. Chapter 4 presents the results on the centerline measurements to estimate  $\kappa_{CL}$ . In Chapter 5 the interaction between the scales is investigated, while their coherence in Chapter 6. In Chapter 7 the main conclusions of the thesis are summarised.

## CHAPTER 2

### Theoretical background

The following chapter consists in of an explanation of the mathematical definitions and statistical tools used throughout the thesis. A brief overview of the classical theory for wall-bounded turbulence will follow, along with a description of the basic physics principles underpinning the measurements techniques. In conclusion, the main objectives of the thesis will be outlined.

#### 2.1. Statistical principles

Although a full characterisation of wall-bounded turbulent flows is still impossible, historically, the statistical approach has been taken to investigate this type of flow. Its complex dynamics, as matter of facts, can be accurately described as a purely random process. The statistical tools used to characterise the turbulent flow are provided in this section.

##### 2.1.1. Velocity averaging

A turbulent flow is often described as a random and fluctuating flow state. Therefore, the instantaneous velocity  $U_i(\mathbf{x}, t)$  is usually separated into its mean and fluctuating part:

$$U_i(\mathbf{x}, t) = \langle U_i \rangle(\mathbf{x}, t) + u_i(\mathbf{x}, t) \quad (2.1)$$

Referred to as the Reynolds decomposition. Here,  $U_i(\mathbf{x}, t)$  is the  $i$ -th component of the instantaneous velocity  $U(\mathbf{x}, t)$ , function of time and position  $\mathbf{x} = (x, y, z)$ ,  $u_i(\mathbf{x}, t)$  is its fluctuating part and  $\langle U_i \rangle(\mathbf{x}, t)$  its mean. In turbulent flows simulations and experiments multiple kinds of *averaging* are used to compute the mean value of a quantity. For flow conditions that can be replicated  $N$  times, the correct way to retrieve the mean would be by performing an *ensemble average*, i.e. the set of samples is obtained from performing the same exact experiment for  $N$  times. This means that if we want to completely characterise the velocity in one point in space,  $\mathbf{x}$  at time  $t$ , we should repeat several experiments with the same boundary and initial conditions, and each time we should measure at the same desired location  $\mathbf{x}$  at the same instant  $t$  from the start of the experiment. In this way, the velocity ensemble average at position  $\mathbf{x}$  and time  $t$  is computed as:

$$\langle U_i \rangle (\mathbf{x}, t) \equiv \frac{\sum_{j=1}^N U_{i,j}(\mathbf{x}, t)}{N} \quad (2.2)$$

Where  $U_{i,j}(\mathbf{x}, t)$  is the  $i$ -th component of the instantaneous velocity measured at the  $j$ -th realisation, at the same time and position,  $N$  the total number of experiment realisations. However, in practice the time series at the desired location is measured during one single experiment, with the assumption that the flow is *statistically stationary*. This means that the statistics of the variable are constant in time, and that the *ensemble average* is equal to the time average, i.e. averaging over the number of realisations leads to the same result as averaging over time. Therefore, for a statistically stationary turbulent flow, the mean part of the velocity component  $U_i(\mathbf{x}, t)$  is defined as the temporal mean and identified here with an overbar,  $\overline{U}_i(\mathbf{x})$ :

$$\overline{U}_i(\mathbf{x}) = \langle U_i \rangle (\mathbf{x}) = \frac{1}{T} \int_0^T U_i(\mathbf{x}, t) dt \quad (2.3)$$

Where  $T$  is the sampling time. The statistics shown throughout the thesis will be based on time averages.

### 2.1.2. Probability density function

In the case of laminar flow, to compute the velocity component  $U$  at a certain time and space, it is possible to completely rely on theory, i.e. the Navier-Stokes equations, knowing that the result will agree to what is obtained experimentally. For turbulent flows, theory can only estimate that value with a certain degree of accuracy, given the unpredictable nature of the flow itself. Therefore we aim at determining the *probability* of an event to occur, such as  $A \equiv \{U < 10\}$  m/s.

The probability  $p$  of an event  $A$  is, for example:

$$p = P(A) = P\{U < V_a\} \quad (2.4)$$

where, intuitively,  $p$  is a real number included in the range  $[0;1]$  that represents the likelihood for the event  $A$  to occur (in the case above of the random velocity variable  $U$  to assume values lower than  $V_a$ ). For an impossible event  $p = 0$ , whilst  $p$  is set to unity for a sure event.

The probability of any event can be inferred from the *cumulative distribution function* (CDF). The CDF of a random variable  $U(t)$  represents the probability for  $U(t)$  to take on a value lower or equal to  $V$ :

$$F(V) = P(U(t) < V) \quad (2.5)$$

From the definition, for every  $U(t)$ , every cumulative distribution function has the following properties:  $F(-\infty) = 0$ ,  $F(+\infty) = 1$ . Since the probability

of any event is non-negative, the probability the random variable has to take on a value between  $V_a$  and  $V_b$ , with  $V_a < V_b$ , is expressed as:

$$P(V_a < U(t) < V_b) = F(V_b) - F(V_a) \geq 0. \quad (2.6)$$

Now, the *probability density function* (PDF) can be defined as:

$$f(U) = \frac{dF(U)}{dU} \quad (2.7)$$

and from the properties of the CDF it follows that the PDF is non-negative:

$$f(U) \geq 0 \quad (2.8)$$

and it satisfies the normalisation condition:

$$\int_{-\infty}^{+\infty} f(U)dU = 1. \quad (2.9)$$

The PDF fully characterise the random variable  $U(t)$ , meaning that if the PDF (or equally the CDF) of a random variable is known, then also the  $n$ -th order moment is.

### 2.1.3. Statistical moments

The first-order moment of a random variable  $U$  is the *mean*, defined as:

$$\langle U \rangle = \int_{-\infty}^{+\infty} U f(U) dU \quad (2.10)$$

It represents the probability-weighted average of all the possible values that  $U$  can take on.

Once the mean is defined, it is possible to introduce the *fluctuation* in  $U$ :

$$u = U - \langle U \rangle \quad (2.11)$$

Since the mean of the fluctuations is always zero, higher order moments are introduced to further describe the flow from the statistical point of view. The second-order moment is the *variance*, defined as the mean-square fluctuation:

$$\text{var}(U) = \langle u^2 \rangle = \int_{-\infty}^{+\infty} u^2 f(U) dU \quad (2.12)$$

The square-root of the variance is the *standard deviation*, or *root-mean square* of  $U$ :

$$\sigma_u = \sqrt{\langle u^2 \rangle} \quad (2.13)$$

It quantifies the intensity of the typical fluctuations. Likewise, the  $n$ -th central statistical moment can be defined as:

$$\langle u^n \rangle = \int_{-\infty}^{+\infty} u^n f(U) dU \quad (2.14)$$

The first and second moments have obvious importance for the characterisation of the flow state, but also the third and fourth moments are often considered. They are usually normalised with the appropriate power of the standard deviation:

$$S_u = \frac{\langle u^3 \rangle}{\sigma_u^3} \quad (2.15)$$

$$F_u = \frac{\langle u^4 \rangle}{\sigma_u^4} \quad (2.16)$$

Called *skewness* and *flatness* or *kurtosis* respectively. The skewness and flatness describe particular characteristics of the PDF. The skewness is an indicator of the symmetry of the PDF: a zero skewness describes a symmetric distribution like the Gaussian, while it becomes positive if the PDF is shifted towards values that are larger than the mean, and lower than the mean if negative. The flatness, as the name suggests, is a measure of how peaked or flat the PDF is. For reference, a Gaussian distribution has  $F_u = 3$ .

#### 2.1.4. Correlations

In the first section of this chapter it was emphasised that the PDF fully characterise a random variable. At each instant in time, the random variable  $U(t)$  is characterised by its PDF as:

$$f(U) = \frac{dF(U)}{dU} \quad (2.17)$$

However, this quantity does not contain any information about the statistical relations of  $U(t)$  at two different points in the flow; indeed two random processes with the same one-time PDF can be have a radically different behaviour statistically. For this reason, multi-time and space statistics are used to characterise the process. The correlation between the process in a given point in space  $\mathbf{x}$  at two different instants,  $t$  and  $t + \tau$  is the *autocovariance*. Hence, the autocovariance indicates how quickly the process forgets its past behaviour at that particular point

$$R(\mathbf{x}, \tau) = \langle u(\mathbf{x}, t)u(\mathbf{x}, t + \tau) \rangle \quad (2.18)$$

Where  $\tau$  is the *lag time*. In the case of a statistically stationary process, all the statistics are independent of time, therefore the only important parameter

when determining the autocovariance is the time-lag  $\tau$ . When the time lag is 0, the variance is retrieved. The autocovariance is usually normalised with the variance, obtaining the *correlation function*:

$$\rho(\mathbf{x}, \tau) \equiv \frac{\langle u(\mathbf{x}, t)u(\mathbf{x}, t + \tau) \rangle}{\langle u(\mathbf{x}, t)^2 \rangle} \quad (2.19)$$

it represents the correlation coefficient between the process in the point  $\mathbf{x}$  at the two instants  $t$  and  $t + \tau$ . If the correlation is equal to 0, it means that the fluctuations at  $t$  and  $t + \tau$  are no longer correlated. Consequently, the following properties are valid:

$$\rho(0) = 1 \quad (2.20)$$

$$|\rho(\tau)| \leq 1 \quad (2.21)$$

For the processes characterising turbulent flows, as the lag-time increases, the correlation is expected to decrease. This trend is quickly enough for the integral:

$$\Lambda_t \equiv \int_0^{+\infty} \rho(\tau) d\tau \quad (2.22)$$

to converge, defining  $\Lambda_t$  as the *integral time scale*.

If instead we consider multi-space and single-time statistics, such as fluctuations from different points in space but measured at the same instant in time, the same considerations done so far can be applied using space as the parameter. It is particularly useful when investigating turbulent structures developing in space. Hence, the statistical properties become:

$$R_u(\mathbf{x}, \mathbf{r}) \equiv \langle u(\mathbf{x}, t)u(\mathbf{x} + \mathbf{r}, t) \rangle \quad (2.23)$$

$$\rho(\mathbf{x}, r) \equiv \frac{\langle u(\mathbf{x}, t)u(\mathbf{x} + \mathbf{r}, t) \rangle}{\langle u(\mathbf{x}, t)^2 \rangle} \quad (2.24)$$

$$\Lambda_l \equiv \int_0^{+\infty} \rho_u(r) dr \quad (2.25)$$

As the covariance, the *spatial correlation function* and the *integral length scale* respectively. Here,  $\mathbf{r}$  is the vector indicating the distance between the two points in space where fluctuations are considered. If  $\mathbf{r}$  is parallel to the velocity fluctuation  $i$ -th component  $u_i$ , then the autocorrelation is said to be *longitudinal*. On the other hand, if  $\mathbf{r}$  is perpendicular, it is *perpendicular*. In the case of statistically homogeneous process, the autocorrelation is put more simply as:

$$\rho_u(r) = \frac{\langle u(\mathbf{x}, t)u(\mathbf{x} + \mathbf{r}, t) \rangle}{\langle u^2 \rangle} \quad (2.26)$$

because both the covariance and the spatial correlation function are independent of space.

#### 2.1.5. Taylor's hypothesis

The results presented later in this thesis are obtained in the majority of cases by using a hot-wire anemometer. The underlying assumption when deducing quantities from the data acquired with this tool is the *Taylor's hypothesis*, also known as the *frozen turbulence approximation*. Taylor's suggestion was that the behaviours of a specific fluid-mechanic quantity  $Q$  in space and time along the mean direction of motion, are simply related by a convection velocity  $U_C$ , aligned with the mean velocity along an  $x$  direction:

$$\frac{\partial Q}{\partial t} \approx -U_C \frac{\partial Q}{\partial x} \quad (2.27)$$

it tells us that the diffusion and the transport of the quantity  $Q$  along the perpendicular direction to the mean flow are neglected. Generally, the local mean velocity is used as convection velocity, meaning that the flow structures, of any scale, behave like they are 'frozen' and are only convected by the mean local velocity. It may appear as a coarse approximation of real-life cases, but its validity in most cases is confirmed by experimental studies. On the other hand, to allow for a better approximation the key parameter to act on is the convection velocity. For instance, it is mostly accepted to use the local mean velocity for the advection of the large-scale structures, but a different approach should be taken when investigating the smaller scales inhabiting the near-wall region. In wall-bounded turbulence, as suggested by Romano 1995 Del Álamo and Jiménez 2009, the convection velocity should be far lower than the local mean, and usually highly dependent on the Reynolds number.

#### 2.1.6. Spectral analysis

When analysing random processes, not all the information can be inferred from the PDF. It is for this reason that in the previous section the correlation function is introduced, which proved to provide additional details on the relation established between the signal at different points in time or space. Adding a spectral analysis allows a description of how the energy of the turbulent fluctuations is distributed among the different frequencies, and with the Taylor's hypothesis, among the scales too. This information is inferred from the *power spectral density* (PSD), by using the Fourier transform  $\mathcal{F}_T$ , transforming a mathematical function of time  $f(t)$  into another function of angular frequency  $\mathcal{F}(\omega)$

$$\mathcal{F} = \frac{1}{2\pi} \int_{-\infty}^{+\infty} e^{-i\omega\tau} f(\tau) d\tau \quad (2.28)$$

The PSD represents the distribution of the power of the fluctuations among different frequencies:

$$\mathcal{S}(\omega) = \lim_{T \rightarrow \infty} \langle \mathcal{F}_T(\omega) \rangle \quad (2.29)$$

Where  $\mathcal{F}_T(\omega)$  is the *truncated Fourier transform* of the velocity fluctuation  $f(t)$ , where the integration is performed over a finite interval T:

$$\mathcal{F}_T(\omega) = \frac{1}{\sqrt{T}} \int_0^{+\infty} f(t) e^{-i\omega t} dt \quad (2.30)$$

The choice of using the truncated fourier transform is due to the continuous nature of the signals of interests. For a typical experimental signal the *power* P of a signal u(t) is defined as:

$$P = \lim_{T \rightarrow \infty} \frac{1}{T} \int_0^{+\infty} |u(t)|^2 dt \quad (2.31)$$

with the Fourier transform not existing in numerous cases because of the infinite time domain over which the signal is integrated. The problem is solved by limiting the Fourier transform to a finite domain, as in the *truncated Fourier transform*.

For the Wiener-Khinchin theorem, for a statistically stationary process, the PSD is the Fourier transform of the corresponding autocovariance function  $R(\tau)$ :

$$\mathcal{S}(\omega) = \frac{1}{2\pi} \int_{-\infty}^{+\infty} e^{-i\omega\tau} R(\tau) d\tau \quad (2.32)$$

and it follows that:

$$R(\tau) = \int_{-\infty}^{+\infty} e^{i\omega\tau} \mathcal{S}(\omega) d\omega \quad (2.33)$$

Since both the fluctuations  $u(t)$  and the autocovariance function  $R(\tau)$  are real-valued functions, their Fourier transform (the PSD) is an even function, i.e.  $\mathcal{S}(\omega) = \mathcal{S}(-\omega)$ . Because only positive frequencies will be considered in this work, only the one-sided PSD  $P(\omega)$  is used:

$$P(\omega) = \begin{cases} 2\mathcal{S}(\omega) & \omega \geq 0 \\ 0 & \text{otherwise} \end{cases}$$

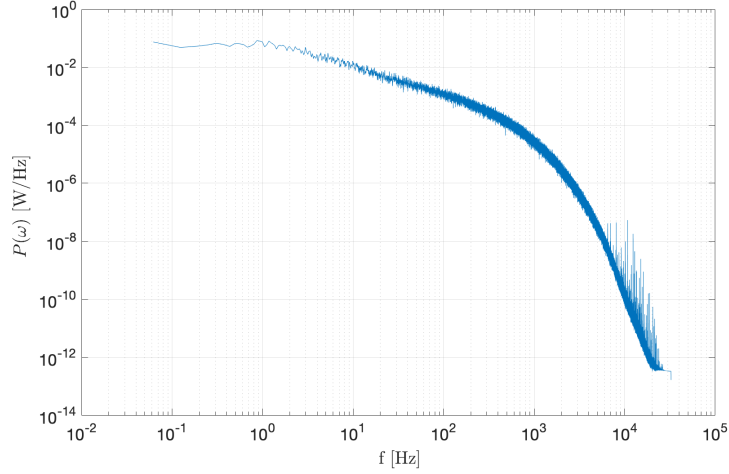


Figure 2.1: Power spectral density as function of frequency for  $Re_\tau = 9.9 \times 10^3$  at  $y^+ = 60$ . Data from current measurements.

In most cases, the angular frequency is substituted with the frequency  $f = \omega/2\pi$ . An example of the power spectral density in double logarithmic scaling is shown in Fig.2.1.

It is interesting to notice that for  $\tau=0$ , eq.(2.1.6) becomes:

$$R(0) = \overline{u^2} = \int_{-\infty}^{+\infty} \mathcal{S}(\omega) d\omega \quad (2.34)$$

$\mathcal{S}(\omega)$  can be seen as the variance, or equivalently the turbulent energy, of the band  $d\omega$  and centered in  $\omega$ .

Experimentally, the random signal  $u(t)$  considered for the estimation of the power spectral density is usually a time series of finite length. Therefore, a reliable method to estimate spectral density from a finite sequence of time samples is required. The most intuitive way to proceed would be to apply periodogram method, where a discrete Fourier transform (DFT) is applied to the whole data set. However, this method has two main disadvantages: the *spectral leakage* and the unacceptable noisy result. The spectral leakage consists in the spectral bias due to the "windowing" of the time series, causing an abrupt truncation of the data. A finite time series can be interpreted as an infinite signal seen through a rectangular window of the size of the sampling time. In practice, the signal is multiplied by a rectangular window function, whose shape causes discontinuities at the beginning and end of samples. This effect can be attenuated by tapering the time-history using a window function

that allows a more gradual truncation of the data set, such as the Hann or Hamming window. On the other hand, because of the shape of the window, a loss factor is introduced due to the artificial dampening of the data, affecting especially those located at the beginning and end of the window.

Then, in order to make the spectral density converge with sampling time, the Welch's method can be applied. It consists of dividing the sampled data  $u(t)$ , consisting in  $n$  points, in  $N$  segments of length  $L$ , with a 50% overlap between each other. To each segment, a window function  $w(t)$  (Hann or Hamming) is applied in the time domain,  $u(t)w(t)$ . The DFT is now separately computed for each  $u(t)w(t)$  of every segment  $N$ , taking the square magnitude to obtain  $N$  spectral estimates. The final result is achieved by averaging the power spectral densities obtained for every segment. The key features of this method are the averaging and the overlapping. The first allows to obtain a smoother PSD, by computing the single DFT for each segment. The second limits the loss of information related to the windowing. The spectral analysis performed on the current measurements is based on the Welch's method. In some cases, instead of the frequency, the wavenumber  $k$  or the wavelength  $\lambda$  will be used:

$$k = \frac{2\pi f}{\bar{U}} \quad (2.35)$$

$$\lambda = \frac{2\pi}{k} \quad (2.36)$$

where  $\bar{U}$  is the local mean velocity. These conversions are based on the Taylor's hypothesis, which will be briefly reviewed in the next section. This hypothesis, known as the *frozen turbulence* is based on the assumption that the turbulent structures are only convected by the mean local velocity. To analyse the hot-wire data later presented, the wavenumber spectrum  $\Phi_{uu}(k)$  was used in the form:

$$\Phi_{uu}(k) = \frac{P(f)\bar{U}}{2\pi} \quad (2.37)$$

Obtained imposing the following

$$\overline{u^2} = \int_0^{+\infty} \Phi_{uu}(k) dk \quad (2.38)$$

Yielding the normalised form of eq.(2.37).

The spectra analysis can be extended to yield information about the scale-to-scale (linear) correlation between scales at two different positions ( $y_1$  and  $y_2$ ). Considering two velocity fluctuations signals, at two wall-normal locations  $u(y_1)$  and  $u(y_2)$ , the linear correlation can be inferred by computing the linear coherence spectrum (LCS), which is defined as:

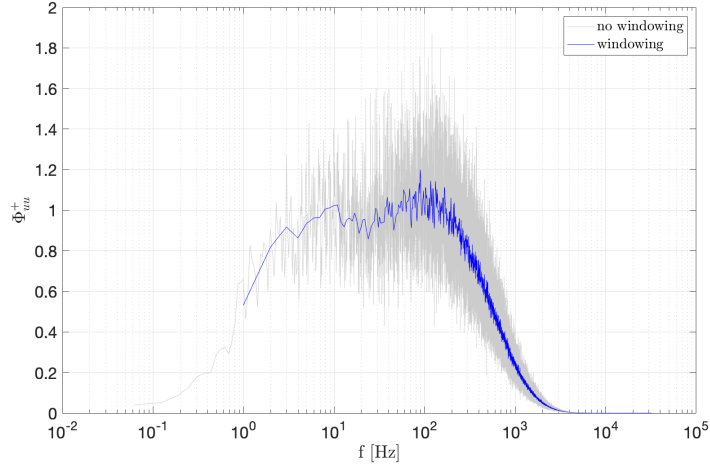


Figure 2.2: Pre-multiplied form of the power spectral density as function of frequency, for  $Re_\tau = 9.9 \times 10^3$  at  $y^+ = 60$ . Data from current measurements.

$$\gamma_L^2 = \frac{\left| \left\langle \tilde{U}(y; \lambda_x) \tilde{U}^*(y_{ref}; \lambda_x) \right\rangle \right|^2}{\left| \left\langle \tilde{U}(y; \lambda_x) \right\rangle \right|^2 \left| \left\langle \tilde{U}(y_{ref}; \lambda_x) \right\rangle \right|^2} = \frac{\left| \Phi'_{uu}(y, y_{ref}; \lambda_x) \right|}{\Phi_{uu}(y; \lambda_x) \Phi_{uu}(y_{ref}; \lambda_x)}. \quad (2.39)$$

(as in Baars, Hutchins, and Marusic 2016) where  $U(y_1; \lambda_x) = \mathcal{F}[u(y)]$  is the Fourier transform of the signal at the  $y$ -location ( $u(y)$ ), the asterisk denotes the complex conjugate, the  $\langle \rangle$  indicates the ensemble averaging, and  $||$  the modulus.  $\Phi'_{uu}(y_1, y_2; \lambda_x)$  is the cross-spectrum and  $\Phi_{uu}(y_1, \lambda_x)$  is the energy spectra of  $u(y_1)$  (similarly for  $y_2$ ), with  $\lambda_x$  being the streamwise wavelength.

From the definition, since it incorporates only the magnitude of the cross-spectrum, the value of  $\gamma_L^2$  represents the maximum correlation for a given scale. In other words, it can be equivalently interpreted as the common variance shared by  $u(y_1)$  and  $u(y_2)$ .

If information about the phase shift between the correlated scales are required, a linear stochastic estimate (LSE) of the turbulence can be used (Adrian 1979). The LSE evaluates a conditional output from an unconditional input, by computing the stochastic transfer kernel  $H_L$ . In spectral space,  $H_L$  is a complex-valued parameter indicating how the output is stochastically coupled with the input, at each scale. Taking  $u(y_1)$  as input, and  $u(y_2)$  as output, the kernel is defined as:

$$H_L(y_1, y_2; \lambda_x) = \frac{\langle U(y_1; \lambda_x)U^*(y_2; \lambda_x) \rangle}{|\langle U(y_1; \lambda_x) \rangle|^2} = |H_L|e^{j\phi} \quad (2.40)$$

Here, the gain squared of the kernel of eq.(2.40) ( $|H_L(y_1, y_2; \lambda_x)|^2$ ) is related to the LCS of eq.(2.39) via:

$$|H_L(y_1, y_2; \lambda_x)|^2 = \frac{\gamma_L^2(y_1, y_2; \lambda_x) \langle |U(y_2; \lambda_x)|^2 \rangle}{\langle |U(y_1; \lambda_x)|^2 \rangle} \quad (2.41)$$

where  $\phi$  is the phase, embedding the stochastic phase shift for the coherent scales.

## 2.2. Pipe flow

Since the pioneering work of Reynolds in 1883, the pipe flow has demonstrated to be crucial for understanding many aspects of wall-bounded turbulence. For instance, its geometry allows an easy computation of the pressure drop, and therefore to accurately estimate key friction quantities for the mean flow. The main purpose of this section is to discuss the fundamental equations to describe the phenomena in a mathematical way. The starting point are the Navier-Stokes equations for an incompressible fluid, in Eulerian and neglecting the body forces:

$$\nabla \cdot \mathbf{U} = 0 \quad (2.42)$$

$$\frac{\partial \mathbf{U}}{\partial t} + (\mathbf{U} \cdot \nabla) \mathbf{U} = -\frac{1}{\rho} \nabla p + \nu \nabla^2 \mathbf{U} \quad (2.43)$$

Being the continuity (mass conservation) equation and the momentum balance respectively.  $\mathbf{U}=(U,V,W)$  is the velocity vector (and  $U, V, W$  are the component in the streamwise, wall-normal and spanwise direction respectively),  $\rho$  is the density and for incompressible flows it is considered constant,  $p$  is the pressure and  $\nu = \mu/\rho$  is the kinematic viscosity. We now implement the Reynolds decomposition introduced in the first section of this chapter, exploiting the fact that we are dealing with a turbulent flow and therefore the velocity  $\mathbf{U}(\mathbf{x}, t)$  is a random variable:

$$\mathbf{U}(\mathbf{x}, t) = \overline{\mathbf{U}}(\mathbf{x}, t) + u(\mathbf{x}, t) \quad (2.44)$$

Where  $\overline{\mathbf{U}}(\mathbf{x}, t)$  is the mean velocity, computed as in 2.1.1 and  $u(\mathbf{x}, t)$  indicates the velocity fluctuations. For all components, after the Reynolds decomposition, the mean velocity vector is  $(\overline{U}, \overline{V}, \overline{W})$  and  $(\overline{u}, \overline{v}, \overline{w})$  is the fluctuating part. The Reynolds decomposition can be extended to the Navier-Stokes equations to obtain the RANS - Reynolds averaged Navier Stokes equations. Given the geometry of the pipe, it is convenient to change the system of coordinates

from Cartesian  $(x,y,z)$  to cylindrical  $(x,r,\theta)$ . In this case,  $x$  indicates the axial streamwise direction,  $r$  is the radial coordinate originating at the centerline and perpendicular to the wall of the pipe and  $\theta$  the angular coordinate. As a turbulent pipe flow is statistically axial-symmetric:

$$\overline{W} = \overline{uw} = \overline{vw} = \frac{\partial}{\partial \theta} = 0 \quad (2.45)$$

the set of equations 2.42 and 2.43 in the axial and radial directions become:

$$\frac{\partial \overline{U}}{\partial x} + \frac{1}{r} \frac{\partial}{\partial r}(r\overline{V}) = 0 \quad (2.46)$$

$$\frac{\partial \overline{U}}{\partial t} + \overline{U} \frac{\partial \overline{U}}{\partial x} + \overline{V} \frac{\partial \overline{U}}{\partial r} = -\frac{1}{\rho} \frac{\partial \overline{p}}{\partial x} - \frac{\partial}{\partial x} \overline{u^2} - \frac{1}{r} \frac{\partial}{\partial r}(r\overline{uw}) + \nu \nabla^2 \overline{U} \quad (2.47)$$

$$\frac{\partial \overline{V}}{\partial t} + \overline{U} \frac{\partial \overline{V}}{\partial x} + \overline{V} \frac{\partial \overline{V}}{\partial r} = -\frac{1}{\rho} \frac{\partial \overline{p}}{\partial r} - \frac{\partial}{\partial x} \overline{uv} - \frac{1}{r} \frac{\partial}{\partial r}(r\overline{v^2}) + \frac{\overline{w^2}}{r} + \nu(\nabla^2 \overline{V} - \frac{\overline{V}}{r^2}) \quad (2.48)$$

We now focus on statistically stationary flows, for which it holds:

$$\frac{\partial}{\partial t} = 0 \quad (2.49)$$

and if we concentrate on the fully developed region, where the flow is statistically independent on the axial position:

$$\frac{\partial \overline{U}}{\partial x} = \frac{\partial \overline{u^2}}{\partial x} = \frac{\partial \overline{v^2}}{\partial x} = 0 \quad (2.50)$$

As for the boundary conditions, the no-slip and axial-symmetry leads to  $\overline{V}|_{r=R} = \overline{V}|_{r=0}$ . Plugging it in eq.(2.46), the following condition is retrieved:

$$\overline{V} = 0 \quad (2.51)$$

namely that the mean radial velocity should be zero everywhere. By applying the boundary conditions to the r-component of the momentum balance equation, 2.48 becomes:

$$\frac{1}{\rho} \frac{\partial \overline{p}}{\partial r} + \frac{\partial \overline{v^2}}{\partial r} = \frac{\overline{w^2}}{r} - \frac{\overline{v^2}}{r} \quad (2.52)$$

Integrating the equation above between a radial coordinate  $r$  and the pipe radius  $R$ , taking the  $x$  derivative and remembering the hypothesis of fully developed flow 2.50:

$$\frac{\partial \overline{p}}{\partial x} = \frac{\partial \overline{p_w}}{\partial x} \quad (2.53)$$

since  $\overline{p_w}$  is the mean pressure at the wall, the relation above states that the pressure gradient along the axial direction is uniform along the pipe radius. Now we consider the x-component of the momentum balance of eq.(2.48), and applying the results obtained in eq.(2.53), the boundary condition on the mean wall-normal velocity in eq.(2.51), and the conditions on the flows in eq.(2.49) and eq.(2.50), it becomes:

$$\frac{1}{\rho} \frac{\partial \overline{p_w}}{\partial x} = -\frac{1}{r} \frac{d}{dr}(r\overline{uv}) + \frac{\nu}{r} \frac{d}{dr}\left(r \frac{d\overline{U}}{dr}\right) \quad (2.54)$$

Expliciting the total shear stress  $\tau = \mu \frac{d\overline{U}}{dr} - \rho\overline{uv}$ , the equation above can be rewritten in a more compact way as:

$$\frac{\partial \overline{p_w}}{\partial x} = -\frac{1}{r} \frac{d(r\tau)}{dr} \quad (2.55)$$

leading to the convenient link between the wall-shear stress and pressure drop along the pipe if integrated from 0 to R in the radial direction:

$$\tau_w = \frac{R}{2} \frac{d\overline{p_w}}{dx} \quad (2.56)$$

Eq.(2.56) is extremely important from the experimental point of view, since it states that to compute the wall-shear stress it is sufficient to accurately acquire the pressure drop along the pipe. This is crucial for an accurate investigation of the pipe flow phenomena.

### 2.3. Wall-bounded flows

Classical turbulence theory classifies the flows into *free shear*, such as wakes and jets, and *wall-bounded*, which includes all the flows over one or more surfaces. Examples of the latter are *internal flows*, such as the flow inside a pipe or a duct, and *external flows* such as the flow over a plate. The presence of the solid surface, in the case of wall-bounded flows, influences the onset mechanism of turbulence. If in jets or wakes turbulence originates from the differences in the velocity field of the flow, this is not the case for the wall-bounded. Here, due to the presence of the wall, the boundary condition to apply is the no-slip i.e. the velocity of the fluid at the wall is zero. Together with the viscosity of the fluid, the onset of turbulence is triggered. In this section, the main characteristics of wall-bounded turbulence are described.

#### 2.3.1. Turbulence scaling and mean velocity profile

According to classical turbulence theory, the domain of wall-bounded turbulent flows can be divided into two main areas: the *inner region*, close to the wall where the viscous forces are dominant, and the *outer region*, located further away from the solid surface and where the effect of viscous forces is smaller

than the inertial ones. In other words, this division is made on the basis that in the inner region the flow is influenced by viscosity and not by the external geometry. This should lead to a similar behaviour of the flows in the near-wall region, despite different geometries, since the external conditions should not affect their dynamics. Close to the wall, the parameters affecting the mean velocity  $\bar{U}$  are the wall-shear stress  $\tau$ , the wall-distance  $y$  and the kinematic viscosity  $\nu = \mu/\rho$ . Thus,  $\bar{U}$  is expected to scale on properly defined normalised parameters (the viscous scales) based on these quantities. First, the friction velocity  $u_\tau$  is defined

$$u_\tau = \sqrt{\frac{\tau_w}{\rho}} \quad (2.57)$$

with  $\rho$  being the fluid density. Now, the viscous length scale  $l_*$  can be introduced

$$l_* = \frac{\nu}{u_\tau} \quad (2.58)$$

Once these two quantities are defined, the viscous time scale  $t_*$  can be expressed as

$$t_* = \frac{l_*}{u_\tau} = \frac{\nu}{u_\tau^2} \quad (2.59)$$

and the key quantity used in throughout the entire thesis, the friction Reynolds number,  $Re_\tau$  is defined for the wall-bounded flows:

$$Re_\tau = \frac{Lu_\tau}{\nu} = \frac{R}{l_*} = R^+ \quad (2.60)$$

where  $L$  is the characteristic length scales, the pipe radius  $R$  in the current case of a pipe flow. It is interesting to notice how the friction Reynolds number represents the viscous-scaled pipe radius, or equivalently, the ratio between the outer and the inner scales. As introduced here, the superscript  $+$  will denote from here on, the inner-scaled variables. The inner-scaled velocity,  $U^+$  is defined as:

$$U^+ = \frac{\bar{U}}{u_\tau} = f\left(\frac{yu_\tau}{\nu}\right) = f\left(\frac{y}{l_*}\right) \quad (2.61)$$

where  $y/l_*$  is the inner-scaled wall-normal distance,  $y^+$ . Its definition resembles a local friction Reynolds number. In a fundamental work, Prandtl introduces the *Prandtl's law of the wall*, where he postulates that in the inner-region, the following relation holds:

$$U^+ = f(y^+) \quad (2.62)$$

For regions extremely close to the wall,  $y^+ < 5$ , known as the *viscous sublayer*, eq.(2.62) becomes:

$$U^+ = y^+ \quad (2.63)$$

The part of the inner-region outside of the viscous sublayer is called *buffer region*, where there is the maximum turbulence production and maximum streamwise turbulence intensity (see Pope 2001). Further away from the wall, the viscous stresses become negligible compared to the turbulent stresses. Here, in the outer region (or core region for internal flows), the scaling parameters change. The relevant length scale is now defined by the external geometry: the pipe radius for the pipe flow, the half-height of the channel for the channel flow, and the boundary layer thickness for the turbulent flow over a flat plate:

$$Y = \frac{y}{R} \quad (2.64)$$

As for the velocity,  $u_\tau$  is still used as scaling quantity. The dimensional analysis of the outer region, leads to the *Coles velocity defect law*

$$\frac{U_{CL} - \bar{U}}{u_\tau} = g\left(\frac{y}{R}\right) \quad (2.65)$$

with  $U_{CL}$  being the centerline velocity. If the Reynolds number is large enough, we can assume the existence of a region of wall distances, called the *overlap region* that have large  $y^+$  values ( $y^+ \gg 1$ ) and small  $Y$  values ( $Y \ll 1$ ), or equivalently  $l_* \ll y \ll R$ . This means that both eq.(2.62) and (2.65) hold at the same time:

$$f\left(\frac{u_\tau y}{\nu}\right) = g\left(\frac{y}{R}\right) \quad (2.66)$$

From the derivation of Millikan (Millikan 1938), in the overlap region, the relative derivatives of the velocity profiles should be independent of the length scale, therefore constant:

$$\frac{\partial}{\partial y} \left( \frac{\bar{U}}{u_\tau} \right) = \frac{u_\tau}{\nu} f' \left( \frac{y u_\tau}{\nu} \right) = -\frac{1}{R} g' \left( \frac{y}{R} \right) \quad (2.67)$$

The solution of eq.(2.67) is for  $f'$  and  $g'$  being inversely proportional to  $y^+$  and  $Y$  respectively. Integrating eq.(2.67) leads to a logarithmic mean velocity profile in the overlap region:

$$U^+ = \frac{1}{\kappa} \ln(y^+) + B \quad (2.68)$$

$$\frac{U_{CL} - \bar{U}}{u_\tau} = -\frac{1}{\kappa} \ln\left(\frac{y}{R}\right) + C \quad (2.69)$$

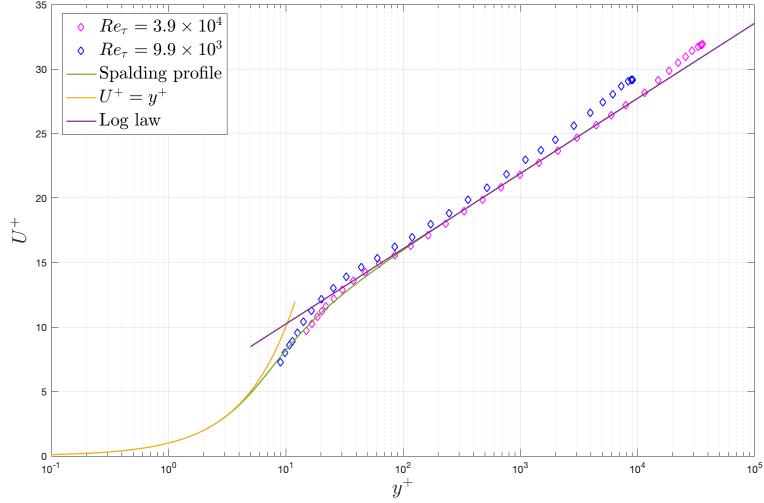


Figure 2.3: Inner-scaled mean velocity profile as function of inner-scaled distance from the wall for  $Re_\tau = 9.9 \times 10^3$  and  $Re_\tau = 3.9 \times 10^4$ . Data from current measurements.

Where eq.(2.68) is known as *logarithmic law of the wall* or *log law*, first derived by Prandtl (Prandtl 1925). The start of the logarithmic region is still object of debate, but its lower bound it is accepted to be in the range  $50 < y^+ < 200$ , extending to around  $0.15R$ . The constants  $\kappa$  and  $B$  are denoted as the Von Kármán and additive constants. Classical turbulence theory states their universal nature, independent from the type of wall-bounded flows that it describes. Fig.2.3 compares the mean-velocity profile for  $Re_\tau = 9.9 \times 10^3$  and  $Re_\tau = 3.9 \times 10^4$ . As the Reynolds number increases, the log region is seen to extend further from the wall in inner units. Another interesting result is obtained by adding the inner and outer formulations of the logarithmic law, namely eq.(2.68) and eq.(2.69):

$$\frac{U_{CL}}{u_\tau} = \frac{1}{\kappa} \ln(Re_\tau) + D \quad (2.70)$$

usually referred to as the *friction law*, from which the friction factor  $C_f$  is specified as:

$$C_f = 2 \left( \frac{u_\tau}{U_{CL}} \right)^2 \quad (2.71)$$

## 2.4. The scales of turbulence

Turbulence is characterised by a wide spectrum of eddies of different sizes. The largest scales are limited by the external geometry of the flow: for a boundary layer it is the boundary layer thickness  $\delta$ , for a channel flow the half-height of the channel  $h/2$  and for the current case of the pipe flow, the radius  $R$ . In order for the turbulence to be sustained, energy should be injected to the large scales from the mean-flow via a production mechanism, or from an external source of energy like heating. The interaction between the eddies enhances the energy transfer, in an inviscid way, to gradually smaller scales until the viscous stresses become increasingly important, and the kinetic energy is dissipated into heat. This process is known as *energy cascade* and was first mentioned by the British scientist Richardson (1922). According to Richardson, eddies can therefore be characterised by three parameters: length  $l$ , velocity  $u(l)$  and timescale  $t(l) = l/u(l)$ . The large scale are characterised by a length  $l_0$  comparable to the macroscopic geometric feature, generally denoted as  $L$ . The velocity  $u_0$  is of the order of  $U$ , therefore the corresponding Reynolds number  $Re_0 = l_0 u_0 / \nu$  is large since the viscous stresses are negligible. It is only later, in 1941, that Kolmogorov suggested a novel approach based on the dependence of velocity and time on the length: he noticed that as the length decreases, the velocity and time behave in the same way. Three are the main hypothesis of his theory. The first is known as the *local isotropy* hypothesis, stating that the small-scale turbulence is statistically isotropic for Reynolds numbers sufficiently large. This characteristic physically means that the statistics of the small scales do not depend on the direction of the mean flow. In other words the small scales "forget" the information from the mean flow and the boundary conditions, contrary to what happens for the large scales. Secondly, for sufficiently high Reynolds, small-scale turbulence statistics are universally described by the mean dissipation rate of energy  $\epsilon \approx u^3/l$  and the viscosity  $\nu$ . This is due to the viscous process underpinning the dissipation process at small scales, of the energy transferred from the big scales. From the two parameters characterising the statistics, the Kolmogorov scale can be defined as:

$$\eta \equiv \left( \frac{\nu^3}{\epsilon} \right)^{1/4} \quad (2.72)$$

and in the same way, the velocity and time scales of the dissipation range:

$$u_\eta \equiv (\epsilon \nu)^{1/4} \quad (2.73)$$

$$t_\eta \equiv \left( \frac{\nu}{\epsilon} \right)^{1/2} \quad (2.74)$$

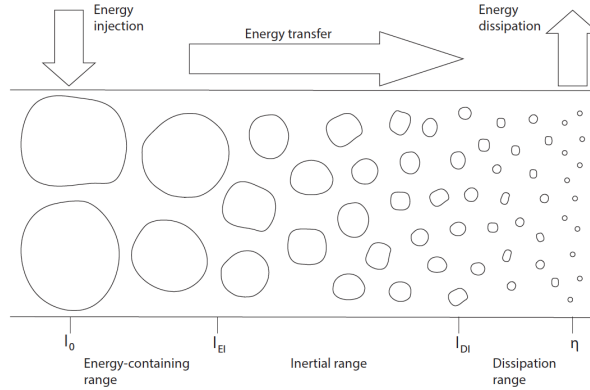


Figure 2.4: Schematic of the energy cascade process from Fiorini 2017.

Consequently, the Kolomogorov length scale gives the ratio between the largest and smallest scales of turbulence i.e. the range of the size of eddies:

$$\frac{l_0}{\eta} = \frac{l_0 \epsilon^{1/4}}{\nu^{3/4}} \sim \frac{l_0}{\nu^{3/4}} \left( \frac{u^3}{l_0} \right)^{1/4} = \left( \frac{l_0 u}{\nu} \right)^{3/4} = Re^{3/4} \quad (2.75)$$

with  $u$  being the velocity of the large scales. Intuitively this states that as the Reynolds number increases, the range of scales between  $l_0$  and  $\eta$  does as well, explaining the difficulties encountered in the detailed description of the turbulent flows without invoking any modelling assumption. Moreover, it follows that for very high Reynolds numbers there is an increasing range of scales between  $l_0$  and  $\eta$ : the physical difference between the large scales and smallest scales increases almost linearly. This phenomena is known as the *scale separation*. Intuitively, if the size of the external geometry is obviously fixed, the scale separation occurs because of the progressive decrease in size of the smaller scales,  $\eta$ . The third hypothesis of the Kolmogorov theory states that for sufficiently high Reynolds numbers, in the inertial sub-range  $\eta \ll l \ll l_0$ , eddies are universally determined only by the mean dissipation rate  $\epsilon$ . Fig.2.4 below captures both the energy cascade process and the scale separation.

## 2.5. Hot-wire anemometry

Despite the undeniable progress in experimental measuring techniques, such as holographic methods or three-dimensional particle tracking, the hot-wire anemometry (HWA) remains one of the most used techniques for velocity measurements in turbulent flows. Its popularity, kept unchanged so long after its first introduction by King in 1914, is mainly due to its exceptional spatial and

temporal resolution for a relatively cheap price compared to optical measurements, for instance. In other words, hot-wire anemometry is able to capture the smallest and fastest physically relevant velocity fluctuations. Of course, placing such element in the flow will disturb the local flow field, but it has been proven that intrusivity is limited for a well-designed probe, meaning that possible disturbances are accounted for in the calibration process. As the name suggests, the hot-wire anemometry implies the presence of a hot-wire, i.e. heated wire to make velocity measurements. The fundamental working principle of HWA is based on the fact that the local fluid velocity is indirectly measured by sensing the changes in the forced heat convection by the small, electrically-heated wire that is exposed to the flow. In the specific case of this thesis, the hot-wire is operated in the constant temperature mode (CTA). The anemometer keeps the temperature of the wire constant through a compensating electronic circuit with a feedback loop, sensing the changes in heat transfer due to the velocity fluctuations. By measuring the electrical current required to keep the temperature constant and an accurate calibration, it is possible to retrieve the velocity of the flow.

### 2.5.1. Basic principles

The principle at the basis of hot-wire anemometry is the amount of cooling that is experienced by the heated wire when exposed to the turbulent flow. In this case, a relation between the cooling of the wire, the heat introduced to keep the wire at the constant temperature and the local flow velocity can be observed. Assuming that the wire is heated through the Joule's effect, the heating power is given by:

$$P = IV = I^2 R_w = \frac{V^2}{R_w} \quad (2.76)$$

where  $I$  is the electrical current heating the wire,  $V$  is the voltage drop across the sensor and  $R_w$  is the resistance of the wire. Multiple phenomena can be cause of the cooling of the wire: radiation losses (accounting for only 0.1% of the convective losses), free/natural convection (negligible compared to the forced convections in situations like the hot-wire anemometry), heat conduction of the prongs of the probe (not negligible, but accounted for during the calibration procedure) and forced convection. It is clear how the latter is generally assumed to be the primary source of heat loss for the wire. Forced convection,  $W$  is expressed as:

$$W = hA_w(T_w - T) = h\pi DL(T_w - T) \quad (2.77)$$

where  $h$  is the convective heat transfer coefficient,  $A_w$  the area of the wire with a diameter of  $D$  and a length of  $L$ , where the forced convection takes place.  $T_w$  and  $T$  are respectively the temperature of the wire and the one of fluid in

contact with it. In order to express the heat transfer in a non-dimensional way, for a cylindrical-shaped body, the *Nusselt number*,  $Nu$  is introduced to replace  $h$ :

$$Nu = \frac{hD}{k_f} \quad (2.78)$$

where  $k_f$  is the thermal conductivity of the fluid. Assuming incompressible flows, ignoring free convection and using wires with a large length-to-diameter ratio, the Nusselt number is now a function of only the wire's Reynolds number  $Re_w$  (using the diameter of the wire  $D$ ) and the temperature overheat ratio  $a_T$ ,  $Nu = f(Re_w, a_T)$ . The overheat ratio is a crucial parameter when operating the hot-wire and can be defined in terms of temperature and resistance as:

$$a_T = \frac{T_w - T_0}{T_0}, a_R = \frac{R_w - R_0}{R_0} \quad (2.79)$$

where the subscript  $w$  denotes quantities referring to the wire, and the 0 to the cold/reference state. If  $T_w - T_0 < 250^\circ$ , the working resistance of the wire  $R_w$  varies linearly with its temperature:

$$R_w = R_0[1 + \alpha(T_w - T_0)] \quad (2.80)$$

where  $\alpha$  is the temperature coefficient of electrical resistivity of the material constituting the wire, typically  $3.6 \times 10^{-3}/C$  for Platinum wires. In general, it is a positive quantity for metals, meaning that the resistance increases with the temperature. Despite the assumptions made, there is still a variety of relations possible between the Nusselt number and the wire Reynolds number, such as the empirical correlation:

$$Nu = [A_1(a_T) + B_1(a_T)Re_w^n](1 + a_T/2)^m; \quad (2.81)$$

where  $m$ ,  $A_1$  and  $B_1$  are temperature-dependent constants. If we now express  $Re_w$  in terms of cooling velocity, the latter becomes non-linearly dependent on forced convection  $W$ , which in turn can be coupled to electrical heating via eq.(2.76) to 2.78, yielding:

$$I^2 R_w = V^2 / R_w = \{\pi L k_f (T_w - T_\infty)\} Nu \quad (2.82)$$

where, for a specific case when the wire is operated at constant overheat ratio, the terms in brackets can be considered constant. Making the cooling velocity  $U$  now explicit, substituting the expression of the Nusselt number of eq.(2.81) and incorporating the case-specific parameters such as  $\alpha_0$  in the calibration constants  $A_2$  and  $B_2$ , it yields to:

$$V^2 = (A_2 + B_2 U^n)(T_w - T) \quad (2.83)$$

If the hot-wire is operated in CTA mode, like throughout the work here presented, for an ambient temperature of  $T$ , the quantities  $R_w$  and the difference  $(T_w - T)$  are constant and can be included in the calibration constants  $A$  and  $B$ , yielding to the so-called *King's law*:

$$V^2 = A + BU^n \quad (2.84)$$

clearly showing the thermoelectrical principle at the basis of hot-wire anemometry, where the cooling velocity  $U$  is non-linearly related to the voltage  $V$  passing through the heated wire. Given the small sensor size (with a diameter ranging from  $0.5 - 10\mu\text{m}$  and the length  $0.1 - 2\text{mm}$ ), and the intrinsic variations of each home-made wire, the calibration procedure needs to be performed for each hot-wire probe used, to determine the case-specific calibration parameters. By fitting the calibration points  $(U, V)$  with eq.(2.84), the calibration coefficients  $A$ ,  $B$  and  $n$  can be inferred. A simpler alternative to the King's law is to perform a 4<sup>th</sup> order polynomial fit to the data, in the form:

$$U = \sum_{n=0}^4 A_n V^n \quad (2.85)$$

where the coefficients  $A_n$  are determined via least-square fitting. The 4<sup>th</sup> order polynomial is the calibration relation chosen for every measurement presented in this work.

### 2.5.2. Limitations

One of the advantages of using hot-wire anemometry in turbulence measurements is the undeniable good spatial and temporal resolution. But, as the Reynolds numbers increases, the small-scale structures in the near-wall region (of the size of the Kolmogorov scales,  $\eta$ , of a few viscous units here) can become smaller than the sensing length of the wire  $L$ . In this case the wire is unable to capture the smaller velocity fluctuations, responding with an averaged measured value that can be expressed as:

$$u_m(t) = \frac{1}{L} \int_0^L u(s, t) ds \quad (2.86)$$

with  $s$  the coordinate along the wire direction, originating at one of the two prongs. Fig.2.5 demonstrate the effect of insufficient spatial resolution, which is noticeable in terms of attenuation of the inner-scaled variance of the measured streamwise velocity fluctuations. The issue was thoroughly investigated by Wyngaard 1968 for isotropic turbulence, where analytical considerations can be made. On the other hand, experimental rules of thumb have been given for wall-bounded turbulence, starting from the early works of P. M. Ligrani and Bradshaw 1987, who identified the wire viscous length  $L^+ = L/l_*$  as

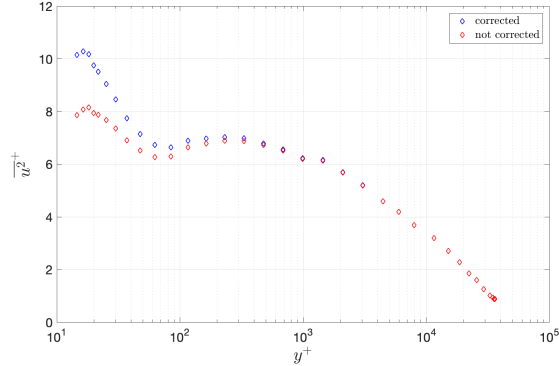


Figure 2.5: Inner-scaled streamwise velocity variance as function of inner-scaled wall-distance for  $Re_\tau = 3.9 \times 10^4$ , using a single hot-wire probe with a sensing length of 0.5mm and a diameter of  $2.5\mu m$ .  $l_* \approx 44$ , leading to attenuation of the energy measured as the red symbols show. Blue symbols are the signal corrected with the scheme proposed by Smits et al. 2011.

key parameter for spatial filtering, and further investigated by Hutchins et al. 2009. In particular, in order not to be greatly affected by insufficient spatial resolution, it is good rule to ensure  $L^+ \leq 20$ . In cases where this is not possible, a number of correction schemes have been put forward, such as Smits et al. 2011 (widely used because it has been validated for a wide range of  $l^+$  and  $Re$ ), P. Monkewitz, Duncan, and Nagib 2010 when small  $L/D$  wires are used, or Miller, Estejab, and Bailey 2014 who incorporates also a correction for the end conduction effect, and also options valid for any turbulent flows by R. Segalini A. Ö. et al. 2011 and A. Segalini et al. 2011. In fact, not all the heat is transferred by forced convection, but as briefly mentioned above, part of the heat is transferred via conduction from the wire to its supporting prongs. This is side-effect of the architecture of the probe and should be limited, by intuitively increasing the length of the wire. This is contrast with the solution for spatial resolution issue, and therefore a compromise can be found by considering that heat conduction is proportional to the cross-section of the wire,  $W_c \propto \pi D^2/4$  and heat convection is proportional to the exposed surface of the wire instead,  $W_{fc} \propto \pi D^2/4L$ . Their ratio, proportional to  $\propto L/D$ , identify the length-to-diameter ratio as key parameter in minimising the end conduction effect without compromising the spatial resolution, with P. M. Ligrani and Bradshaw 1987 suggested a threshold of  $L/D > 200$ .

## 2.6. Background

In this section a brief overview of the past key studies laying the ground for the present work is presented. The most relevant research topics and open questions are discussed to put the present work into context.

### 2.6.1. *The log-law*

Despite the undeniable progress in theoretical knowledge, experimental and numerical techniques, a correct depiction of wall-bounded flows in the overlap region is still object of intense debate.

During the 1920's, in early days of wall-bounded turbulence research Prandtl and von Kármán extracted the  $1/7$  power-law from Blasius' data, which could describe fairly well both the velocity profile and friction in pipe flows, across the range of Reynolds numbers available at that time.

Not even a decade went by when the experimental investigation on pipe flows by Nikuradse, at higher Reynolds numbers, suggested that the data were better fitted by a slightly modified power-law. The  $1/7$ -power law was made Reynolds-dependent with the power-law exponent  $1/n$ , where  $n$  increases with the Reynolds number. The power-law has always been fairly accepted from its introduction, but few aspects (being the result of an extrapolation, not being valid in the near-wall region, lacking of a physical meaning close to the center and an annoying Reynolds number dependence of the exponent) sparked the interest in finding a better alternative.

The logarithmic-law for the mean velocity profile and friction was presented by von Kármán in 1930. By analysing Nikuradse data and starting from Prandtl's mixing length concept, he was able to prove that the inner-scaled velocity defect in the outer region (normalised with the friction velocity) does not depend on Reynolds number. This led to a logarithmic description of the mean-velocity profile and friction factor, valid for the entire range of Reynolds numbers available.

The value of von Kármán constant  $\kappa$ , one of the two parameters governing the logarithmic law (the other is an additive constant,  $B$ ), was set by von Kármán to 0.36 for the mean-velocity profile and 0.38 for the friction relation.

As matter of facts, canonical flows i.e turbulent boundary layer, channel and pipe flows, are widely believed to be similar in the inner region, and therefore there is no apparent reason why  $\kappa$  should be affected by the geometry.

Even if the form of the log-law remains unchanged today, the value of the von Kármán constant is continuously reevaluated, ranging from 0.36-0.43. Over the years, it reached the "most-popular" value of 0.384 for the zero-pressure gradient TBL (Örlü et al. 2017, Furuichi et al. 2015).

When the first results from the Superpipe in Princeton were available to the turbulence community, they obtained  $\kappa = 0.436$  (Zagarola and Smits 1998).

Not only it was much larger than the expected, but it also resulted from a log-law much further away from the wall than previously assumed. Even when McKeon, Zagarola, and Smits 2005 reanalysed and corrected the data,  $\kappa$  lowered to 0.42, remaining still significantly distant from other suggested values for different geometries and Reynolds numbers regimes.

For long, the scatter was explained by the experimental uncertainty, since high accuracy is required to shed a final light on the matter, until Nagib and Chauhan 2008 challenged the idea of "constants" suggesting a von Kármán coefficient that depends on the flow geometry.

Adding controversies to an already hot-topic, there is the skin-friction relation  $U_{CL} = (1/\kappa)\ln(Re_\tau) + C$ . For the asymptotic matching of the wake already discussed by Coles 1956a, the value of  $\kappa$  in the above relation, named  $\kappa_{CL}$  from here onwards, should be equal to the one extracted from the log-law in the overlap region, but  $\kappa_{CL}$  has consistently remained larger than 0.42 for the pipe flows (0.42-0.43 for the Superpipe data McKeon, Zagarola, and Smits 2005, Cantwell 2019, 0.43 for the CICLoPE facility Fiorini 2017).

Only very recently two solutions have been proposed to solve this conundrum, by P. A. Monkewitz 2017 and by Luchini 2017. On one hand, Luchini confirmed the universality of the logarithmic law of the turbulent velocity profile across different flow geometries, provided the effect of the pressure gradient is considered with an additional higher order term in the formulation. On the other, Monkewitz reanalysed the Superpipe data, introducing a "universal" internal log-law valid for  $10^2 < y^+ < 10^3$  with  $\kappa = 0.384$ , followed by an external log-law valid for  $y^+ < 0.05Re_\tau$  and the wake with  $\kappa_{CL}$  dependent on the flow type (but kept at 0.384 for the TBL and found to be 0.42 by P. A. Monkewitz 2017 for the pipe flow). This arises the question of the statistical significance of the difference between  $\kappa$  and  $\kappa_{CL}$ .

As previously mentioned, it is crucial to rely on accurate description of the mean velocity profile, in particular  $\kappa$  matters for different reasons. First, the log-law (whose slope is  $1/\kappa$ ) is used to verify the quality of the measured profiles and it is also employed in the Clauser method (Clauser 1954) to extract the value of the friction velocity  $u_\tau$ , which is a key quantity in wall-bounded turbulence. As pointed out by Örlü, Fransson, and Alfredsson 2010, it is also used to determine the wall-position during experiments.

Moreover,  $\kappa$  is an input quantity in CFD models for the law of the wall to predict friction, and the impact that it has for a vast range of applications it is now clear.

Reaching conclusions on the nature of the log-law has proven to be extremely challenging, due to multiple reasons. Without a standardisation of methods to extract the value of the parameters and a common view on the boundaries of the logarithmic region it is hard to agree on a value.

Moreover, Örlü 2009 demonstrated the extreme sensitivity of the log-law governing parameters on the limits of the log-region, reporting values of  $\kappa$  ranging from 0.40 down to 0.34. Additionally, the differences in the departure from the law itself are very subtle and very high is the sensitivity of the values of  $\kappa$  and  $\kappa_{CL}$  on the errors on  $u_\tau$ .

On that note, reliable and simple methods to estimate the friction velocity are crucial to limit the uncertainties on the von Kármán parameters, leading to a preference for a geometry like the pipe to conduct these kind of experiments. For this geometry the friction velocity can be readily estimated from the static-pressure drop along the pipe, instead of more complex techniques like the oil-interferometry used for TBL, for instance. The joint efforts of many Universities around the world to build the large-scale experiment CICLoPE is a right step in the direction of highly accurate measurements at high Reynolds numbers regimes.

### 2.6.2. Organised motions in turbulence

Despite being intrinsically chaotic, wall-bounded turbulent flows exhibit an internal architecture of motions. Investigating their organisation and how they interact with each other is key for a better understanding of turbulence nature, flow dynamics and improving control methods.

Although a clear-cut definition of organised motion is still not-existent today, they can in general terms be described as a region both in time and space that is characterised by mass and momentum transport. The traditional classification (Smits, McKeon, and Marusic 2011) identifies four main structures: the near-wall streaks, the hairpin vortices, the large-scale motions and the very-large-scale motions.

The basic units of the turbulent organised motions are the near-wall streaks, first observed by Kline et al. 1967 who investigated down to the viscous sublayer (for  $y^+ < 70$ ). The near-wall streaks, developing in the streamwise direction, are characterised by a spanwise spacing of  $\approx 100\nu/u_\tau$ , by high or low momentum, and are seen to be both Reynolds and flow geometry independent. Alternatively, the fundamental block of coherent structures are suggested to be the hairpin/horseshoe vortices (Adrian 2007). The same vision is shared by Perry, Henbest, and Chong 1986 stating that the turbulent flows can be seen as a *forest of hairpin vortices* (Perry, Henbest, and Chong 1986). Nonetheless, they were first theorised by Theodorsen 1952 as structures with a minimum height of  $\approx 100\nu/u_\tau$ , originating at the wall and extending for a wide range of scales.

Despite controversies on the more or less crucial role in the physics of coherent structures (Cantwell 1981, Schoppa and Hussain 2002), their importance

and diffused presence in the boundary layers was strongly proven first by experimental observation by Head and Bandyopadhyay 1981 and later corroborated by the numerical work of Wu and Moin 2009.

Only recently with the leap in computer powers and technological advancement that allowed more accurate measurements at higher Reynolds numbers, numerical and experimental studies revealed the organisation of the aforementioned elements in larger coherent structures, called large-scale motions (LSM).

Numerous are still the open questions regarding their origin and dynamics, but the widest consensus (Kim and Adrian 1999, Guala, Hommema, and Adrian 2006, Tomkins and Adrian 2003, Ganapathisubramani et al. 2005) believes them to be the result of packets of hairpin vortices travelling at the same convection velocity.

The LSMs extend to approximately 2-3  $\delta$  in the streamwise direction and the hairpins bulding them have their heads inclined at around  $20^\circ$  to the wall (Adrian, Meinhart, and Tomkins 2000) a feature that Adrian 2007 proved to be crucial for the dyanmics. They are also pointed as the responsible for turbulent buldges in the near-wall region, since the aligned hairpins induce low streamwise momentum between the legs (Adrian, Meinhart, and Tomkins 2000, Ganapathisubramani, Longmire, and Marusic 2003).

In 1999, Kim and Adrian 1999 identified long-meandering structures, characterised by low streamwise-momentum regions flanked by higher-velocity flow: the very-large-scale motions (VLSM), or superstructures in boundary layers. Their origin is still not clear, but they are thought to be alignment of packets of LSM (Fig.2.6), centered in the logarithmic region and extending well into the outer region in internal flows, while they appear to break down or to weaken in the case of turbulent boundary layers (Bailey et al. 2010). Their meandering nature makes it difficult to infer their true length by single-point statistics (spectra or correlations).

Experimental studies in boundary layers using a hot-wire rake extending in the spanwise direction, were able to capture structures extending up to 10-20  $\delta$  (Hutchins and Marusic 2007a), whilst a similar technique applied to pipe and channel flows by Monty et al. 2007 led to measure structures developing in the streamwise direction for 20-30 radii or channel half heights. Spectral analysis highlight the energetically and dynamically importance of the LSM and VLSM. Using a feature-detection algorithm and PIV data, Ganapathisubramani, Longmire, and Marusic 2003 and Ganapathisubramani et al. 2005 quantified their significant contributions to the Reynolds shear stress as 50%, with similar percentage presented by Balakumar and Adrian 2007, who also added that modes with  $\lambda_x/\delta > 3$  contributes up to 65% to the total turbulent kinetic energy.

The large wall-normal extension of the (LSM and VLSM) hints at the possible correlation with the near-wall region. Mathis, Hutchins, and Marusic 2009 and Hutchins and Marusic 2007b showed how the larger scales interact

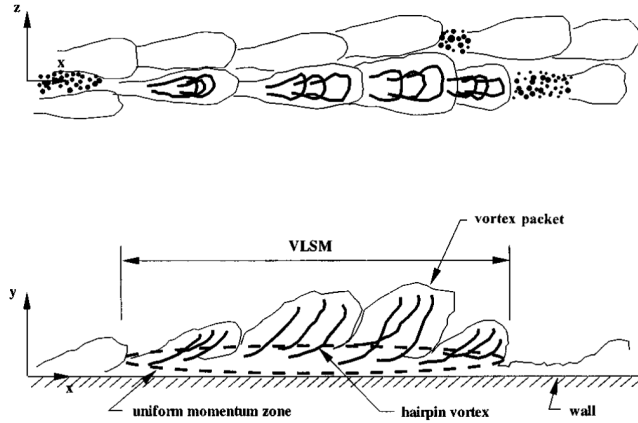


Figure 2.6: Schematic of the alignment of the hairpin packets forming the large- and very-large-scale motions. Reprinted from Kim and Adrian 1999

with the near-wall region through a combined effect of energy superimposition and modulation of the velocity fluctuations of the small-scales. Unravelling the nature of this interaction would help shedding light on some of the controversies in wall-bounded turbulence scaling. For instance, the interaction between small and large scale motions, observed in data from CICLoPE (Örlü et al. 2017) and Klewicki and Falco 1990 Hutchins et al. 2009, challenges the classical inner-scaling of streamwise turbulence intensity that does not take this dynamics into account but is confirmed by experiments performed at the SuperPipe.

### 2.6.3. Attached eddy model

Turbulence modelling remains one of the biggest challenges of the field. However, models are extremely important because they allow for prediction and improve physical insight of many phenomena.

The need for very accurate data both in time and space together with a physical knowledge of the phenomena that still fails to capture the entire richness of turbulence, are the reason behind the very few models available today.

Even more critical is the situation for wall-bounded turbulence, where the non-isotropy hypothesis complicates the mathematics even more. Here, the focus is on the coherent motions characterising the logarithmic region and it is in this context that Townsend 1976 introduced the attached eddy hypothesis (AEH), one of the very few attempts in modelling wall-bounded turbulence. It can be considered the starting point of more recent proposals, laying their

fundamentals on Townsend's hypothesis, to then expand it to other regimes and tailor it for more specific flow-case.

The AEH is a conceptual model, that can be applied to inviscid, asymptotically high Reynolds numbers and throughout the years has gained more and more support by experimental results. It simplifies the complex architecture of the flow in the near-wall region with a system of geometrically self-similar, randomly distributed wall-attached eddies. The density of their population, increasing with Reynolds number, is inversely proportional to the distance from the wall. This means that eddies increase their size as moving away from the wall, but fewer and fewer as the distance increases. The consequence, completely independent from the geometry of the attached eddy, is a logarithmic behaviour of the normal Reynolds stresses  $u^2 = A_1 + B_1 \ln(y/\delta)$  and  $w^2 = A_2 - B_2 \ln(y/\delta)$  (where  $u^2$  and  $w^2$  are the streamwise and spanwise Reynolds stresses.  $A_1$ ,  $B_1$ ,  $A_2$  and  $B_2$  are constants depending on the type of eddy chosen for the random distribution).

The key property of these eddies, from Townsend itself: *The velocity field of the main eddies, regarded as persistent, organised flow patterns, extend to the wall, and in a sense, they are attached to the wall.* Townsend 1976. This is a very crucial point in his theory. With the term "wall-attached" Townsend meant that for a distance from the wall,  $y$  in the log-region, the energy-containing motions are said to be attached in the sense that they feel the presence of the wall. In other words, the velocity field is influenced by the wall itself without being physically connected to it.

The model can be applied to the inviscid, asymptotically high Reynolds numbers wall-bounded flows. It does not model the viscous small-scale motions in the near-wall region, but it concerns only the inertia-dominated energy-containing motions inhabiting the log-layer.

The other key point of the Townsend's theory that is still object of intense debate is the geometry of the eddies. In his theory, Townsend is not committed to a specific geometrical shape, but the spirit is mainly directed to a "representative" type of eddy that allows to provide a description of as many features of wall-bounded turbulence and an explanation to the correlations and statistics observed.

However, this particular aspect of the theory sparked the interest of many, putting forward different suitable candidates for the attached eddies. For instance, Perry, Henbest, and Chong 1986 started from the double cone roller proposed by Townsend (which failed to predict the correct streamwise velocity) and following the studies of Head and Bandyopadhyay 1981, Theodorsen 1952 and Perry and Abell 1977, introduced the hairpin/ $\Lambda$  vortex, originating from the wall (even if that was not required from the AEH). Using the hairpin, they were able to reproduce the logarithmic profile of the mean velocity and the

spectral energy distribution characterised by the  $k_x^{-1}$  region in the streamwise velocity spectra (with  $k_x^{-1}$  being the streamwise wavenumber).

The velocity fluctuations induced by the attached eddies are, as matter of facts, the explanation of the  $k_x^{-1}$  region Marusic and Monty 2019. Several issues make this method not optimal: the limited extent of the  $k_x^{-1}$  region, the sensitivity to spectral aliasing (Davidson, Nickels, and Krogstad 2006) and the unavoidable need of correlations with the near-wall region if the both the wall-attached and self-similar nature want to be investigated. For this reasons, conclusions coming from multi-point measurements are preferred: if Baidya et al. 2019, Tutkun et al. 2009 have investigated the matter in the spanwise direction, Baars, Hutchins, and Marusic 2017 verified the AEH for turbulent boundary layers and surface layers in the wall-normal direction given the ease in covering a wide distance. These type of measurements are also convenient to assess the self-similarity of the structures (Fig.2.7).

This term implies two main features for the characteristic eddies: that the energy density of the eddies is constant and in the geometrical sense, that their size scales only with the distance from the wall. Given the strength of this hypothesis, which is crucial for the mathematical description of numerous aspects of turbulence, many studies concentrated on verifying the self-similarity of the structures populating wall-bounded flows.

For instance, the seminal work by Baars, Hutchins, and Marusic 2016, investigated the self-similar nature of the structures in the wall-normal direction of turbulent boundary layers for more than a decade on Reynolds numbers. His coherence spectra showed self-similar eddies with an aspect ratio of 14.

The continuous efforts made to improve and verify the attached eddy model are due to the already promising results that made this model widely popular. For instance it is widely used in models to predict friction, in two-point measurements to study the rate of energy dissipation in wall-bounded turbulence Mouri 2017 and in the study of atmospheric surface layers (Katul and Vidakovic 1996, Hunt and Carlotti 2001, McNaughton 2004, Kunkel and Marusic 2006 and Hutchins et al. 2012).

These are only few examples of how it is undeniably useful in applications of industrial interest, but there is more. It would act as a reference to validate wall-bounded turbulence theories as it allows prediction of statistics for the energy containing motions. Further studies are required to overcome the current limitations: it allows only the modelling of the attached eddies and as purely kinematic model, if we want to extend it to flow control applications, then the dynamics should definitely be incorporated.

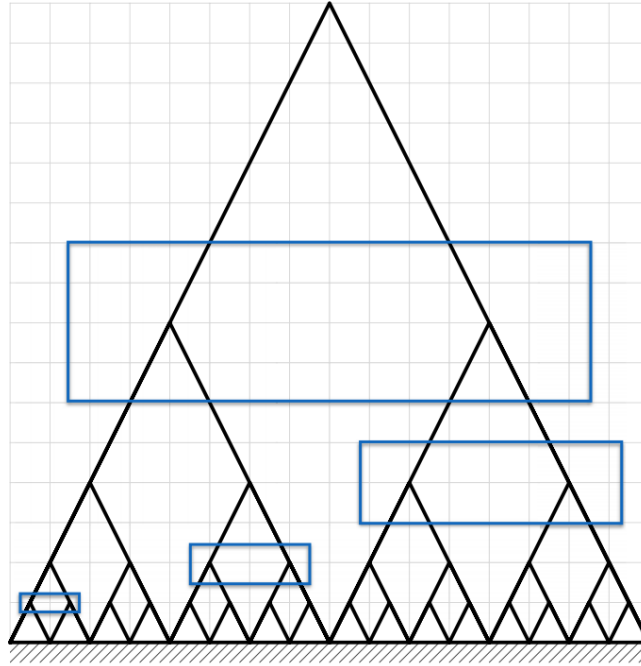


Figure 2.7: Conceptual for a system of self-similar attached eddies. The blue rectangles highlight the areas where a self-similar pattern is observed. Reprinted from Woodcock and Marusic 2015.

#### 2.6.4. Interaction of turbulence scales

Classical turbulence theory predicts a near-wall region ( $0 < y^+ < 30$ ) where the velocity statistics averaged in time and normalised with the friction velocity depend universally on the distance from the wall  $y^+ = y\nu/u_\tau$ . This is known as *inner-scaling* and it is seen to fail for the fluctuating streamwise velocity in recent numerical and experimental studies. For instance, the work by Klewicki and Falco 1990 and Örlü et al. 2017 shows a variation of the inner-peak that goes beyond experimental uncertainty, suggesting a Reynolds number dependence. For turbulent boundary layers Marusic, Baars, and Hutchins 2017 suggested an explanation of this behaviour based on the attached eddy hypothesis, where the hierarchy of attached structures centered far from the wall cause large velocity fluctuations that superimpose their energy onto the near-wall streaks. This further hints at the crucial role of the large-scale contributions to the increase of the broadband turbulence intensity, completely excluding the small scales. Marusic et al. 2010 used a cut-off spectral filtering technique,

to decompose the fluctuations of the large and small scales. By isolating the contributions they were able to prove that in turbulent boundary layers the growth of the streamwise turbulent intensity can be related to an increase of the large scales' energy. Also the one-dimensional premultiplied energy spectra long suggested the primary responsibility of the large scales (Marusic et al. 2010). Comparing the spectra of the near-wall region, the collapse for different Reynolds numbers is observed only in high frequency domain (the small scales range), while at lower frequencies, the energy increases for increasing Reynolds numbers. It is important to stress the caution required when interpreting the data in the near-wall region at high Reynolds numbers, due to the possible insufficient spatial and temporal resolution issues P. M. Ligrani and Bradshaw 1987, Hutchins et al. 2009 that dampen the turbulent fluctuations. Despite the multitude of correction schemes suggested in literature, Smits et al. 2011, a great advancement in reaching a definitive answer can be propelled by high-resolution/high Reynolds numbers experimental facilities like CICLoPE.

The primary effect of the scales interaction is the linear superimposition of the large-scale energy onto the near-wall cycle. Despite being thought as autonomous (independent of external triggering to self-sustain Jimenez and Pinelli 1999), it is shown Hutchins and Marusic 2007b that for higher Reynolds numbers, the near-wall streaks are influenced by an increasing amount of large-scale energy.

The pure linear superposition is not the sole effect of the large-scale footprint in the near-wall region. Mathis, Hutchins, and Marusic 2009 demonstrated that the small-scale energy is in fact modulated both in amplitude and frequency by the superimposed footprints. Once the Reynolds number is high enough to ensure sufficient scale-separation between the small and the larger scales, the small structures will "feel" the footprint of the big scales as a modified boundary condition. For instance, large streamwise velocity fluctuations will cause a quasisteady period of locally increased shear stress. The small scales will, in turn, respond accordingly by proportionally increasing the velocity fluctuations amplitude.

An additional evidence of the link between the inner and outer region is the coherence spectra resulting from two-point synchronised measurements. Baars, Hutchins, and Marusic 2017 computed the Linear Coherence Spectrum using experimental and numerical data sets for turbulent boundary layers and atmospheric surface layers to represent the maximum correlation for a specific scale. This is particularly useful when verifying the validity of the classical scaling of the streamwise velocity fluctuations. Only the portion of turbulence in the near-wall region (the small scales) that is not coherent with the outer-region can be described with the classical universal dependence on the inner-scaled wall-distance  $y^+$ . It is the fluctuations in the outer-region, coherent with the inner-region (the "wall-attached" in the sense of Townsend), that will

grow with increasing Reynolds numbers, superimposing their energy onto the near-wall structures.

In conclusion, improving the knowledge on the interaction between the small and large scales would be extremely beneficial to formulate more accurate models. In this way it would be possible to predict near-wall statistics measuring in a much more accessible area, like the outer region and allow to simulate the evolution with the Reynolds number. For instance, the model proposed by Mathis, Hutchins, and Marusic 2009 assumes a universal near-wall signal that is modulated by the measured large-scale signal in the outer region.

## CHAPTER 3

### Facility and experimental set-up

The construction of this facility and the first set of mean flow statistics, spectral and quadrant analysis have been extensively presented in Fiorini 2017. The reader is referred to this for further discussion on the design. The motivation behind a high Reynolds facility and an overview of its layout are given in the following chapter.

#### 3.1. The need of a high Reynolds facility

The idea behind the construction of the CICLoPE laboratory, and in particular behind the design of the Long Pipe, is to allow to address critical research issues within the area of wall-bounded turbulence at high Reynolds number, combining for the first time well-established sensors and high accuracy. Despite high Reynolds number turbulence appears in numerous applications of practical industrial and environmental interest, its richness and complexity challenge both the numerical and experimental approach. If on one hand the current computer power is still not sufficient to obtain good statistics, spatial resolution becomes a severe hindrance when opting for an experimental method to investigate high Reynolds numbers regimes. The Long Pipe at CICLoPE was designed to allow fully resolved measurements using traditional instruments, not possible in any other facility in the world. The first requirement is to define the operational range of Reynolds numbers that should be guaranteed by the facility, referring to two fundamental features of high Reynolds numbers wall-bounded turbulence: a well-developed overlap region of the mean flow and a well-developed  $k^{5/3}$  region. It is well-known that in wall-bounded turbulent flows there is an overlap region where the mean flow is described by a logarithmic law (eq. (2.68)). The extent of the region is commonly accepted to be  $200 < y^+ < 0.15R$ , with the added requirement of stretching for at least a decade to ensure sufficient spatial resolution (until  $y^+ \approx 2000$ ,  $y = 2000l_*$ ), the constraint on the upper bound

$$2000l_* < 0.15R \quad (3.1)$$

leads to the lower bound of the operational Reynolds number ( $Re_\tau = Ru_\tau/\nu = R/l_*$ ) range  $Re_\tau > 1.33 \times 10^4$ . In order to be able to draw conclusions on the scaling behaviour of turbulent flows, a factor of 3 should be applied, leading

to a minimum highest Reynolds number of  $4 \times 10^4$ . For the appearance in the spectra of the  $k^{-5/3}$  region, according to the Kolmogorov theory and confirmed by numerical and experimental results, one should guarantee enough separation between the Kolmogorov scale  $\eta$  and the energy containing scales  $l_0$ , which for a pipe flow is the pipe diameter  $R$ . Physically it means that it should end at around a tenth of the wavenumber corresponding to the Kolmogorov scale, extending for one order of magnitude in the wavenumber-space, down to wavenumbers one order of magnitude smaller than the energy containing scales  $D$ . By using a numerical dataset, for  $Re_\tau = 14000$  the Kolmogorov scale at the centerline is  $\eta_{CL} \approx 10.6l_*$ . For the previous constraints, the  $k^{-5/3}$  region starts at around  $106l_*$  and stretches for a decade until  $1060l_*$ . The  $k^{-5/3}$  region should end at a wavenumber smaller than the one associated with the energy containing scales:

$$1060l_* < 0.1D \quad (3.2)$$

which in terms of  $Re_\tau$  means:

$$Re_\tau > 5.3 \times 10^3 \quad (3.3)$$

which is fulfilled from the fully-developed overlap region constraint. The conclusions of these discussions led to set the operational range to  $1.3 \times 10^4 < Re_\tau < 4 \times 10^4$ . The next step is to design the facility so it is able to reach high Reynolds numbers. Starting from its definition:

$$Re = \frac{\rho UL}{\mu} \quad (3.4)$$

multiple options exist to increase the Reynolds number. The most direct way to achieve this would be to increase the velocity  $U$ , but two are the main disadvantages of such method: a noticeable increase in the demand of the power will inevitably follow and the increment of the velocity is anyway limited by the onset of compressibility effects. A viable option is to decrease the viscosity  $\mu$ , as they do in cryogenic facilities. Another possibility is to pressurise the facility to increase the density, as implemented at the SuperPipe in Princeton where pressure at the test section can reach up to 187 atm and a maximum  $Re_\tau \approx 10^5$ . The strategy adopted in the large-scale facility at CICLoPE is to increase the characteristic length  $L$ , that in the case of a pipe flow is the radius  $R$ . As it will be shortly shown, this method preserves the spatial resolution that is instead damaged if any of the above methods is implemented. By considering the definition of the friction Reynolds number  $Re_\tau$ , the size of the small scales can be linked to the characteristic size of the facility,  $R$ :

$$l_* = \frac{R}{Re_\tau} \quad (3.5)$$

implying that, for a fixed outer dimension, an increase in the Reynolds number will inevitably lead to a decrease in the size of the small scales, cause of poor spatial resolution. This trend can be counterbalanced by increasing the size of the facility to a value that ensure a minimum  $l_*$  such that it can be still be measured by traditional measuring methods. Standard single hot-wire probes can be manufactured with a sensing length as short as  $120\mu$  m, up to a maximum of  $10l_*$  to avoid spatial averaging. This sets a lower limit to the viscous length scale  $l_*$  at  $12\mu$  m. Using eq. (3.5) and remembering that the facility needs to reach  $Re_\tau \approx 4 \times 10^4$ , we obtain that the radius of the Long Pipe should be 0.48m. The radius of the pipe is subjected to another constraint: the length-to-diameter ratio (L/D) of the pipe itself, a key feature of the design of pipe flow experiments. According to Zagarola et al. 1996, this parameter depends on two conditions that need to be verified: the length the boundary layer needs to grow and reach the center of the pipe, and the length required by turbulence to become fully developed. In both cases, the length grows with increasing Reynolds number. As discussed by Zagarola et al. 1996, a length of 100D (around 100m) is necessary to fulfill both requirements at the regimes investigated. Fig.3.1 clarifies the need of a large-scale experiment like CICLoPE without lowering the fluid viscosity to reach the high Reynolds numbers regime.

### 3.2. General construction

The basic assembly of the Long Pipe in CICLoPE consists in a closed-loop wind tunnel operating at atmospheric pressure and developing on two floors of the laboratory. The circular test section is 111.5m long (see Fig.3.2) and has a diameter of  $900mm \pm 0.2mm$ , resulting in a length-to-diameter ratio of  $L/D \approx 123$ . The pipe is composed of 22 elements, each 5m long, and a last one of only 1.5m where measurements are usually performed (3.3). Every element of the pipe is equipped with four static pressure wall taps, positioned in the streamwise direction and four metal access ports, azimuthally spaced and designed to sit flush with the inner surface of the pipe. Each element is made in carbon fiber, using the filament winding technology which allowed to meet the requirement of smooth internal surface, with a surface roughness of  $k_{rms} < 0.2\mu$  m (corresponding to  $k^+ < 0.02$ ). The test-section is linked to the return circuit, situated at the ground floor, through the shape converter, diffusers and corners.

Mass flow through the pipe is generated by the fan group, comprising two, two-stages counter rotating axial fans installed in series. The fan diameter is 1.8m, extending for 4.2m, absorbing a maximum power of 340kW. Each axial fan is provided with two propellers, mounted on a shared ac-motor powered by a frequency inverter for accurate velocity control. The fans are designed to produce a pressure increase of 6.5kPa, at a volume flow rate of  $38 m^3/s$ , which corresponds to a centerline velocity of  $60m/s$  at the test-section. During the

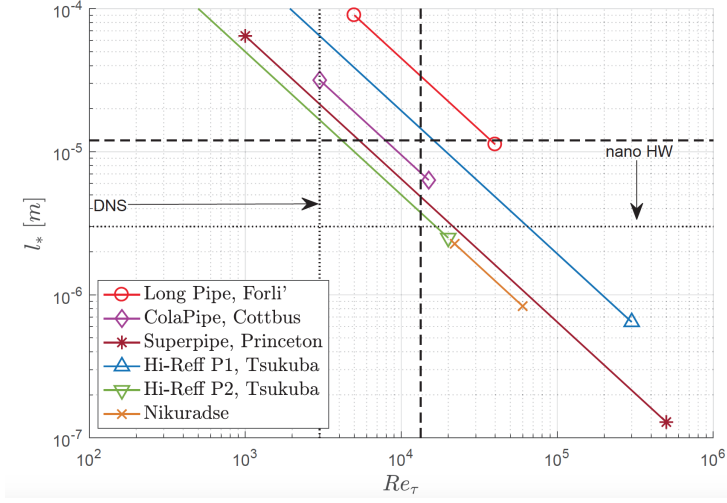


Figure 3.1: Range of Reynolds numbers vs viscous length scales for different pipe flow experiments and facilities. vertical dashed line represents the lower bound of the high- $Re_\tau$  region ( $\approx 13300$ ). The horizontal dashed line is the  $l_* > 10\mu m$  limit for sufficient spatial resolution. CICLoPE is designed to work in this region. Vertical dotted line is the highest reported DNS of a pipe flow ( $Re_\tau = 3008$  by Ahn et al. 2015). Horizontal dotted line is the fully resolved measurements for the NSTAP sensors by Bailey et al. 2010 of a sensing length of  $30\mu m$ .

experimental campaigns whose results are presented here, only one of the two fans was operative, allowing to reach a maximum centerline velocity at the test section of 40m/s. Noise-absorbing material coats a total length of 20m before and after the fan group, to reduce the noise produced and allow the wake of the fan to decay before the corner.

The closed-loop nature of the facility guarantees stable flow conditions and low turbulence levels. Excellent temperature control ( $\pm 0.1^\circ C$ ) of the air inside the pipe is obtained via the heat-exchanger located at the end of the return circuit and connected to the two-air conditioning systems, located just outside the site.

The flow conditioning section is composed of a honeycomb, 4 screens, a settling chamber and a 4:1 convergent.

### 3.3. Instrumentation

Measurements are performed at the test section of the Long Pipe, which is the 1.5m-long element, located at  $x/D \approx 123$ , just before the shape converter.



Figure 3.2: The Long Pipe at CICLoPE, 111.5m long and with a circular cross-section with a diameter of 0.9m.



Figure 3.3: Test section, located at  $x/D \approx 123$  from the convergent.

Here, the centerline velocity is usually monitored through an L-shaped Prandtl tube, mounted on the upper access port of the test section. The total and static ports are connected to an MKS Baratron 120AD differential pressure transducer, with a 1333 Pa range, acquiring the dynamic pressure at a rate of 10Hz.

When higher accuracy in measuring centerline velocity is required, as in the experimental campaign to determine  $\kappa_{CL}$  as discussed in chapter , a total head probe is used, installed on a supporting system vertically spanning the entire diameter and designed to minimise the blockage effect. In this case, the static pressure is acquired via one of the four static-pressure taps positioned every  $90^\circ$  around the circumference of the test section.

Given the confirmed axial-symmetry of the pipe (Fiorini 2017), any of the four taps can be used. The static-pressure taps have a diameter of 1mm and are placed on every pipe-element. In particular, for each 5m-element, 5 pressure taps are located 1m apart, and the last one (furthest from the convergent), 3 additional ones are positioned azimuthally every  $90^\circ$ . In the test section, being only 1.5m long, 4 taps are spaced around 30cm.

They are connected to a 32-channel digital pressure scanner Initium to acquire the static pressure at different locations the pipe. The pressure scanner has a 2500 Pa range and a manufacturer reported accuracy of  $\pm 1.25$ Pa. The acquisition frequency is kept at 5Hz and the results from each tap is averaged for the entire sampling time, to compute the pressure drop and consequently, the shear stress and the friction velocity  $u_\tau$ , crucial for turbulence scaling.

For the measurements presented in this thesis, as it will be detailed in chapter 5, up to 11 channels are retained for the linear fit to estimate the pressure drop, covering around 70m upstream the test section. Ambient pressure is acquired through a MKS Baratron 120AA absolute pressure transducer, with a 133322 Pa range. The ambient temperature is monitored through a PT 100 thermistor, secured inside the test section, used to retrieve air density.

Two types of traversing system are used to hold and move the probe used during the measurements. Both fit the 150mm round access ports, 4 for each pipe section, azimuthally equally spaced to allow different measuring stations, both in streamwise and azimuthal directions. The first traversing unit, used during the two-point correlation experimental campaign, is an hollow airfoil made in composite material, sliding through the wall. At the edge of the airfoil, the one inside the test section, the probe holder is mounted, and the cables are conveyed outside the pipe to be connected to the acquisition board through the cavity inside the airfoil. Since it was designed for near-wall measurements, it spans from the wall to a maximum distance of around  $0.3R \approx 13$ cm. It is operated with a stepper motor, with a resolution step of  $10\mu$  m, using a Renishaw Tonic T100x relative optical linear encoder to retrieve the position, with a  $0.5\mu$  m resolution. The advantage of fixing the linear encoder on the moving

part of the traverse system is that any play in the mechanism is accounted for during the acquisition.

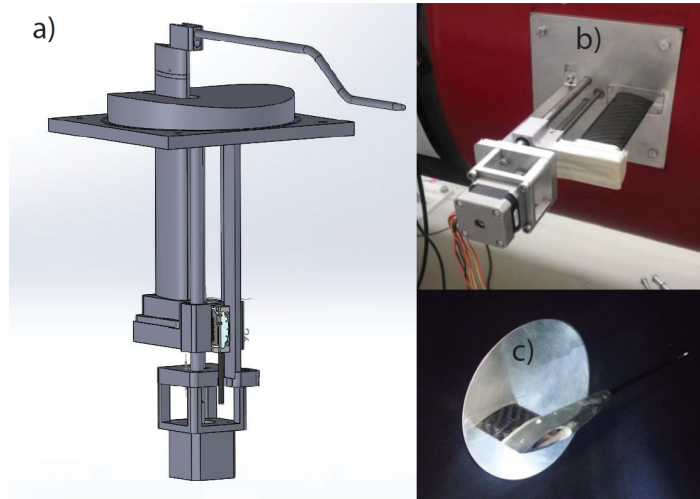


Figure 3.4: Small traversing (from Fiorini 2017). a) CAD model, b) part of the traversing outside of the test section, c) part of the traversing inside of the pipe.

The second traverse system was designed by Hutchins et al. 2011. The traversable sting was mounted at the test section, vertically spanning the entire diameter of the pipe and therefore requiring the access of two ports. To minimise the intrusivity, the sting has a NACA0012 profile, with a chord length of 69.3mm. It allows to perform wall scans from locations below the inner peak ( $y^+ < 10$ ) up to  $0.93R$  from the wall. The traversed distance is limited by the structural stability of the system when exposed to high flow velocity. It is connected to a stepper motor, allowing a minimum vertical step of  $8\mu\text{m}$ , and the position is retrieved using a Renishaw RG58C linear encoder with a resolution of  $0.1\mu\text{m}$ . In both cases, the steppers are operated with the National Instruments NI-9501 modules installed on the cRIO9-68 chassis, while the encoders are read via a NI-9401 digital I/O module.

A third traverse system, referred to as the "global-traverse" from here on, is used as support during the hot-wire calibration or to hold the total-head probe during centerline measurements. It was designed to span the entire diameter of the pipe, offering a greater degree of flexibility and it can host multiple probes, at the expenses of a higher blockage compared to the second traverse described, and obviously the "small" one. It is operated with a similar stepper motor as

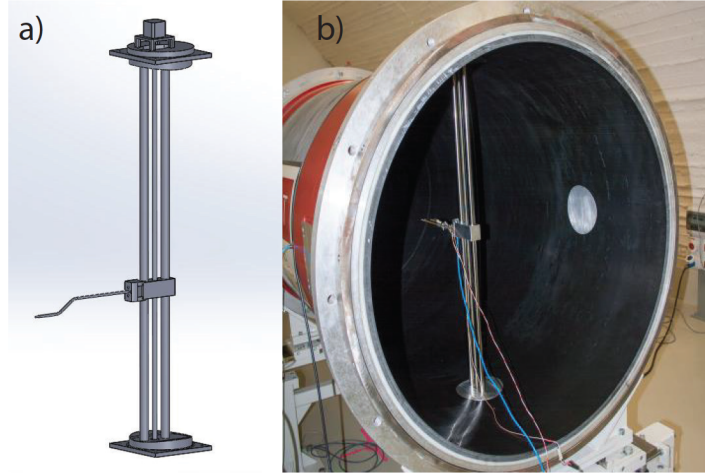


Figure 3.5: Global traverse (from Fiorini 2017). a) CAD model, b) Traverse as mounted at the test section.

the first traverse, but the position is retrieved through an integrated rotative encoder, mounted on the shaft.

### 3.3.1. Hot-wire anemometry

The hot-wire probes used are custom made single-wire boundary-layer type of probe, with a  $2.5\mu\text{m}$  Wollaston wire soldered on Dantec-style stainless steel prongs, with a nominal sensing length of 0.5mm, as shown in Fig.3.6, to keep the length-to-diameter ratio as close as possible to 200 as suggested by P. M. Ligrani and Bradshaw 1987. The hot-wires are operated in constant-temperature mode (CTA), by a Dantec StreamLiner 90N10 frame and 90C10 CTA channels with an overheat ratio  $a = (R_w - R_0)/R_0 = 0.8$ , where  $R_w$  is the working resistance of the wire when heated at operating temperature, and  $R_0$  is at cold/reference state. The working temperature of the wire,  $T_w$  is approximately  $250^\circ\text{C}$ , and the temperature coefficient is  $0.0039\text{ 1/C}$  for Platinum. The sampling frequency is set at 65kHz, with a low pass filter at 10kHz for all measurements presented. The signal is acquired through the National Instrument NI-9215 Analog Input module, mounted on the same cRIO 9068 chassis as the traverse system.

Calibration of the wire is performed *in-Situ*, mounting the probe on the global traverse at the test section, placed horizontally, and the hot-wire probe is positioned at the centerline of the pipe. The centerline velocity is monitored via the L-shaped Prandtl tube, mounted at the test-section using the upper access port, in order to place it as close as possible to the hot-wire without being



Figure 3.6: Single-wire, boundary-layer type of probe. Sensing length of the wire,  $L=0.5\text{mm}$ , diameter  $d=2.5\mu\text{m}$

excessively intrusive. The temperature of the flow is acquired as described above. The reference calibration temperature  $T_{ref}$  is obtained averaging the temperature during the entire process, while hot-wire voltage  $V$ , centerline flow velocity  $U$  and temperature are acquired for each point. Moreover, the voltage for each calibration point is corrected for possible temperature variation with respect to the mean temperature of the  $i$ -th point  $T_i$ , using the expression from Bruun 1995.

$$V_{corr}(T_{ref}) = V_m(T_i) \left(1 - \frac{T_i - T_{ref}}{a/\alpha}\right)^{-1/2} \quad (3.6)$$

where  $V_m$  is the voltage measured and  $V_{corr}$  is the corrected one. The calibration velocity range depends on the type of measurement and the maximum speed that will be reached. Where possible, the entire velocity range offered by the facility was spanned, acquiring more than ten points. The calibration coefficients and curve are obtained performing a least-square fitting with a fourth-order polynomial to the  $n$  calibration points:

$$U = c_0 + c_1V + c_2V^2 + c_3V^3 + c_4V^4 \quad (3.7)$$

where  $c_0 \dots c_4$  are the five calibration coefficients. Given the difficulties associated with calibrating at low speeds when *ex-situ* calibration is not possible, the voltage at zero speed is acquired and used as first point.



## CHAPTER 4

### Scaling of centerline velocity

In order to estimate the accuracy of the pressure drop along the pipe and its effects on the friction velocity and Von Kármán constant at the centerline  $\kappa_{CL}$ , measurements using a Pitot probe and a set of static pressure taps are performed. Instead of adopting an empirical approach, like in the work of Fiorini 2017 for the same facility, a systematic analysis is carried out. This chapter presents the results related to the pressure drop along the pipe and mean flow behaviour at the centerline for  $Re_\tau$  ranging from  $8.9 \times 10^3$  to  $3.9 \times 10^4$ .

#### 4.1. Experimental set-up

The pressure drop along the pipe is estimated by acquiring the static pressure at different streamwise locations along the pipe. The 1mm-diameter wall taps are connected to the digital pressure scanner Initem, with a reported accuracy of  $\Delta p = \pm 1.25 Pa$ , uncorrelated between the channels. A total of 19 channels are acquired at a sampling frequency of 5Hz for a one-minute period. The centerline velocity is monitored placing a Pitot-probe at the centerline of the test section, with an accuracy of 1mm, connected to the MKS Baratron 120AD differential pressure transducer. The final set-up is pictured in Fig.4.1 For a detailed description of the instruments used the reader is referred to chapter 2, while table 4.1 below reports the parameters characterising the flow for the  $Re_\tau$  investigated. Given the high accuracy required for this kind of experiments, extreme care is paid in choosing which pressure taps to retain to compute the pressure drop and which Pitot probe to use. The procedure is thoroughly described in 4.1.1 and in 4.2.1 respectively.

##### 4.1.1. Choice of the ports

Since the static pressure follows a linear decay for a fully developed turbulent pipe flow, the pressure drop can be estimated by linearly fitting the experimental data points. An important parameter is the length over which the fit is applied, i.e. the number of points that are considered in the fit. A detailed analysis on the effect of the number of taps on the pressure drop estimate can be found in Fiorini 2017, where 8 taps are used in the linear fit, covering a distance of about 40m upstream of the test section, corresponding to  $x/D=44$ . For the current experiment, up to 19 channels are acquired, extending to approximately 70m upstream the test section.

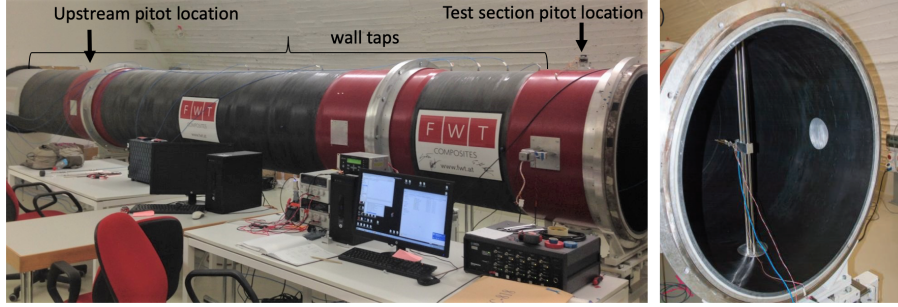


Figure 4.1: Left: a portion of Long Pipe in CICLoPE, where the location of the wall-taps and pitot probe are indicated.

Among the numerous methods to remove outliers when performing a linear fit, a "modified" version of the Montecarlo method is implemented. Instead of randomly perturb the data choosing a random value in the range  $[-1.25, +1.25]$ , the "distorted" static pressure from the  $i$ -th wall tap ( $p(x_i)$ ) is obtained by considering all possible combinations of the transducer accuracy:  $0, \pm 1.25\text{Pa}$ , for a total of  $3^N$  cases ( $N$  number of taps). For each combination the pressure drop is computed using the linear-square fit:

$$\frac{dp}{dx} = \frac{\sum x_i p_{fit}^{1+\alpha} \sum p_{fit}^\alpha - \sum x_i p_{fit}^\alpha \sum p_{fit}^{\alpha+1}}{\sum x_i^2 p_{fit}^\alpha - (\sum x_i p_{fit}^\alpha)^2} \quad (4.1)$$

where  $x_i$  is the location of the  $i$ -th pressure tap,  $p_{fit}$  is the value of the static pressure at the  $i$ -th location and  $\alpha$  is the weight of the least-square method, set to 1 as it has proven not to influence the results. The procedure is applied for all nine Reynolds numbers. To choose which ports to discard, the deviation from the linear fit is computed as the difference between the experimental pressure data and the value of the linear fit at the same location  $x_i$ :

$$p_{dev}(x_i) = p(x_i) - p_{fit}(x_i) \quad (4.2)$$

Fig.4.2 shows the deviation from the linear fit of the static pressure from 15 of the 19 ports that are initially considered for the determination of the pressure drop. The taps located at 69.25m and 94.225m from the inlet of the Long Pipe are discarded in the first iteration, since their deviation is noticeably larger than the specified transducer accuracy  $\Delta p$ , for all nine Reynolds numbers investigated. The iteration continues until the resulting mean value of the pressure drop of the current iteration is within the standard deviation of the previous one, suggesting that the choice of the pressure taps and their location is not critical. The results for 11 and 7 taps are summarised in Table 4.1. Based on these observations, it is decided to retain 11 taps for the computation of the

$Re_\tau$	Mean		Standard deviation	
	7 taps	11 taps	7 taps	11 taps
$8.1 \times 10^3$	0.402	0.407	0.032	0.0275
$1.3 \times 10^4$	0.9485	0.951	0.0325	0.028
$1.6 \times 10^4$	1.656	1.659	0.0325	0.0275
$2.1 \times 10^4$	2.6355	2.636	0.0326	0.028
$2.5 \times 10^4$	3.752	3.752	0.0325	0.028
$2.9 \times 10^4$	5.135	5.133	0.0325	0.0275
$3.3 \times 10^4$	6.699	6.699	0.0325	0.0275
$3.7 \times 10^4$	8.485	8.483	0.0325	0.0275
$3.9 \times 10^4$	9.725	9.720	0.0325	0.0275

Table 4.1: Comparison between mean and standard deviation of pressure drop when 7 and 11 taps are retained for the linear fit.

pressure drop along the pipe, whose deviation from the fit is shown in 4.3. In Fig.4.4 it is shown the mean pressure measured for each of the 11 taps used for the fit, for the 9 Reynolds numbers investigated. The  $\Delta p$  reported on the y-axis refers to differential static pressure measured along the pipe, using the first pressure tap after the test section as reference. The dashed lines represent the linear fit obtained with the least-square method, to compute the pressure drop.

From the standard deviation of the error of the fit, the 95% confidence interval for the slope of the linear regression  $p_{fit} = x_i \frac{dp}{dx} + b$  can be computed; for a distribution of  $n$  points, 11 in this case, with coordinates  $(x_i, p_i)$ , in absolute value [Pa/m] (from Bendat and Piersol 2011):

$$95CI = \sqrt{\frac{\sum_{i=1}^N (p_i - p_{fit})^2}{N - 2}} \cdot \sqrt{\frac{1}{\sum_{i=1}^N (x_i - \bar{x}_i)^2}} \cdot t_{N-2, \alpha/2} \quad (4.3)$$

The results are then normalised with the mean value of the pressure drop for each Reynolds number to obtain the percentage variation:

$$95\% = \frac{95CI}{\mu_{dp/dx}} \quad (4.4)$$

Results for the nine Reynolds numbers are shown in Fig.4.5. The error is seen to be constantly around 0.5% except for the two lowest Reynolds numbers, where transducer accuracy has a greater impact.

## 4.2. Centerline velocity measurements

From the derivation of the pressure gradient it is possible to estimate the friction velocity  $u_\tau$  exploiting the geometry of the pipe, yielding:

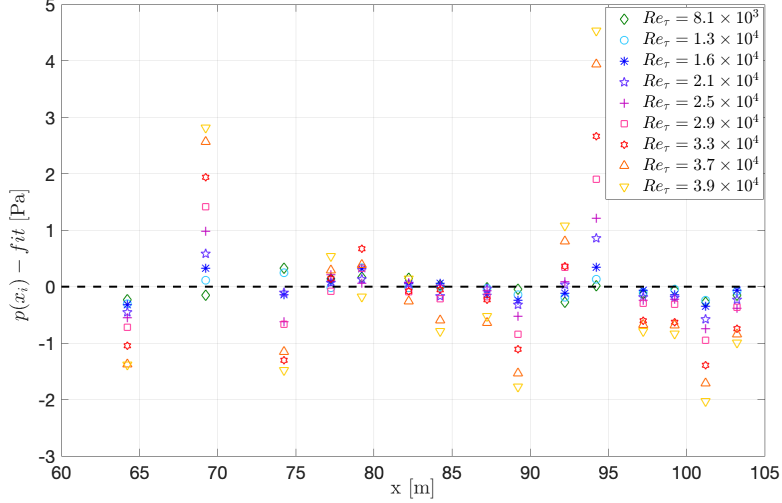


Figure 4.2: Deviation from the linear fit for each of the 15 taps retained for the 9  $Re_\tau$ .

$$u_\tau = \sqrt{\frac{\tau_w}{\rho}} \quad (4.5)$$

with  $\tau_w$  being the wall shear stress, defined as in eq.(2.56). The friction Reynolds is now introduced as:

$$Re_\tau = \frac{u_\tau R}{\nu} \quad (4.6)$$

By combining the log-law and the velocity-defect law introduced in 1, the centerline relation can be obtained in the form:

$$U_{cl}^+ = \frac{1}{\kappa_{cl}} \ln(Re_\tau) + C \quad (4.7)$$

Where  $U_{cl}^+ = U_{cl}/u_\tau$  is the inner-scaled centerline velocity, C is the sum of the additive constants of the two equations. The asymptotic matching of the inner and outer region through the logarithmic region discussed in Coles 1956b, requires  $\kappa = \kappa_{cl}$ , with  $\kappa$  being the Von Kármán constant governing the logarithmic law. As extensively reported in the literature review in chapter 2,  $\kappa_{cl}$  for the pipe flow from different facilities has constantly remained larger than

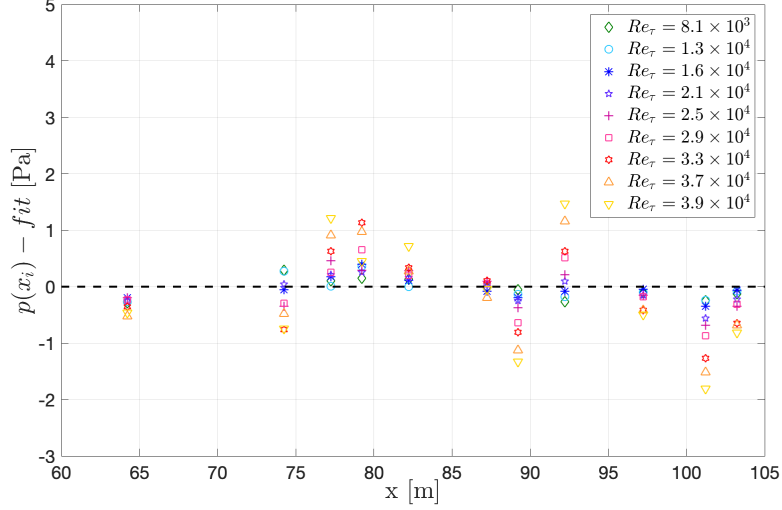


Figure 4.3: Deviation from the linear fit for each of the 11 taps retained for the 9  $Re_\tau$ .

0.42. This value is still considerably higher than the Von Kármán constant calculated by fitting the mean velocity profile in the logarithmic region, which for the Long Pipe is reported by Fiorini 2017 to be  $\kappa = 0.39$ . To assess whether it has a physical significance or it is solely due to experimental uncertainty, pressure drop acquisitions and centerline velocity measurements are simultaneously performed. First, the value of  $\kappa_{cl}$  for the Long Pipe is computed. Then, a detailed uncertainty analysis is performed on the pressure measurements, to assess the influence of the uncertainty of  $u_\tau$  on the value of  $\kappa_{cl}$ , and therefore the statistically significant difference between  $\kappa_{cl}$  and  $\kappa$ .

#### 4.2.1. Pitot probes

The centerline velocity  $U_{cl}$  is estimated as:

$$U_{cl} = \sqrt{\frac{2\Delta p}{\rho}} \quad (4.8)$$

where  $\rho$  is the air density and  $\Delta p = p_{tot} - p_{static}$ , acquired through a Pitot probe connected to a MKS Baratron AD differential pressure transducer. In order to improve the Pitot probe measurements of the centerline velocity, in terms of probe deflection and vibrations when exposed to the highest flow speeds, three

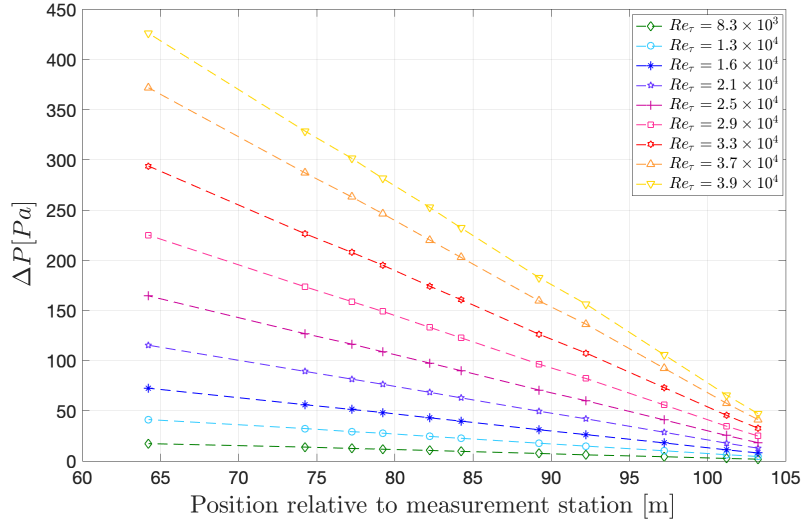


Figure 4.4: Differential pressure measured at each of the 11 taps along the pipe, using the first tap after the test section as reference, for the range of Reynolds numbers investigated. Only the taps retained in the linear fit are shown. The dashed lines are the linear fit obtained with the least-square method.

Type of probe	Outer diameter [mm]	Inner diameter [mm]
Pitot-static #1	6	1.8
Total-head #2	1	0.2
Total-head #3	3	1

Table 4.2: Geometrical characteristics of the three probes tested.

types of probes (in Fig.4.6) are tested. Geometrical characteristics are listed in table 4.2 above.

In the case of the Pitot tubes, the static pressure is acquired from the tap located at the bottom of the pipe circumference at the same location as the probe, as detailed in Nagib et al. 2017. Each probe is mounted at the test section of the Long Pipe, at  $x/D = 122$ , since Fig.4.7 shows that placing the probe at the test section or  $5.5D$  upstream does not affect the results. The first probe is mounted on a supporting system designed to minimise the blockage effect, whereas the other two are installed on a traverse system spanning the entire diameter of the pipe. A preliminary investigation on the behaviour of the probes and their support systems is carried out, to look for possible

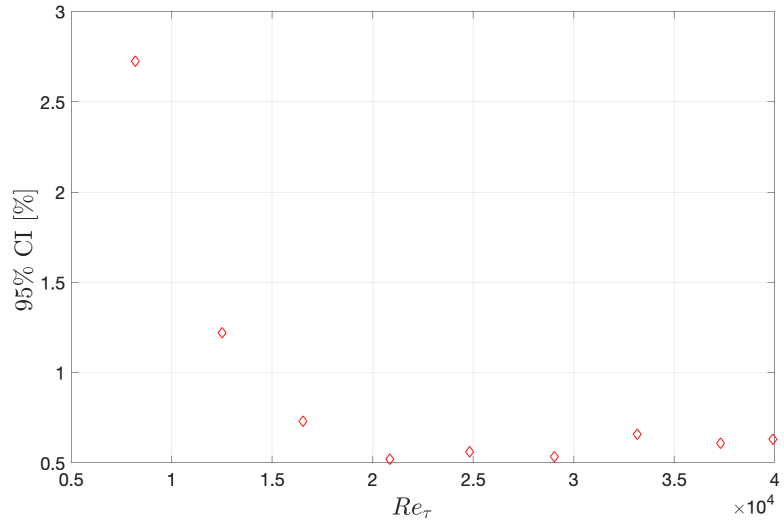


Figure 4.5: 95% confidence intervals, in [%] for the pressure drop acquired for  $9 Re_\tau$ .

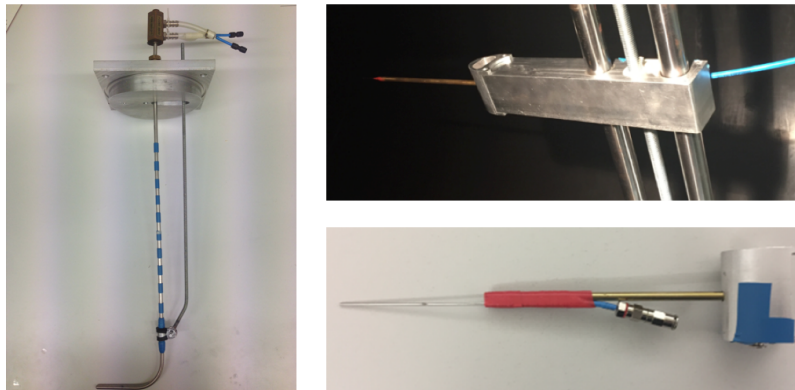


Figure 4.6: Left: probe #1. Bottom right: probe #2, top right: probe #3.

vibrations and deflections, monitored through a glass window mounted at the probe location. Probe #1 is seen to vibrate at the highest velocities, therefore a stabilising brace is added to the stem, which is in turn periodically thickened with tape to reduce the Von Kármán vortex shedding, without compromising

Fan speed [%]	Pitot static	Top	Front	Bottom	Back
40 %	16.89m/s	16.81m/s	16.83m/s	16.81m/s	16.81m/s
100 %	43.60m/s	43.34m/s	43.36m/s	43.36m/s	43.40m/s

Table 4.3: Comparison of the centerline velocities obtained using the Pitot-static and the four wall taps.

the blockage. Contrary to the Pitot-static, the two total-head probes show no sign of vibration nor deflection. Subsequently, the axi-symmetry of the flow is verified by alternatively acquiring the static pressure from each of the four taps around the test section. The symmetry of the pipe is confirmed by variations of less than 0.15% between the resulting velocities obtained by using the four taps, and around 0.5% compared to the Pitot static port, as reported in table 4.3.

To benchmark the different probes performances and evaluate the corresponding centerline velocity measurements, the bulk velocities  $U_{bulk}$  estimated from the pressure drop at the contraction entrance to the pipe are used. The bulk velocity is computed by employing the Bernoulli's theorem, valid for incompressible and irrotational flows:

$$p_1 + \frac{1}{2}\rho v_1^2 = p_2 + \frac{1}{2}\rho v_2^2; \quad (4.9)$$

with the indices 1 and 2 denoting the entrance and the exit of the convergent, respectively. Therefore,  $p_1$  and  $p_2$  are the static pressures and  $v_1$  and  $v_2$  the mean velocities of the two sections, since the viscous losses can be considered negligible in the convergent, any variation in pressure can be regarded as solely caused by a velocity variation:

$$\frac{v_1}{v_2} = \frac{A_2}{A_1}; \quad (4.10)$$

with  $A_1$  and  $A_2$  being the cross-sectional areas. Since the contraction ratio of the convergent of the Long Pipe in CICLoPE is  $CR = A_1/A_2 = 4$ ,  $v_1 = \frac{1}{4}v_2$ . Substituting in eq.(4.9), it yields to:

$$v_2 = \sqrt{\frac{32(p_1 - p_2)}{15\rho}}; \quad (4.11)$$

Since  $v_2$  is the mean velocity at the exit section of the convergent, for mass conservation considerations it is the bulk velocity  $U_{bulk}$  at the test section. The trend of the bulk velocity with the centerline velocity at the test section for the three probes is shown in Fig.4.8, where a problem with probe #2 is highlighted, given the lower value of  $U_{CL}$ .

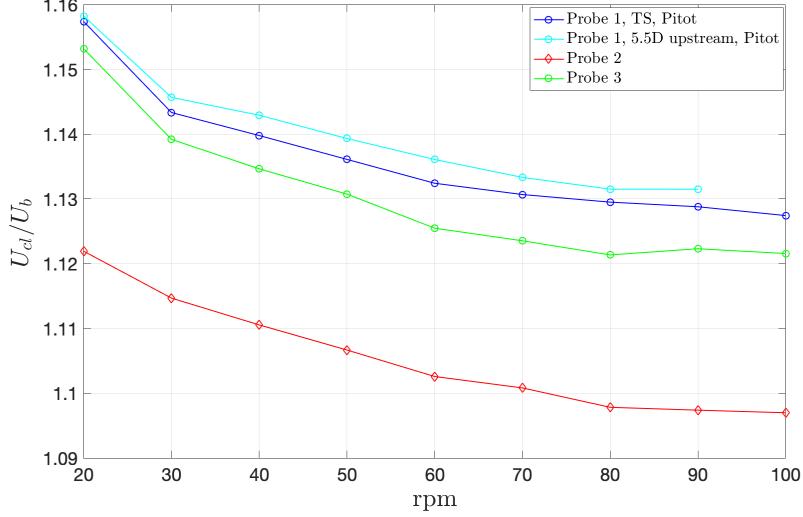


Figure 4.7: Ratio of centerline to bulk velocity versus fan speed.

Therefore, the results presented here are from probe #3, since from Fig.4.7 it has a lower blockage and its inner viscous-scaled diameter is such not to fall into the range of sizes that requires a correction. According to Mckeen et al. 2004 and Chue 1975, the geometry of the probe itself can influence the data. In the case of probe #2, yielding a considerable lower ratio of  $U_{cl}/U_{bulk}$  despite being mounted on the same traverse system as #3, the inner-diameter of  $d^+ = 20$  falls inside the range where viscous corrections are required. In Fig. 4.9 the inner-scaled centerline velocity is reported as function of the friction Reynolds number. The experimental data acquired for a range of Reynolds numbers from  $8.1 \times 10^3$  to  $3.9 \times 10^4$  are seen to follow the logarithmic decay. By fitting the data points in eq.(4.7), considering the entire range of Reynolds numbers acquired, the following relation is obtained:

$$U_{cl}^+ = \frac{1}{0.429} \ln(Re_\tau) + 7.25 \quad (4.12)$$

Comparing the present result with the panorama of pipe flow experiments in Fig.4.9, the value is in agreement with the recent work on the SuperPipe data by Cantwell Cantwell 2019, with  $\kappa_{CL} = 0.4311$  and  $C=7.3442$ . Except for the data by Monty 2005, obtained in another facility and at lower Reynolds numbers (up to a maximum of  $Re_\tau = 4000$ ), data are seen to agree well with results from other pipe flow facilities. On the other hand, it is worth to point out that Zanoun, Durst, and Nagib 2003 proposed values of  $\kappa_{CL}$  ranging from

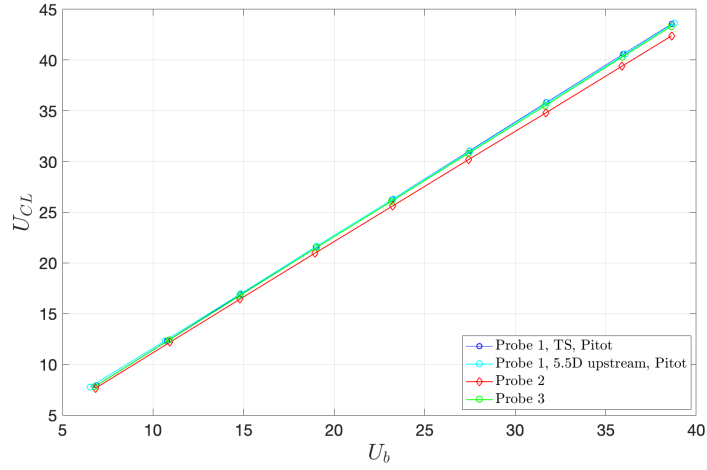


Figure 4.8: Bulk velocity as function of centerline velocity for the three probes tested.

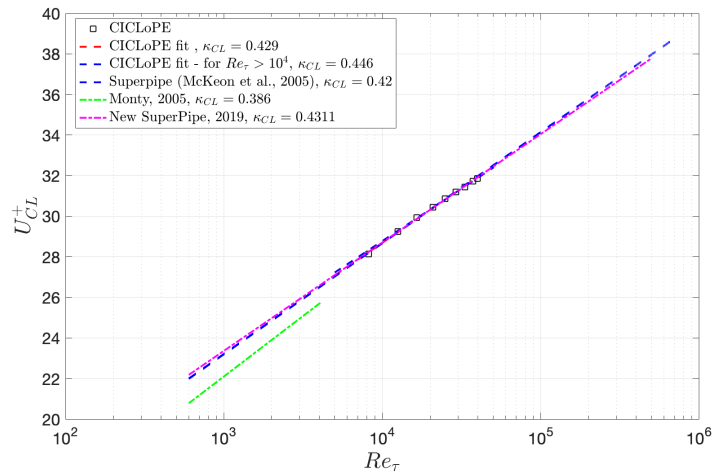


Figure 4.9: Inner-scaled centerline velocity vs friction Reynolds number. CICLoPE data fit, from  $Re_\tau = 8.1 \times 10^3$ ; CICLoPE data fit, from  $Re_\tau > 10^4$ ; SuperPipe data fit from McKeon, Zagarola, and Smits 2005; Monty 2005; SuperPipe data fit from Cantwell 2019

0.33 to 0.43. To verify the significant statistical difference between the  $\kappa$ s found with the fit of the logarithmic region of the mean velocity profile and the one obtained with the friction relation, a detailed uncertainty analysis is carried out. Since both  $U_{CL}^+$  and  $Re_\tau$  are functions of  $u_\tau$ , it is interesting to verify the sensitivity of the error on  $u_\tau$  for the estimation of the slope of their linear fit,  $\kappa_{CL}$ . Moreover, since the uncertainty on  $u_\tau$  can increase noticeably at low Reynolds numbers, its effect will be investigated. In this case, considering only  $Re_\tau > 10^4$ ,  $\kappa_{CL} = 0.446$ .

### 4.3. Uncertainty analysis

#### 4.3.1. Experimental data

A detailed uncertainty analysis is required to estimate how the experimental error on the pressure drop acquisition affects the  $u_\tau$  estimation, and therefore the value of  $\kappa_{CL}$ . In this way, we can investigate if it is possible to exclude the experimental uncertainty as cause of the difference between and the  $\kappa$  found with the fit of the mean velocity profile in the log-region (referred from here on with  $\kappa_{wall}$ ). Referring to the centerline logarithmic relation and the definition of  $u_\tau$  expressed in eq.(4.7), it is clear how the uncertainty on  $\kappa_{CL}$  is introduced by the uncertainties affecting the pressure drop along the pipe.

The sources of the uncertainty are essentially two: the random errors due to the accuracy of the Initium pressure scanner, reported by the manufacturer to be  $\pm 1.25$  Pa, and statistical convergence. Since the static pressure is acquired during the whole test, the dominating uncertainty is the one connected to the pressure scanner accuracy.

Among all possible methods to perform the uncertainty analysis, the Monte Carlo method is chosen, since it allows to explore the influence of the error distribution. Both a continuous and discrete error distributions are tested. In the case of the discrete error distribution, the extreme values of the transducer accuracy are taken ( $\pm 1.25$ Pa and 0) in order to investigate all possible combinations required to examine the worst case scenario. The two cases are discussed in the following:

- **Monte Carlo with continuous error distribution:** A random error in the range  $[-1.25; 1.25]$ Pa is added to the static pressure from each tap, iterating the process for  $N_{iter} = 10^4$ . The error distributions tested are gaussian and boxcar. The error changes with the tap considered and with the Reynolds number, since the pressure scanner used has  $N$  sensors and was re-zeroed after every acquisition. For each iteration  $i$  and for each Reynolds number tested  $j$ , the pressure drop  $\frac{dp}{dx}_{ij}$ , the friction velocities  $u_{\tau_{ij}}$  and the Reynolds numbers  $Re_{\tau_{ij}}$  are computed from the "perturbed" data. An example of the pressure drop distribution resulting from a gaussian error distribution for  $N$  iterations is shown in Fig.

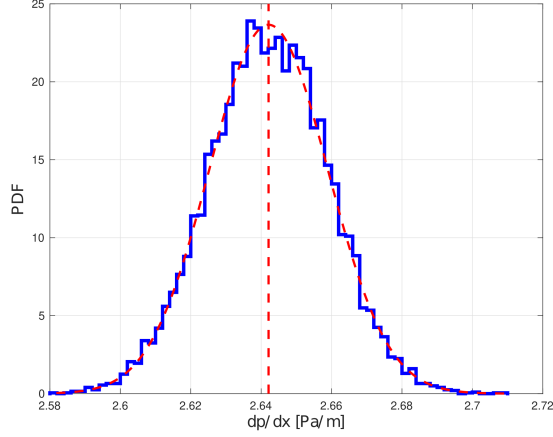


Figure 4.10: Pressure drop distribution for  $Re_\tau = 3.1 \times 10^4$  after applying the Gaussian error distribution,

4.10. For each iteration, the nine pairs of  $(U_{clij}^+; Re_{\tau ij})$  are linearly fitted to compute  $\kappa_{CLij}$ , shown for a gaussian error distribution Fig. 4.19, centered at  $\kappa_{CL} \simeq 0.435$ .

- **Monte Carlo with discrete error distribution:** All the possible permutations of the extreme values  $\pm 1.25\text{Pa}$  and  $0\text{ Pa}$  are computed, considering 11 pressure taps along the pipe and 9  $Re_\tau$ , as described in 4.1.1, resulting in 9 matrices  $3^{11} \times 11$ . Each line of the matrix is the error to be added to the static pressure from each tap. Each line then becomes the "perturbed" static pressure, now used to computed the "distorted" pressure drop  $\frac{dp}{dx_{ij}}$ . The resulting distribution for a Reynolds number is shown in Fig. 4.11.

Once all permutations are considered, the relative error of the pressure drop is computed as:

$$e_{dpdx_j} = \frac{\sigma_{dpdx_j}}{\mu_{dpdx_j}} \quad (4.13)$$

where  $\mu_{dpdx_j}$  and  $\sigma_{dpdx_j}$  are the mean value and the standard deviation of the pressure drop for the  $j$ -th Reynolds number, respectively. Following the error propagation theory, the error on  $u_\tau$  is defined as:

$$e_{u_\tau} = \frac{e_{dpdx}}{2} \quad (4.14)$$

and it propagates respectively on  $Re_\tau$  and  $U_{CL}^+$  as:

$$Re_{\tau,pert} = Re_\tau(1 + A \cdot e_{u_\tau}) \quad (4.15)$$

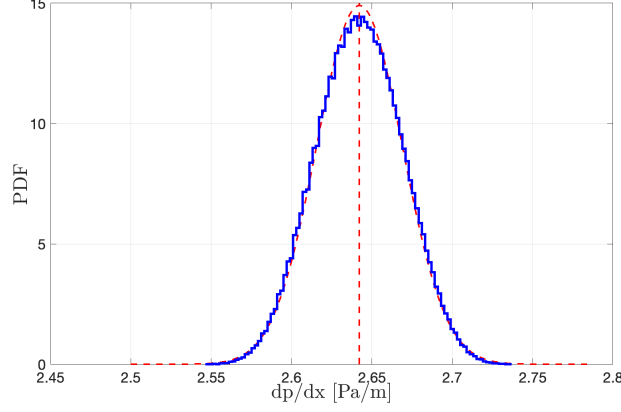


Figure 4.11: Pressure drop distribution for  $Re_\tau = 3.1 \times 10^4$  after applying the discrete error distribution method.

and

$$U_{CL_{pert}}^+ = U_{CL}^+ (1 - A \cdot e_{u_\tau}) \quad (4.16)$$

where A is the matrix composed of  $\pm 1$  and 0 to consider all the cases where the error is added (1), subtracted (-1) or 0 (0).

4.3.1a. *Friction velocity.* From the centerline relation 4.7, where  $U_{CL}^+ = U_{CL}/u_\tau$ , it is clear of  $u_\tau$  is a key parameter for the estimation of the  $\kappa_{CL}$ . Therefore, here we want to estimate the error in  $u_\tau$  to see later how it propagates on  $\kappa_{CL}$ . The methods described above are applied on the  $u_\tau$  resulting, for each iteration or permutation, from the "perturbed" pressure drop. For a fixed Reynolds number of  $3.3 \times 10^4$ , an example of PDF of  $u_\tau$  is shown in Fig.4.13. The PDF of  $u_\tau$  is seen to be indifferent to the shape of error distribution implemented in the continuous method, and the discrete method giving a broader distribution of value, since it considers all the possible cases. A detailed overview of the mean, standard deviation and errors affecting  $u_\tau$  in the three cases is reported from Fig.4.14 to Fig.4.16. It is confirmed that for the whole Reynolds number range the mean is not affected by the method used, and the percentage error obtained when the error analysis is performed with the discrete error distribution is slightly higher than that with the continuous error distribution.

Fig.4.17 and Fig.4.18 simulate the results if a more accurate pressure scanner is used. If for the current case of reported accuracy  $\pm 1.25 Pa$ , for  $Re_\tau > 10^4$ , the error is solidly lower than 1% when a continuous error distribution is applied, or slightly higher for the discrete error distribution, great improvements

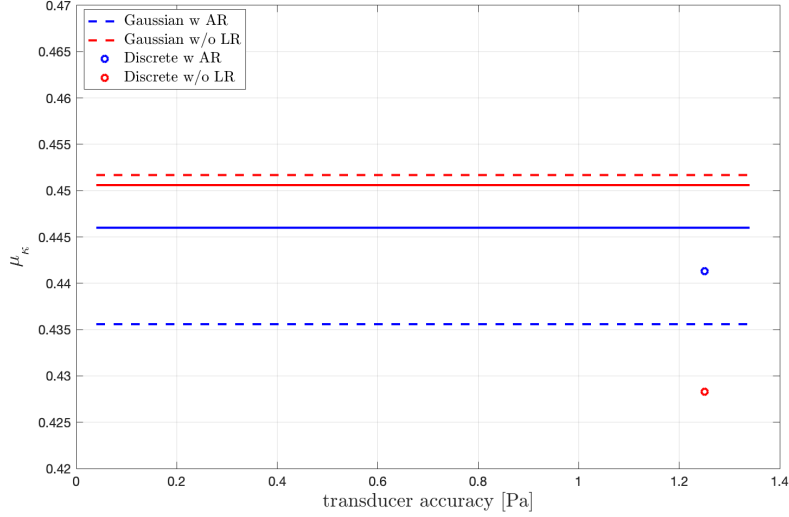


Figure 4.12: Comparison of the mean of the  $\kappa_{CL}$  obtained for each method described above. AR=all Reynolds numbers are considered, NL= the lowest Reynolds number is discarded.

on estimating  $u_{\tau}$  are seen already when using a pressure transducer with half of the uncertainty, for the error is well below 1% even at the lowest  $Re_{\tau}$ .

4.3.1b. *Centerline  $\kappa$* . For each "perturbed"  $u_{\tau}$ , the inner-scaled centerline velocity  $U_{CL}^+$  and logarithm of the friction Reynolds  $Re_{\tau}$  are computed, and the slope of linear fit of the two quantities is estimated. Its inverse represents the value of  $\kappa_{CL}$ . The error analysis is conducted in same way as the previous sections, and the resulting PDF distributions for the two methods are represented in Fig.4.19 and Fig.4.20, for the Gaussian and discrete error distribution respectively.

Particularly interesting is the resulting  $\kappa_{CL}$  distribution obtained with the discrete error distribution, shown in Fig.4.20. It presents a three-lobed PDF: one central "hump" at  $\kappa_{CL} \simeq 0.443$ , close to the one found for the continuous error method, and two symmetric humps at 0.37 and 0.53. As pointed out in Nagib et al. 2017, the three-lobed PDF reflects the dominance of the lowest Reynolds number in the least-square fit to determine  $\kappa_{CL}$ . In general, as shown in Fig. 4.12 the mean of  $\kappa_{CL}$  is not considerably affected by the choice of method implemented for the analysis, leading to a mean  $\kappa_{CL} = 0.4409 \pm 0.0054$ , corresponding to a variation of less than 1.5% between all the methods implemented.

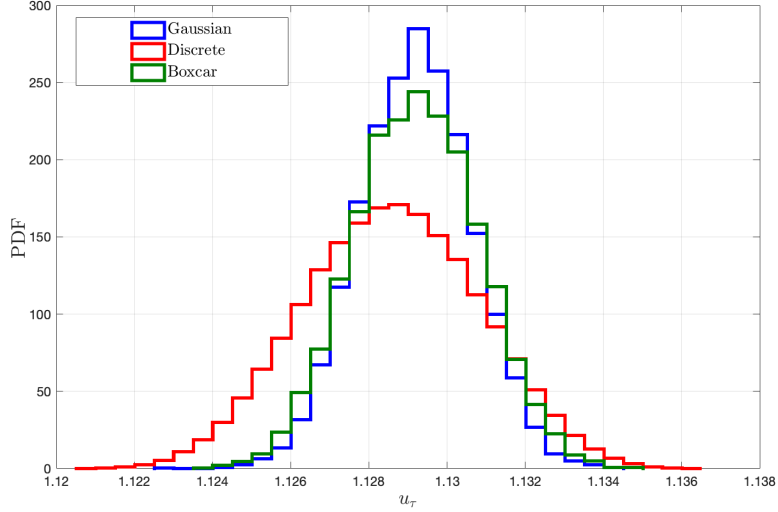


Figure 4.13: PDF of  $u_\tau$  resulting when applying the Montecarlo method with a Gaussian and boxcar error distribution, and discrete error distribution.

Unlike the mean, the standard deviation is instead influenced by the choice of method implemented, with a variation of around 15% between the cases (mean standard deviation of  $0.0624 \pm 0.009$ ), with the discrete error distribution, that considers all possible cases, leading to the highest standard deviation. As reported in Fiorini 2017, the uncertainty on friction measurements greatly affects the low-speed case, as show in Fig.4.21 where the static pressure measured along the pipe is plotted with  $\pm 1.25$  Pa error bars, reporting the transducer accuracy for  $Re_\tau = 3.1 \times 10^4$ . On the other hand, the effect is nearly absent in the high Reynolds numbers regime, where the uncertainty of the pressure scanner of  $\pm 1.25$  Pa becomes negligible. For these reasons, the effect of dropping the lowest Reynolds number is investigated, by repeating the analysis without considering it in the linear fit.

In this case, the mean value of  $\kappa_{cl} = 0.443 \pm 0.013$  is still inside the range of  $\kappa_{CL}$ s obtained considering all Reynolds numbers, and no clear pattern is visible in the behaviour of the magnitude of  $\kappa_{CL}$  when the lowest  $Re_\tau$  is neglected. The reason behind the decrease for the discrete error distribution is still not clear, but the value is still in the uncertainty range of the method. On the other hand, Fig. 4.22 highlights how dropping the lowest Reynolds number decreases noticeably the standard deviation in all cases, leading to a decrease of nearly 50% of the mean standard deviation, and therefore on the error on  $\kappa_{CL}$  that

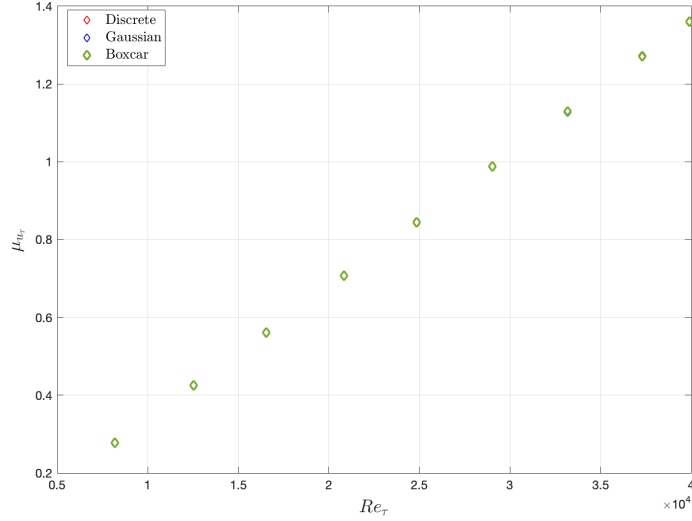


Figure 4.14: Mean of  $u_\tau$  for the 9 Reynolds numbers investigated applying the Monte Carlo method with a continuous (Gaussian and boxcar) and discrete error distribution.

Table 4.4: Comparison of mean and standard deviation of  $\kappa_{CL}$

Method	All Reynolds			No lowest $Re_\tau$		
	$\mu_{\kappa_{CL}}$	$\sigma_{\kappa_{CL}}$	error %	$\mu_{\kappa_{CL}}$	$\sigma_{\kappa_{CL}}$	error %
Gaussian	0.4353	0.0536	12.3 %	0.4517	0.0338	7.4 %
Boxcar	0.446	0.0619	13.9 %	0.4506	0.0381	7.4 %
Discrete	0.4413	0.0717	16.2 %	0.4283	0.0331	7.7 %

drops from around 14% to 7%, as seen in table 4.4. Moreover, the standard deviation becomes basically independent from the method used. The reason behind the low-Reynolds number effect, besides being linked to a not sufficient scale separation, could be the combination of log-scale and non-logarithmic spacing of the tested  $Re_\tau$ , making the error even larger at low values. The results are compared and summarised in table 4.4. Therefore, considering the range  $Re_\tau > 10^4$ , leads to a  $\kappa_{CL}$  well higher than the one found by fitting the logarithmic region of the mean velocity profile that does not follow inside the uncertainty range.

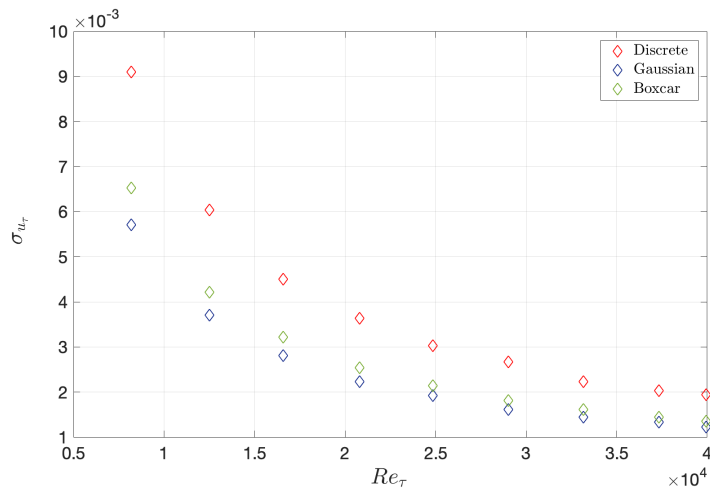


Figure 4.15: Standard deviation of  $u_\tau$  for the 9 Reynolds numbers investigated applying the Monte Carlo method with a continuous and discrete error distribution.

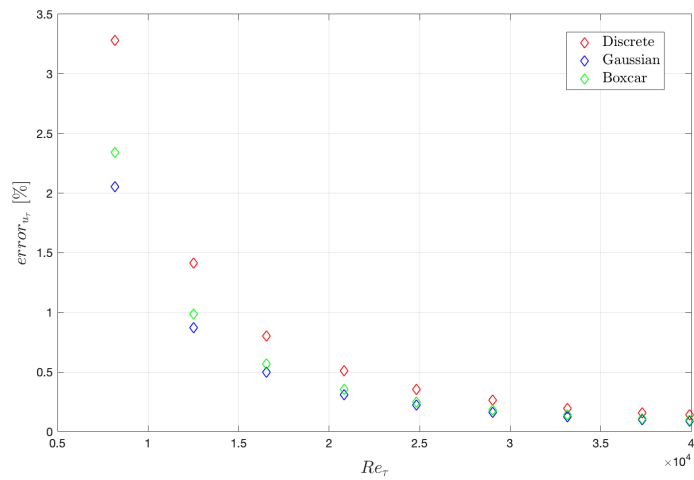


Figure 4.16: Percentage error on  $u_\tau$  for the 9 Reynolds numbers investigated applying the discrete error distribution and the Gaussian and boxcar error distribution.

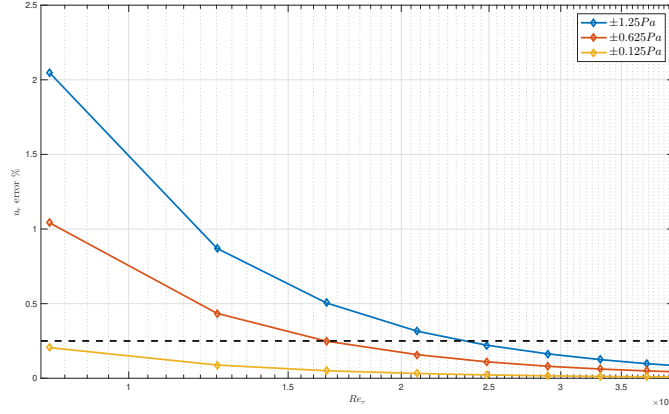


Figure 4.17: Percentage error on  $u_\tau$  applying a continuous gaussian error distribution, for three values of transducer accuracy.

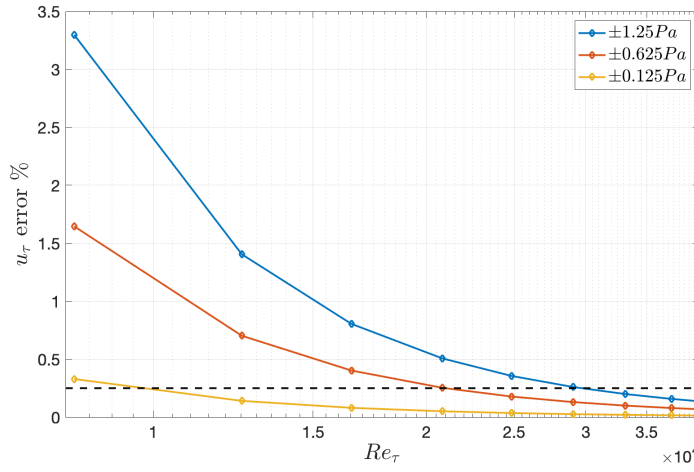


Figure 4.18: Percentage error on  $u_\tau$  applying the discrete error distribution, for the three values of transducer accuracy.

In conclusion, if we consider a range of Reynolds numbers ensuring a sufficient scale separation, for CICLoPE  $\kappa_{CL} = 0.44 \pm 0.03$ . This range excludes the value of  $\kappa_{wall}$ .

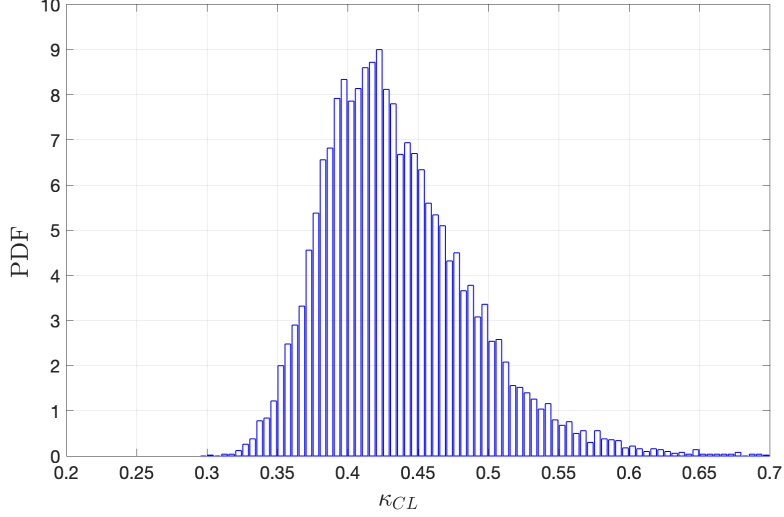


Figure 4.19: PDF of  $\kappa_{CL}$  resulting from a gaussian error distribution for the 9  $Re_{\tau}$ .

#### 4.3.2. Influence of transducer accuracy and Reynolds number range

In this section we want to investigate the effect of the pressure scanner accuracy and the range of Reynolds number considered, on the overall uncertainty. To do so, the error analysis is applied to artificially created data from the centerline fit obtained in the section above and the value of  $\kappa_{CL} = 0.42$  found by P. A. Monkewitz 2017 reanalysing the SuperPipe data. This allows to extend the investigation also on the initial guess of  $\kappa_{CL}$ . Starting from an arbitrary interval of friction Reynolds numbers, ranging from  $5 \cdot 10^4$  to  $10^5$ , the pressure drop along the pipe is retrieved. Using the wall taps locations, also the static pressure from each of the 11 taps retained in 4.1.1. Then, the inner-scaled centerline velocity is retrieved by inputting the value of  $\kappa_{CL}$  and the constant  $C$  found by fitting the experimental data. The functions, detailed below and represented in Fig. 4.23, are two pure logarithmic laws. The two sets of data created using the value of  $\kappa_{CL}$  found by fitting the experimental data and the value found by P. A. Monkewitz 2017 will be called Fit 1 and Fit 2 from here onwards:

- **Fit 1:**  $\kappa_{CL} = 0.429$  and the constant  $C = 7.25$  resulting from the linear fit of the experimental data.
- **Fit 2:**  $\kappa_{CL} = 0.42$ , according to the results by P. A. Monkewitz 2017. Minimising the error from the fit yields a  $C = 6.7$ .

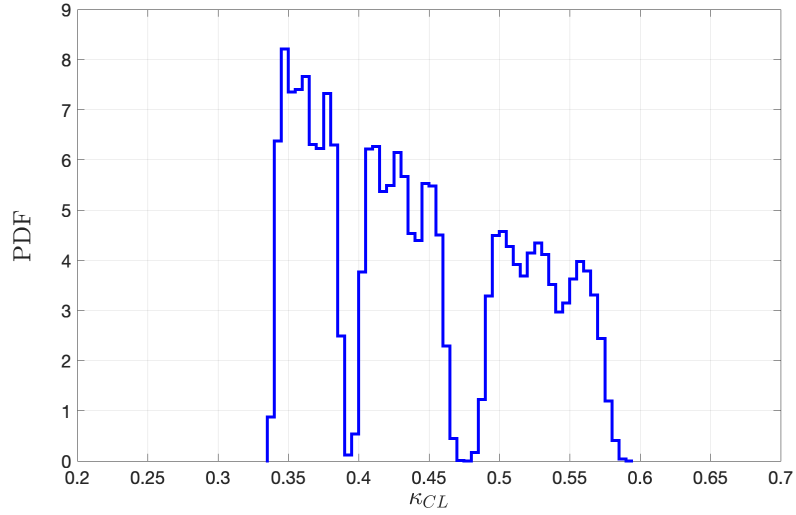


Figure 4.20: PDF of  $\kappa_{CL}$  resulting from the discrete error distribution for the  $9 Re_{\tau}$ .

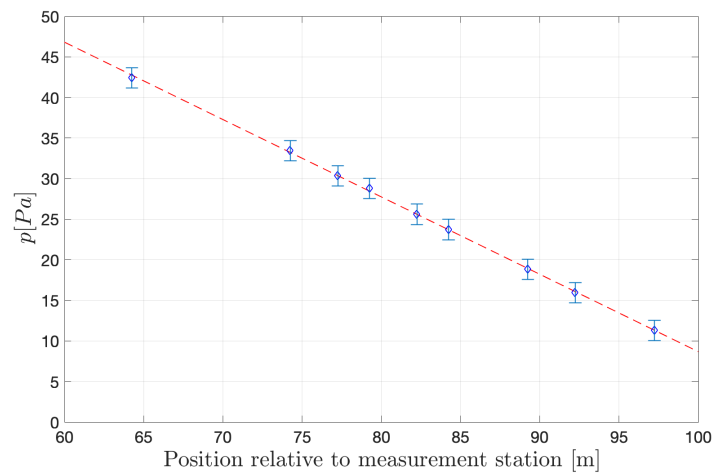


Figure 4.21: Static pressure acquired along the pipe for  $Re_{\tau} = 3.1 \times 10^4$ . Error bars report the  $\pm 1.25 Pa$  transducer accuracy.

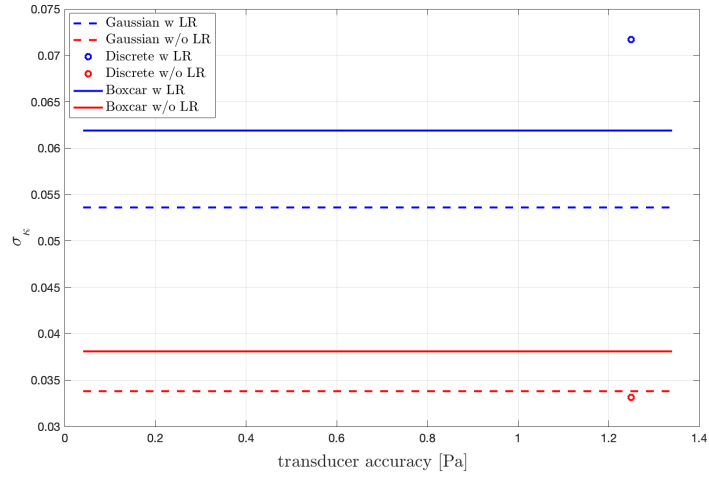


Figure 4.22: Comparison of the standard deviations of the  $\kappa_{CL}$  for each method described above. AR=all Reynolds numbers are considered, NL= the lowest Reynolds number is discarded.

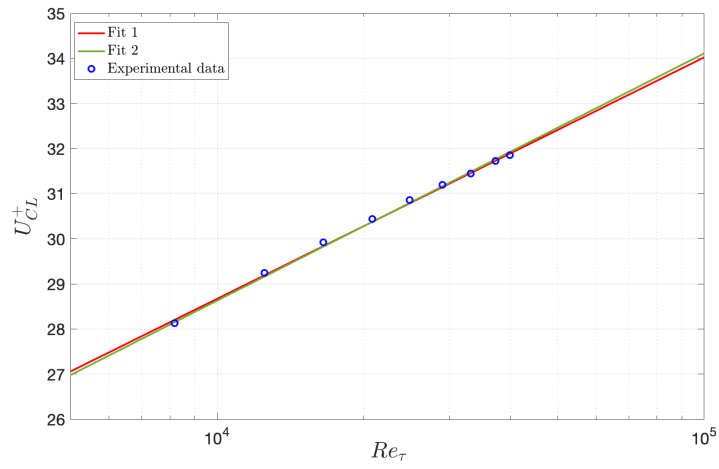


Figure 4.23:  $U_{CL}^+$  vs  $Re_\tau$  for the four synthetic set of data resulting from the four different fitting functions.

	Fit #1	Fit #2
All $Re_\tau$	0.0567	0.0613
No lowest $Re_\tau$	0.0546	0.0646

Table 4.5: RMSE for the four fits.

The deviation of the experimental data from each fit,  $e_{fit}$  is expressed in the form:

$$e_{fit} = \frac{\ln(Re_\tau)}{\kappa_{CL}} + C - U_{CL}^+; \quad (4.17)$$

where  $h$  is a parameter resulting from the fit. The results are reported in Fig.4.24 below and from which the root mean-squared error is computed as:

$$RMSE = \sqrt{\frac{\sum(e_{fit})^2}{N-3}}; \quad (4.18)$$

with  $N$  the number of points considered in the experimental linear fit ( $N = 9$  for the case of all  $Re_\tau$ ). The result for each fit is reported in table 4.5.

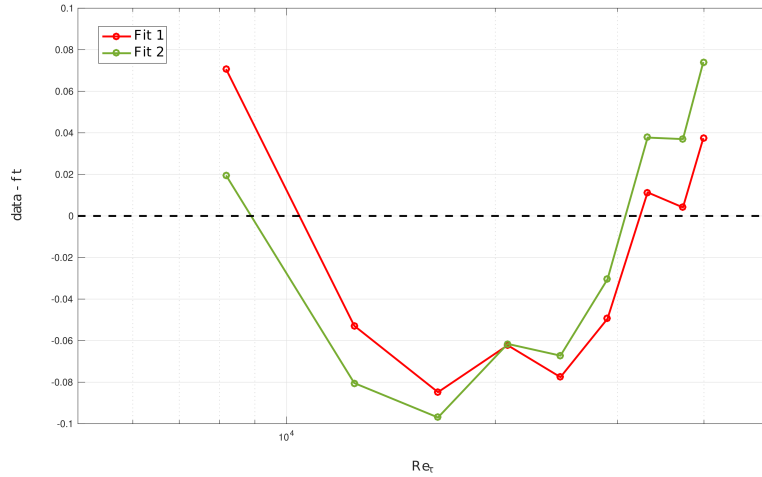


Figure 4.24: Deviation of the experimental data from the synthetic fit, for the four cases tested.

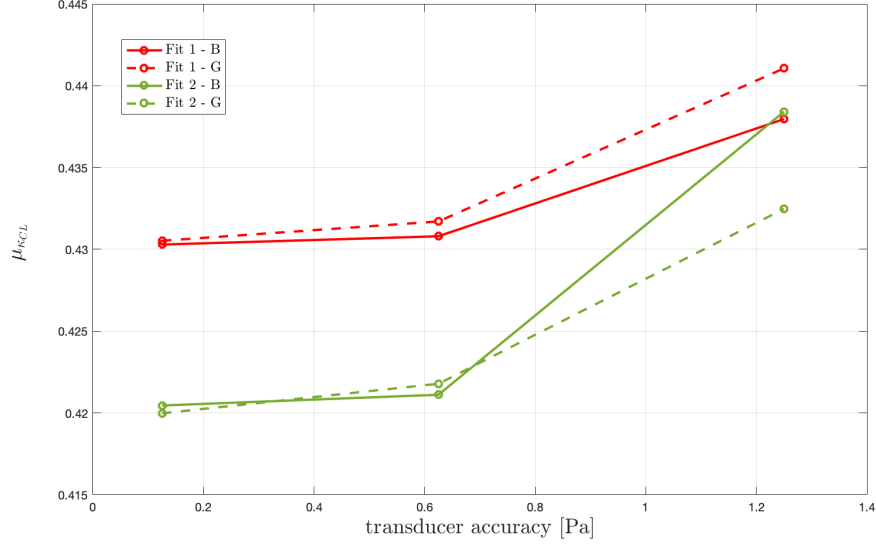


Figure 4.25: Comparison of the mean values of  $\kappa_{CL}$  vs pressure transducer error, for the two fits when the boxcar (B) and gaussian (G) error distributions are used. All Reynolds numbers are used in the fit to compute the  $\kappa_{CL}$ .

Each of the two resulting data sets is subjected to the uncertainty analysis. The static pressures are perturbed as for the continuous error distribution detailed in the previous sections, using three different error magnitudes:  $\pm 1.25 Pa$ ,  $\pm 0.625 Pa$  and  $\pm 0.125 Pa$ . As with the experimental data the effect of the lowest Reynolds number is assessed.

The choice of the error distribution is seen not to influence the value of the mean nor the standard deviation, even when the lowest Reynolds number is neglected in the linear fit to estimate  $\kappa_{CL}$ , as Fig. 4.25 to 4.28 show. Hence, the gaussian distribution is chosen to carry further on the error analysis. Dropping the lowest Reynolds number, the mean value of  $\kappa_{CL}$  becomes independent of the transducer accuracy, as Fig. 4.29 exhibits. As for the standard deviation, it is seen to drop noticeably, constantly below the 0.02 for all transducer's error values, as in Fig. 4.30. A summary of the results for a transducer accuracy of  $\pm 1.25 Pa$ , is reported in table 4.6. The analysis leads to the conclusion that if a sufficient scale separation is guaranteed, then the initial guess is seen not to influence the output. Moreover, the value of  $\kappa_{CL}$  is independent of the transducer accuracy and the error noticeably drops compared to a wider range of Reynolds that includes lower Reynolds numbers.

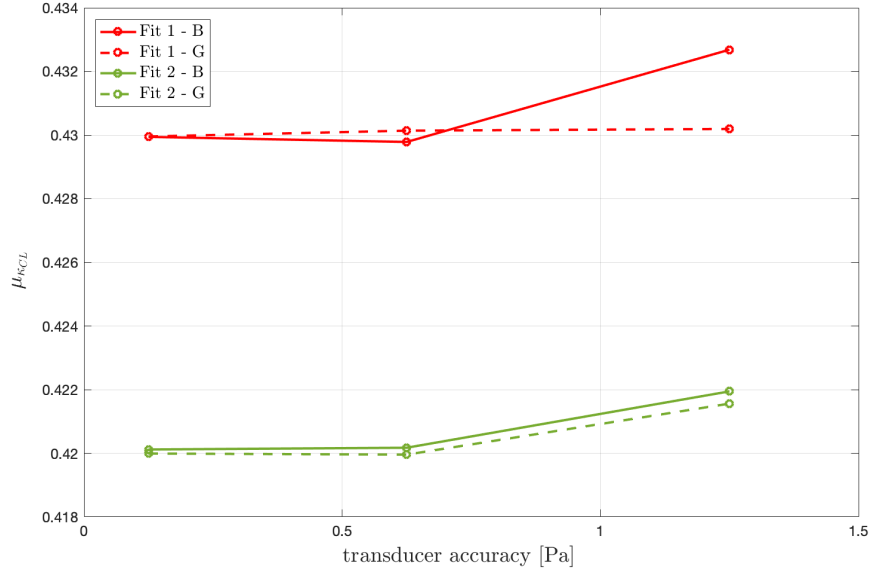


Figure 4.26: Comparison of the mean values of  $\kappa_{CL}$  vs pressure transducer error, for the four fits when the boxcar (B) and gaussian (G) error distributions are used. The lowest Reynolds number is discarded when computing  $\kappa_{CL}$ .

Table 4.6: Comparison of mean and standard deviation of  $\kappa_{CL}$

Method	All Reynolds			No lowest $Re_{\tau}$		
	$\mu_{\kappa_{CL}}$	$\sigma_{\kappa_{CL}}$	error %	$\mu_{\kappa_{CL}}$	$\sigma_{\kappa_{CL}}$	error %
Fit 1 - G	0.4411	0.0556	12.6 %	0.4302	0.0154	3.6 %
Fit 2 - G	0.4341	0.0555	12.7 %	0.4216	0.0148	3.5 %

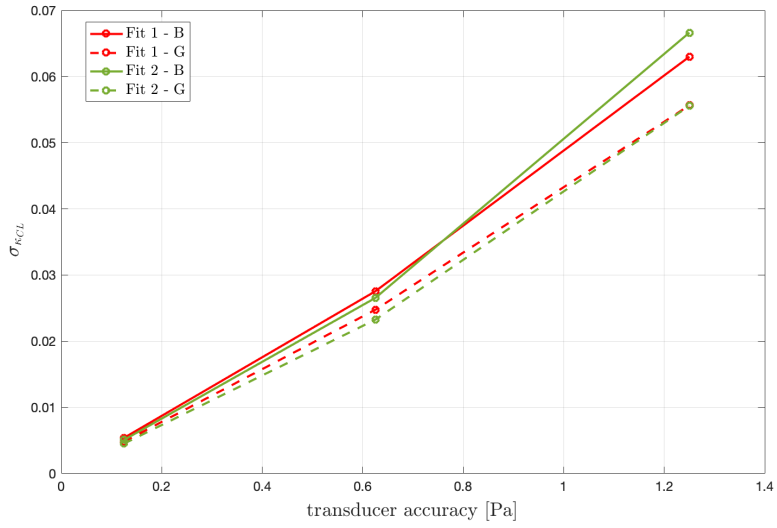


Figure 4.27: Comparison of the standard deviations of  $\kappa_{CL}$  vs pressure transducer error, for the four fits when the boxcar (B) and gaussian (G) error distributions are used. All Reynolds numbers are used in the fit to compute the  $\kappa_{CL}$ .

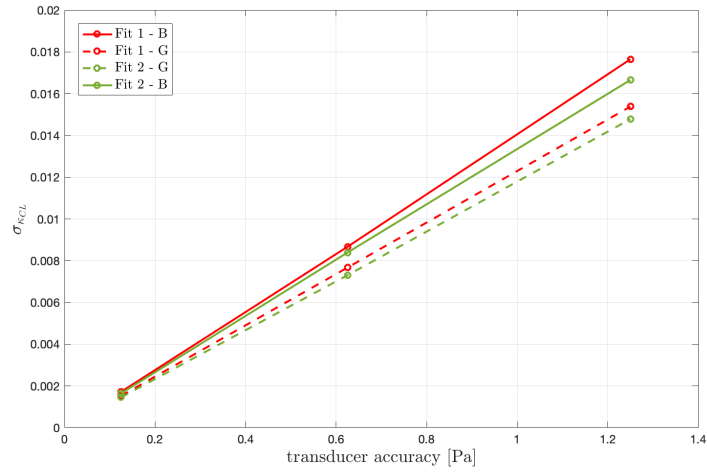


Figure 4.28: Comparison of the standard deviations of  $\kappa_{CL}$  vs pressure transducer error, for the four fits when the boxcar (B) and gaussian (G) error distributions are used. The lowest Reynolds number is discarded when computing  $\kappa_{CL}$ .

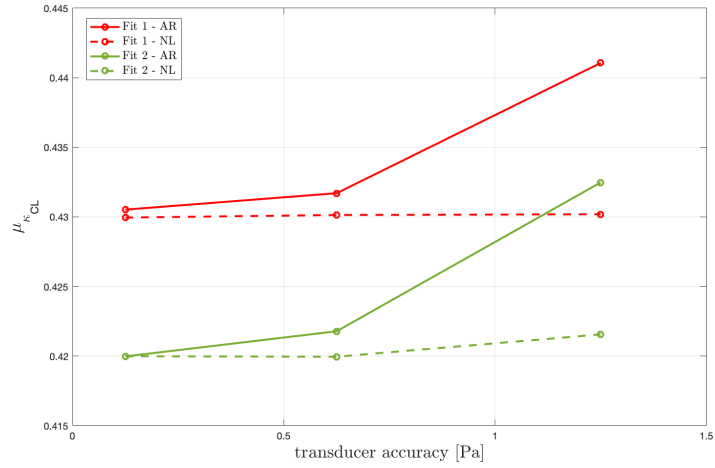


Figure 4.29: Effect of the lowest Reynolds number on the mean value of  $\kappa_{CL}$  for the four fits. AR=all Reynolds numbers are considered, NL= the lowest Reynolds number is discarded.

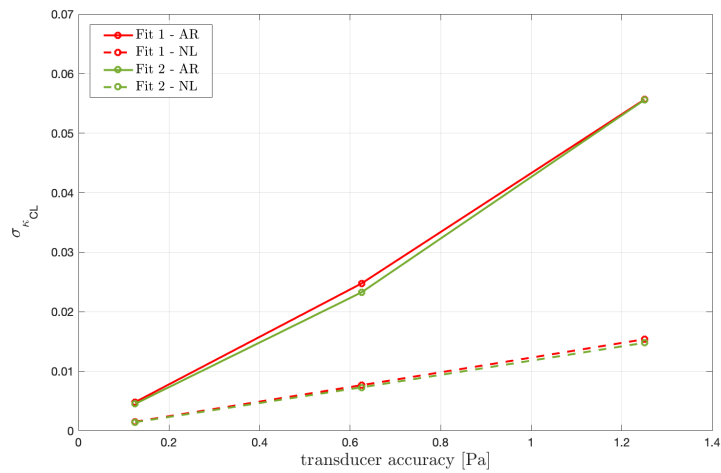


Figure 4.30: Effect of the lowest Reynolds number on the standard deviation of  $\kappa_{CL}$  for the four fits. AR=all Reynolds numbers are considered, NL= the lowest Reynolds number is discarded.



## CHAPTER 5

### Structures interaction

A characterising feature of turbulence is the presence of a wide range of scales. Small-scale motions, of the order of the viscous length scale  $l^*$  are found in the near-wall region. On the other hand, large-scale structures are centered far from the wall and they are seen to develop in the streamwise direction for more than 10 outer length scales, namely in the case of a pipe the radius  $R$ . Starting from a careful selection of the cut-off frequency to separate the small scales from the large, this chapter focuses on two aspects. First on investigating the individual contribution to the full-signal variance across a range of Reynolds numbers, and then on evaluating the interaction between the scales, since its existence would challenge the classical turbulence theory.

#### 5.1. Experimental set-up

Hot-wire anemometry measurements are performed at the test section of the Long Pipe, at  $x/D \approx 123$ . A boundary-layer-type of probe is mounted on the "second" traverse described in chapter 3, to scan the boundary layer from beneath the inner-peak ( $y^+ < 10$ ) to around  $0.93R$ . The sensing length of the wire is  $L=0.5\text{mm}$  with a diameter of  $2.5\mu\text{m}$ . The inner-scaled sensing lengths of the wire, together with all acquisition and run parameters of the cases tested, are reported in table 5.1 below. It shows that the higher Reynolds numbers cases are affected by spatial resolution issues, and *a posteriori* correction scheme needs to be applied. The wire is operated by the Dantec StreamLiner Pro in constant temperature mode, at an overheat ratio of 0.8. The wire is calibrated *in situ* against a Pitot tube placed at the centerline of the pipe. Data are acquired with a 16-bit Data Translation DT9836 card.  $t_s U_{CL}/R \leq 5000$  centerline eddy-turnovers are acquired for  $N_{pts} \leq 31$  wall normal locations for all Reynolds numbers investigated (where  $t_s$  is the sampling time). The sampling frequency is kept at  $f_s = 65\text{kHz}$ , ensuring that the non-dimensional sampling frequency is kept  $f_s^+ \geq 1/3$  as for Hutchins et al. 2009. The initial position of the wire cannot be directly estimated through the encoder due to the slight deflection of the probe when exposed to high speeds. For this reason, an interactive procedure is implemented by using the diagnostic plot by Alfredsson and Örlü 2010, where the local mean velocity is compared to the centerline one. The friction quantities are computed by acquiring the static pressure drop along

$Re_\tau$	$9.9 \times 10^3$	$2.2 \times 10^4$	$3.2 \times 10^4$	$3.5 \times 10^4$	$3.9 \times 10^4$	
$U_{CL}$	9.8	22.9	34.33	38.5	45.5	m/s
$U_b$	8.4	20	30.2	33.5	38.4	m/s
$u_\tau$	0.34	0.74	1.1	1.19	1.36	m/s
$dp/dx$	0.6	2.9	6.2	7.53	9.73	Pa/m
$l_*$	$4.55e-5$	$2.1e-5$	$1.42e-5$	$1.29e-5$	$1.38e-5$	m
$\tau$	0.13	0.65	1.4	1.7	2.2	Pa
$L^+$	11	22	33	38	44	
$N_{pts}$	31	34	37	34	34	
$\kappa$	0.39	0.39	0.39	0.39	0.39	
B	4.5	4.5	4.5	4.5	4.5	
$f_s$	65	65	65	65	65	kHz

Table 5.1: Acquisition and flow parameters for all Reynolds numbers tested.

the pipe via the Initium digital pressure scanner, at a sampling frequency of 5Hz. The centerline velocity is monitored through the Pitot probe, connected to an MKS Baratron differential pressure transducer, located 11R upstream the test section since it proved not to influence the measurements at the test location. The temperature is acquired with a PT 100 thermistor, fixed at the test section. Since measurements can take up to 10 hours, static pressure and centerline measurements are repeated during each test. Measurements were performed at 5 Reynolds numbers in the range  $9.9 \times 10^3$  to  $3.9 \times 10^4$ .

## 5.2. Filtering procedure

To evaluate the contribution of the scales to the broadband turbulence intensity, the full fluctuating velocity signal is decomposed into a its small-scale and large-scale part, using a spectral filter to divide the small scales from the large scales. The procedure implemented, and further discussed in the next sections, can be summarised by the following steps:

- Choice of the cut-off frequency to separate the small-scale from the large-scale contribution to the full-signal streamwise velocity variance. As it will be detailed later, the frequency is chosen as the minimum frequency where the collapse of the streamwise, one-dimensional energy spectra for different Reynolds numbers is seen to hold, at different wall-normal locations. For this reason, the scales are actually separated into Reynolds-dependent and Reynolds-independent, but for sake of simplicity, they will be called from here onwards large and small scales respectively. As it will be clear later in this section, the Reynolds-independency of the small scales does not hold for the entire high-frequency range, due to the spatial filtering effects on the small scales.

- Correction for spatial filtering effects. The small scales can be affected by insufficient spatial resolution as the Reynolds number increases.
- Scaling for the small- and large-scale structures. After the signal has been corrected for the spatial filtering issues, we want to see if for the small scales the Reynolds-independency still holds for the entire range of wall-normal locations, and if so, which trend it has.

The value of the cut-off frequency is chosen on the basis of the "law-of-the-wall" for the streamwise energy spectra, recently proposed by Ganapathisubramani in Ganapathisubramani 2018. The quest of a scaling law for the turbulent energy spectra has seen numerous suggestions and approaches put forward throughout the years, ranging from the dimensional analysis approach of Perry and Abell 1977, where the choice of the velocity and length scales was based on the attached eddy hypothesis, to model-free scaling relations for different regions of the turbulent energy spectra by Zúñiga Zamalloa et al. 2014. It is specifically thanks to the latter that it was proven the existence of a law-of-the-wall in the high-wavenumber region of energy spectra for pipes and channels. Ganapathisubramani 2018 reinterpreted the dimensional analysis carried out in the two works mentioned above, and instead of relying on the attached eddy hypothesis to determine the appropriate velocity and length scales, he postulates the presence of a law-of-the-wall for the small-scale velocity fluctuations, an analogous of the Prandtl's law of the mean flow:

$$\frac{u_s^2(y^+)}{u_\tau^2} = g_w(y^+) \quad (5.1)$$

where  $u_s^2$  is the small-scale variance of the streamwise velocity fluctuations in the high-frequency regime, following the law of the wall represented by  $g_w(y^+)$ . This results in a universal form, depending only on inner scales and independent on the outer ones. To nondimensionalise the turbulent energy  $k_x \Phi_{uu}(k_x, y)$  contained at a certain wavenumber  $k_x$  at a given wall-normal location  $y$ , the quantities needed are a velocity and two length scales for  $k_x$  and  $y$ . Following the Prandtl's law of the wall, the friction velocity  $u_\tau$  and the viscous length scale are chosen as relevant scales for the energy and for the wall-normal location  $y$ . The choice of the second length scale is what differentiate Ganapathisubramani 2018 from the previous studies, choosing the viscous length scale instead of the wall-normal distance  $y$  (as would result from the attached eddy hypothesis). The choice follows from the law-of-the-wall for the small-scale fluctuations, independent of the outer influence and affected only by the inner scales, as  $l_* = \nu/u_\tau$ . This makes the law of the wall, for the streamwise energy spectrum:

$$\frac{k_x \Phi_{uu}(k_x, y)}{u_\tau^2} = F(k_x^+, y^+) \quad (5.2)$$

Therefore, remembering that the integral over the entire wavenumber range of the power spectral density is equal to the turbulent energy of the streamwise velocity component:

$$\int_0^\infty \Phi_{uu} dk_x = u^2(y) \quad (5.3)$$

Recalling eq.(5.1), the universal function in the inner region  $g_w(y^+)$  will be represented by:

$$g_w(y^+) = \int_{M^+}^\infty F(k_x^+, y^+) d\ln(k_x^+) \quad (5.4)$$

is a universal function, across different Reynolds numbers, in the inner region. In particular, for a given  $y^+$  close enough to the wall, eq.(5.4) indicates a universal value of wavenumber  $M^+$ , independent of the wall-normal location.

In the present case, analogous to what presented in Ganapathisubramani 2018, the spectra and therefore the filtering procedure is carried out in the frequency domain instead of the wavenumber. The need to invoke the Taylor's hypothesis may lead to incorrect assumptions regarding the collapse of the spectra, since it is based on the local mean velocity. In this case, the appropriate quantities to nondimensionalise the energy, the wall-normal location and the frequency are still the friction velocity and the viscous length scale for the first two, while the inner-scaled time ( $T = \nu/u_\tau$ ) is the relevant scale for frequency. The universal function  $g_w(y^+)$  is now found by seeking the collapse in the streamwise energy spectra across a range of Reynolds numbers such that:

$$g_w(y^+) = \int_{A^+}^\infty F(f^+, y^+) d\ln(f^+) \quad (5.5)$$

such that it is universal in the inner region and  $A^+$  is equivalent to  $M^+$ . In particular,  $A^+$  is the inner-scaled frequency that will be chosen as cut-off to separate the small- and large-scale contributions to the full-signal inner-scaled variance.

Therefore, we start by comparing the spectra at similar wall-normal locations in Fig.5.1 over a range of Reynolds numbers, against the inner-normalised frequency. The furthest location is chosen to be close to the outer-edge of the logarithmic region for the lowest Reynolds number. Assuming the bounds of the logarithmic region to be  $3\sqrt{Re_\tau} < y^+ < 0.15Re_\tau$  as in Marusic et al. 2013, for the lowest Reynolds  $300 < y^+ < 1483$ .

Despite guaranteeing one of the highest accuracies experimentally available, the data are still slightly affected by spatial filtering. For  $Re_\tau = 3.2 \times 10^4$  and  $Re_\tau = 3.8 \times 10^4$ ,  $L^+ = 35$  and  $L^+ = 44$  respectively. The effects of poor spatial resolution on the pre-multiplied power spectral densities have been thoroughly investigated by Fiorini in Fiorini 2017 and shown in Fig.5.2. The peak

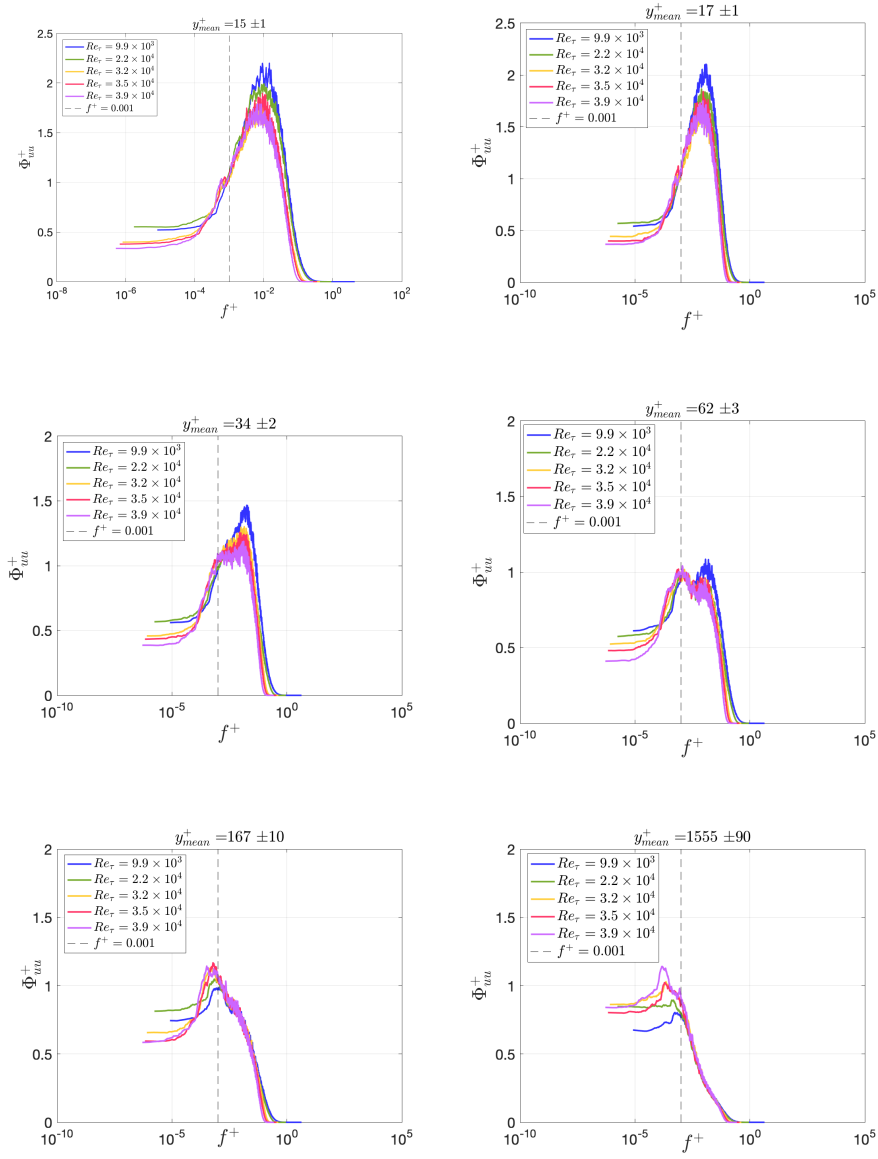


Figure 5.1: 1-dimensional spectra at different wall normal locations for the 5  $Re_\tau$  investigated. Dashed vertical line is the cut-off frequency later chosen for separating large scales from small scales.

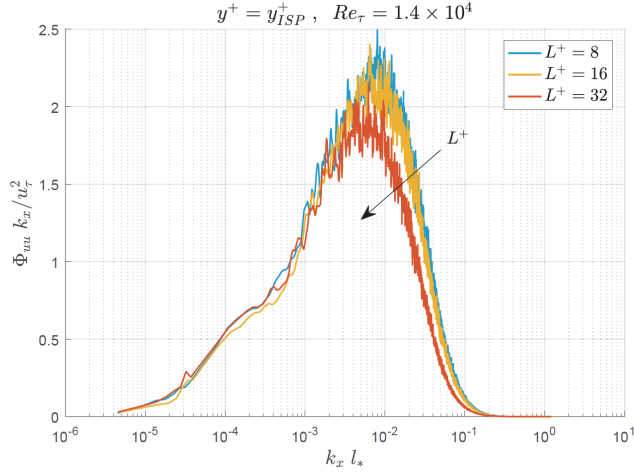


Figure 5.2: Pre-multiplied inner-scaled power spectral density at the wall normal location of the spectrum inner-peak, at  $Re_\tau = 1.4 \times 10^4$ , for different sensor lengths. Figure 5.12 taken from Fiorini 2017

attenuation with  $L^+$  is clear at the high wavenumbers while the curve collapse at the lowest wavenumbers which corresponds to the large-scale regime that is not affected by spatial resolution. This produces an artificial shift of the spectra peak at lower wavenumbers, compatible with the Reynolds number trend observed in the streamwise spectra shown in Fig.5.1. For these reasons, to set the cut-off frequency, the collapse is not sought in the entire high-frequency, but in an intermediate one, where frequencies are still high enough, but not to the extent to be greatly affected by spatial resolution issues. Based on these assumptions,  $A^+ = f^+ = 0.001$  is chosen as threshold.

### 5.3. Correction scheme

Before separating the small- and large-scale contributions to the broadband turbulence intensity, the semi-empirical correction scheme proposed by Smits et al. 2011 is applied to the inner-normalised variance of the full signal  $u^{2+}$ . This method is based on eddy-scaling: using the attached eddy hypothesis it predicts the energy attenuation due to spatial filtering effects across the entire boundary layer. Differently from the majority of other correcting schemes (P. Ligrani and Bradshaw 1987, P. Monkewitz, Duncan, and Nagib 2010), it shows accurate results for a wide variety of Reynolds numbers and wire lengths, most probably for its peculiar feature of using the distance from the wall for scaling, contrary to the viscous length scale as many other do.

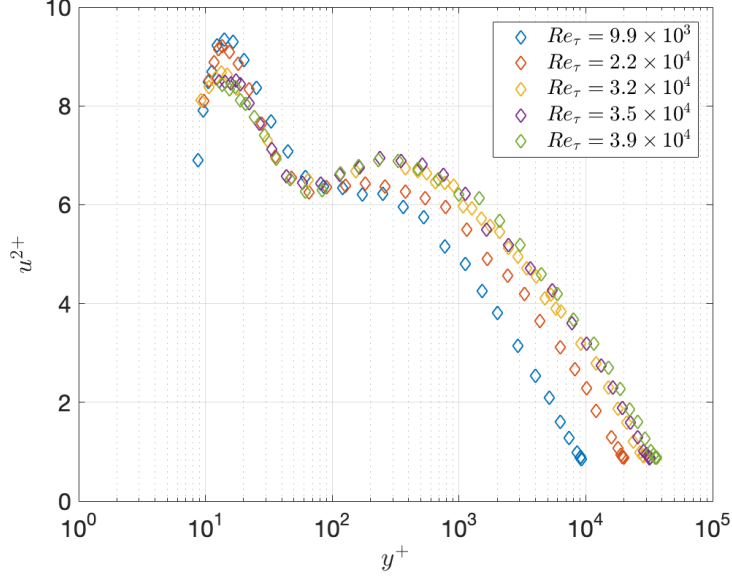


Figure 5.3: Inner-scaled streamwise velocity variance without any correction applied.

The inner-scaled streamwise variance  $u^{2+} = \overline{u^2}/u_\tau^2$  is shown in Fig.5.3 for all the Reynolds numbers acquired, presented without applying any correction-scheme. In agreement with measurements by Fiorini 2017 and Willert et al. 2017 (using hot-wires and PIV in the same facility, respectively) and measurements in the Princeton SuperPipe by Hultmark et al. 2013, the uncorrected profiles show both an inner and outer peak in the variance for  $Re_\tau > 3 \times 10^4$ .

It is possible now to correct the streamwise Reynolds stress found using a finite length wire (measured value) to the value it would have if acquired with an infinitesimally small sensor (true or corrected value). The corrected value is found by multiplying the the measured value  $u_m^{2+}$  with a function of the length of the wire in viscous units  $L^+$ , the inner-scaled wall-distance  $y^+$  and the value of the inner-scaled variance measured at the inner-peak location  $y^+ = 15$ :

$$u^{2+} = u_m^{2+} [f(y^+)M(L^+, u_m^{2+}|_{y^+=15}) + 1] \quad (5.6)$$

where  $M$  is seen to be constant for all wall distances, therefore it needs to be defined at only one location, which is usually the inner-peak one ( $y^+ = 15$ ):

$$M(L^+, u_m^{2+}|_{y^+=15}) = \frac{A \tanh(\alpha L^+) \tanh(\beta L^+ - E)}{u_m^{2+}|_{y^+=15}}. \quad (5.7)$$

with the fitting parameters (with no particular physical meaning) being  $\alpha = 5.6 \times 10^{-2}$ ,  $\beta = 8.6 \times 10^{-3}$ ,  $A = 6.13$  and  $E = -1.26 \times 10^{-2}$ . In many cases, especially at high Reynolds numbers, it can be rather challenging to measure at  $y^+ = 15$ . In that case, the alternative formulation of  $M$  through a regression fit can be used:

$$M(L^+) = 0.0091L^+ - 0.069 \quad (5.8)$$

with a note of caution, since it hides the implication that a wire of  $L^+ \leq 8$  could fully resolve the flow, while in practice  $L^+ \leq 4$  is more likely. Then, the term  $f(y^+)$  is defined as:

$$f(y^+) = \frac{15 \ln(2)}{y^+ + \ln(e^{15-y^+} + 1)} \quad (5.9)$$

The data resulting from the application of this correction scheme are presented in Fig.5.4.

As already noticed by Fiorini 2017 the variance shows an evident increase of the inner-peak for the highest Reynolds numbers, after the energy attenuation due to the insufficient spatial resolution is solved with the correction scheme. The corrected inner-peak values are compared in Fig.5.5 to the results for the turbulent boundary layer by Vallikivi, Ganapathisubramani, and Smits 2015, and other pipe-flow experiments from Superpipe, by Hultmark et al. 2012, and from CICLoPE itself by Willert et al. 2017 using PIV, where data are not affected by insufficient spatial resolution.

The difference between the corrected and uncorrected data is computed in the form:

$$\Delta u^{2+} = u_c^{2+} - u_m^{2+} \quad (5.10)$$

where  $u_c^{2+}$  is the corrected streamwise variance and  $u_m^{2+}$  is the measured one. Based on the assumption that only the small scales are affected by poor spatial resolution, they should be the only involved in the correction process. Therefore, the corrected small-scale variance is found:

$$u_s^{2+} = \Delta u^{2+} + u_{s,m}^{2+} \quad (5.11)$$

where  $u_{s,m}^{2+}$  is the not-corrected small-scale contribution to the broadband turbulence intensity.

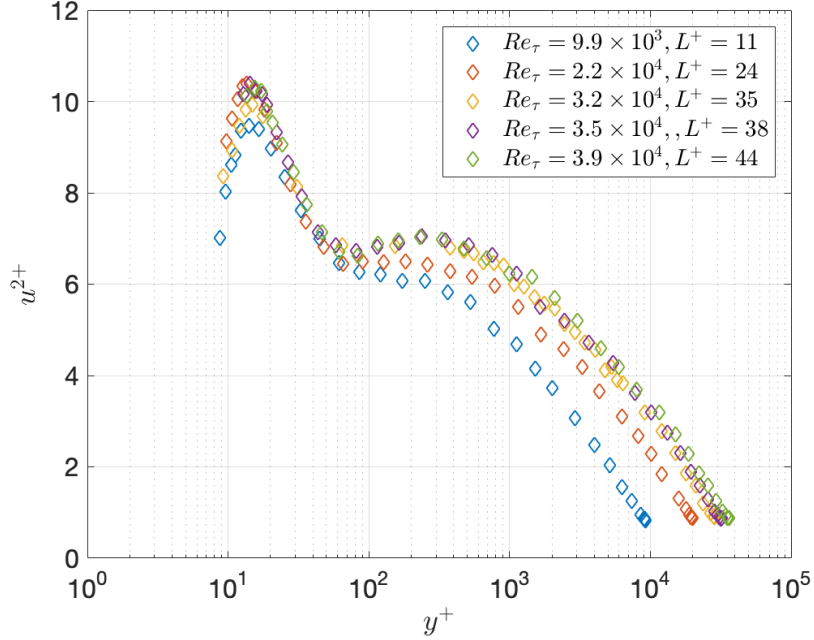


Figure 5.4: Inner-scaled streamwise velocity variance. Data are corrected using the correction proposed in Smits et al. (2011b)

#### 5.4. Data validation

The quality of the data is assessed on the basis of the data from previous experiments from the same facility for a similar range of Reynolds numbers. Single-wire and X-wire hot-wire measurements (with a sensing length of 1mm and a diameter of  $2.5\mu\text{m}$  and  $5\mu\text{m}$  respectively) were performed by Fiorini 2017 and Örlü et al. 2017 from the wall up to  $y \approx 0.3R$ . The inner-scaled mean velocity profiles for the five cases investigated are provided in Fig.5.7. In the logarithmic region the data are fitted using the values of  $\kappa = 0.39$  and  $B=4.5$  suggested by Fiorini 2017 and Örlü et al. 2017 for the same facility. The value agrees well with  $\kappa = 0.39 \pm 0.02$  found by Marusic et al. 2013 using a database of high-Reynolds-numbers wall-bounded turbulent flows experiments. Another logarithmic trend is confirmed by Örlü et al. 2017 and Fiorini 2017 for the streamwise velocity variance in the log-region, converging for different Reynolds numbers and exhibiting a universal slope following:  $\overline{u^2}^+ = C - A \ln(y/R)$ , with  $A = 1.26$  (Townsend-Perry constant) and  $C = 1.81$ . The quality of this fit is assessed in Fig.5.6 where data are plotted in compensated form.

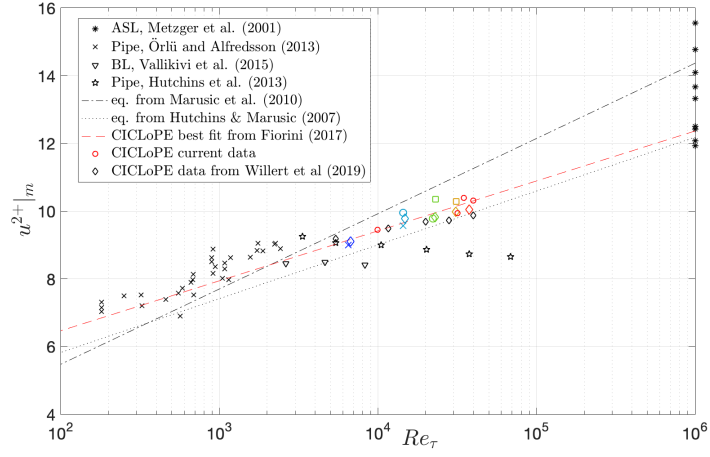


Figure 5.5: Inner peak of the viscous-scaled streamwise velocity variance. Coloured symbols represent data corrected for spatial resolution, while grey symbols are uncorrected data.

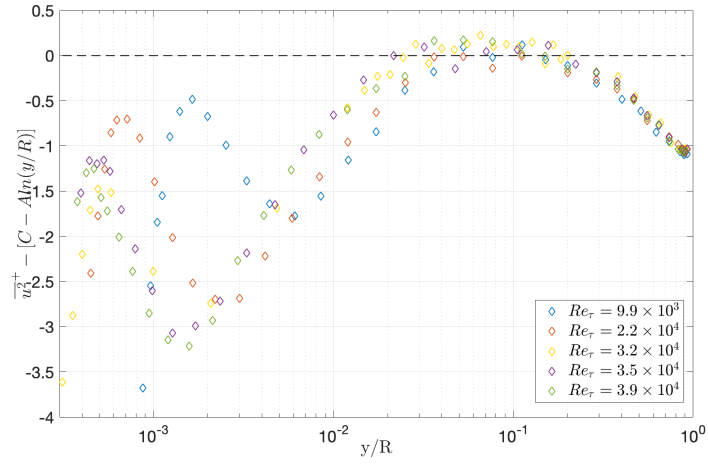


Figure 5.6: Log-law fits to the streamwise variance in wall-units. Curves are shown compensated for by the log-law with the Townsend-Perry constant  $A=1.26$  and  $C=1.81$ , taken from Fiorini 2017.

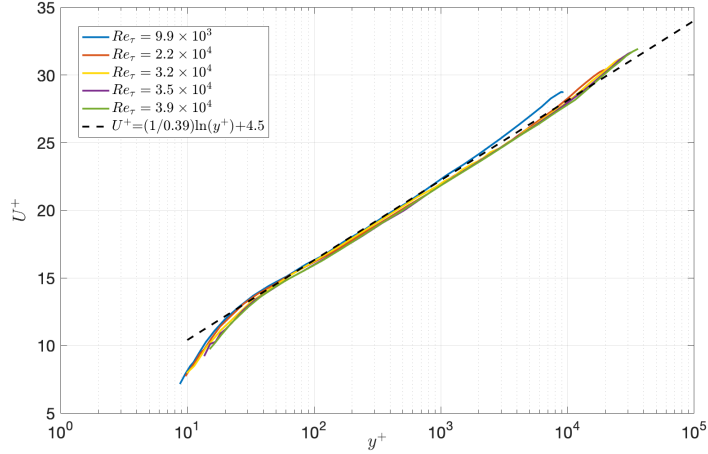


Figure 5.7: Mean streamwise velocity profile in viscous units for the five cases investigated. The straight dashed line is the logarithmic law implemented.

The quality of the log-law fit is verified through plots of the data compensated for by the expected log-law fits as shown in Fig.5.8. Good agreement is noticed throughout the entire  $y^+$  range of the log-region.

The correction scheme described in the previous section is applied to the data and the results, plotted in inner-scaling, for the 5 Reynolds numbers are shown in Fig.5.9. The data are seen to agree well for the entire range of  $Re_\tau$ , except for an anomalous behaviour at  $Re_\tau = 2.2 \times 10^4$ , where the variance is suspiciously higher than the reference data set by Fiorini 2017. For this reason, the analysis is carried on discarding this set of measurements.

### 5.5. Small-scale variance

The small-scale contributions are presented in Fig.5.10 and Fig.5.11. They are separated from the large scales using a spectral cut-off filter, with an inner-scaled cut-off frequency of  $f^+ = 0.001$ . The correction is computed in two steps: first, the Smits et al. 2011 scheme is applied to the full signal, obtaining the difference between the corrected and uncorrected signal,  $\Delta u^+$ . Secondly it is assumed that only the small scales are affected by spatial filtering, therefore the  $\Delta u^+$  is applied only to the small-scale contribution, as detailed in the section above. The data are presented in the uncorrected and corrected form respectively for the retained  $Re_\tau$  after the data validation.

The small-scale fluctuations are seen to collapse for nearly the entire range of wall-normal locations, up to  $y^+ \approx 6000$ , well past the logarithmic region

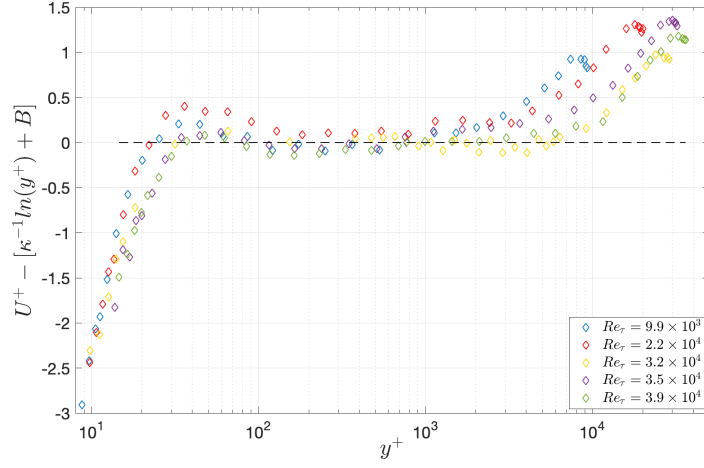


Figure 5.8: Log-law fit to the streamwise mean velocity in wall units. Curves are compensated for by the expected log-law using  $\kappa = 0.39$  and  $B=4.5$ , taken from Fiorini 2017.

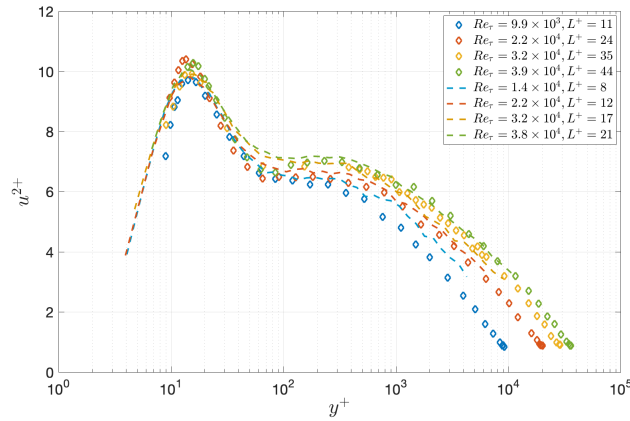


Figure 5.9: Inner-scaled streamwise velocity variance from CICLoPE, dashed lines are measurements from Fiorini (2017), while diamond symbols is data from current measurements. Both data sets are corrected using the same correction scheme proposed by Smits et al (2011b).

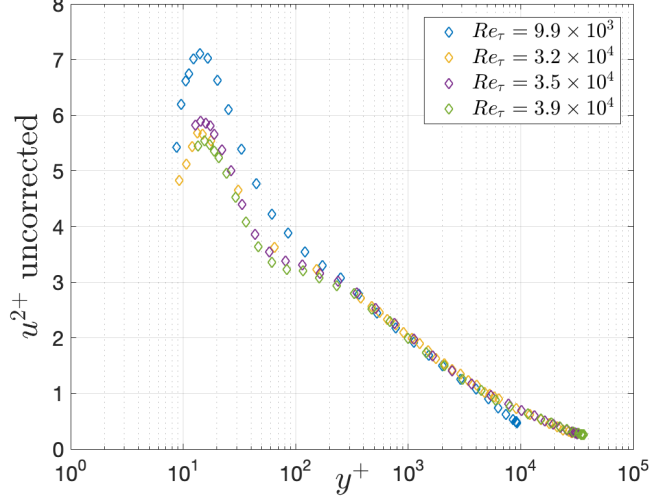


Figure 5.10: Inner-scale streamwise velocity variance for the small scales only. Data are shown without any correction applied.

for the lowest  $Re_\tau$ , which is located at around  $y^+ \approx 1500$ . As a conservative estimation of the bounds of the log-region of the mean flow, it was followed Marusic, Baars, and Hutchins 2017 suggesting:  $\sqrt{Re_\tau} < y^+ < 0.15Re_\tau$ . In particular, over a range of Reynolds numbers, the small-scale variance appears to follow a logarithmic decay with the inner-scaled distance from the wall for  $y^+ > 500$ . This logarithmic trend extends beyond the traditional logarithmic region for the mean profile and has the form:

$$\frac{u_s^2(y^+)}{u_\tau^2} = -\alpha \ln(y^+) + \beta = -0.67 \ln(y^+) + 6.65; \quad (5.12)$$

Where  $\alpha = -0.67 \pm 0.009$  and  $\beta = 6.62 \pm 0.07$  (where uncertainties are computed as the 95% confidence intervals of the linear regression). The logarithmic trend is further confirmed when the small-scale variance is plotted in the compensated form in Fig.5.12. Here, the logarithmic fit of eq.(5.12) is subtracted from the experimental data, similarly to an indicator function where the gradient are plotted. The data show a residual close to zero for a wide range of  $y^+$  locations, compatible with the existence of a universal law-of-the-wall for the small-scale turbulence intensity of a pipe flow, in the form of eq.(5.12). The physical implications of the value of the two constants, the slope of -0.66 and the intercept at 6.62, still needs to be further investigated. Their magnitude could be dependent on the geometry of the flow considered, since

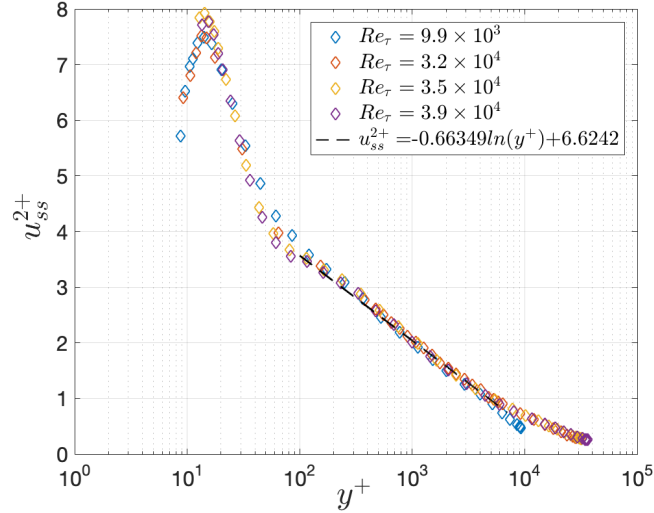


Figure 5.11: Inner-scaled streamwise velocity variance for the small scales only. Data are corrected with the procedure described in the previous section, 5.3. Dashed black line shows the logarithmic decay of the small-scale variance from  $y^+ = 600$ .

despite sharing the same logarithmic decay, the constants differ from the ones found for turbulent boundary layers ( $\alpha = -0.15 \pm 0.002$  and  $\beta = 1.59 \pm 0.01$  Ganapathisubramani 2018), suggesting a geometry dependence of the law of the wall for the small-scale turbulence intensity. On the other hand, their value is expected to depend on the cut-off frequency  $f^+$ , setting the amount of energy retained after the filtering process. Fig.5.13 shows the logarithmic decay for  $f^+ = 0.05$ ,  $f^+ = 0.01$  and  $f^+ = 0.005$  for the turbulent boundary layer. Both the values of  $\alpha$  and  $\beta$  are seen to decrease in absolute value as the cut-off frequency increases, tending to a behaviour similar to the turbulent boundary layer. Physically it means that as the cut-off frequency increases, less energy is retained for the small-scales, but it decreases more slowly moving away from the wall.

## 5.6. Large-scale variance

The inner-scaled variance contribution from the large-scale only is shown in Fig.5.14. As expected, the large scales' contribution increases with the Reynolds number for the entire range of wall-distances, differently to the small-scales'. In Fig.5.15 the value of the contributions at the inner-peak location  $y^+ = 15$  of the small and large scales are compared to the behaviour of the full

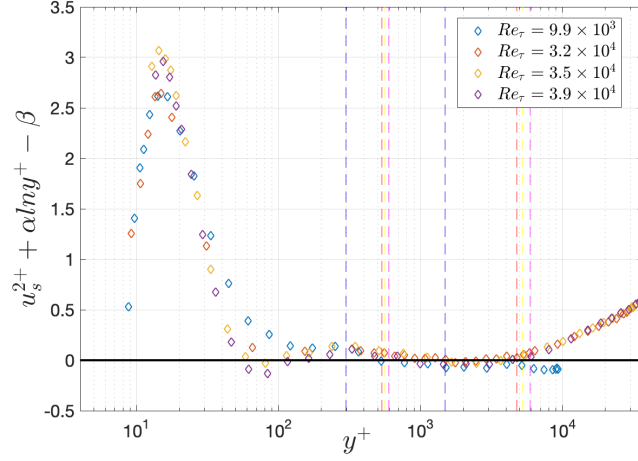


Figure 5.12: Compensated form of small-scale streamwise velocity variance. The logarithmic fit is subtracted from the experimental data (diamonds). Dashed coloured lines are the bounds of the logarithmic region of the mean flow ( $3\sqrt{Re_\tau} < y^+ < 0.15Re_\tau$ ), for matching colours.

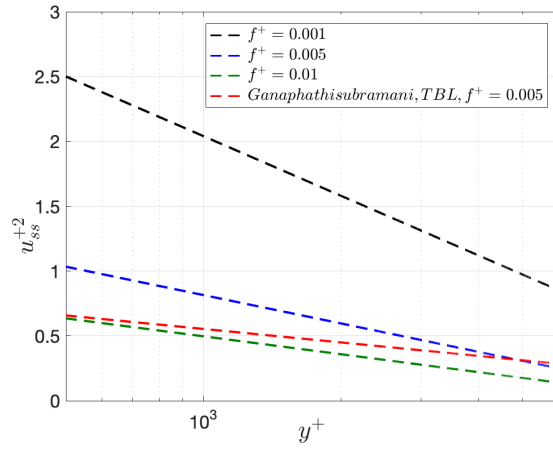


Figure 5.13: Logarithmic decay of the inner-scaled small scale variance, for cut off frequencies of  $f^+ = 0.001$ ,  $f^+ = 0.005$ ,  $f^+ = 0.01$  and  $f^+ = 0.005$  for the turbulent boundary layer.

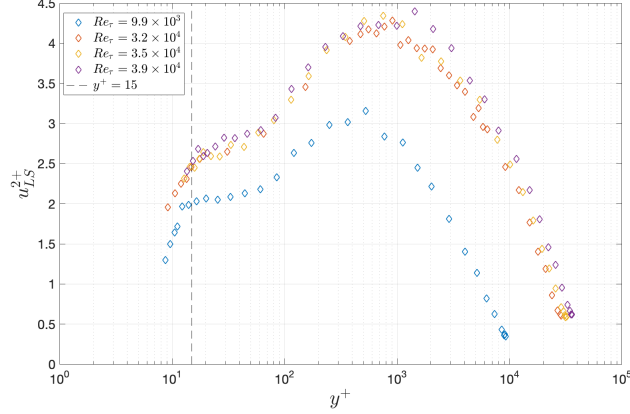


Figure 5.14: Inner-scaled streamwise velocity variance for the large scales only. Dashed line is positioned at  $y^+ = 15$ , where the maximum of the inner-scaled streamwise velocity variance is usually located.

signal. The increase of the peak of the inner-scaled variance of the full signal  $u^{+2}|_m$ , described by the linear fit:

$$u^{+2}|_m = 0.54 \ln(Re_\tau) + 4.49 \quad (5.13)$$

seems to be linked with an increase of the contributions of the large scales, described by

$$u_{LS}^{+2}|_m = 0.39 \ln(Re_\tau) - 1.24 \quad (5.14)$$

with an increase of around 25% between the lowest and highest Reynolds' peak, in contrast to the a rise of nearly 3% for the small-scales' peak, which can be considered therefore constant with the Reynolds.

To relate the behaviour of the large scales in the near-wall region to the outer region, we can use as parameter the ratio between their value at  $y^+ = 15$  and the outer peak,  $u_{LS}^{+2}|_{IP}/u_{LS}^{+2}|_{OP}$ . Given the scatter of the data, the outer peak is taken as the maximum value of the 2<sup>nd</sup> order polynomial fit of the nearby region. Fig.5.16 shows that this ratio can be considered constant with the Reynolds number.

In particular, the value of the ratio around 0.5 means that the outer peaks increases at around double the rate as the inner peak, both keeping the same rate as the Reynolds number grows. The outer-peak trend with the Reynolds number is in fact described by the linear fit:

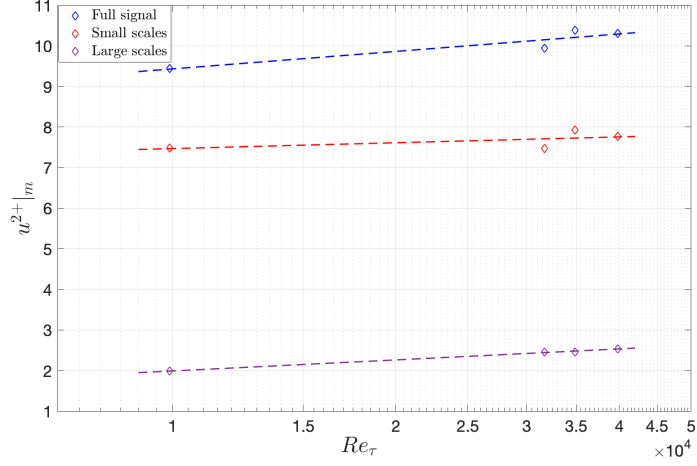


Figure 5.15: Near-wall maxima of the inner-scaled streamwise velocity variance. The contributions from the small scales and large scales are separated. Dashed lines are the least-square fit.

$$u^{+2}|_{m,op} = 0.9 \ln(Re_\tau) - 5.45 \quad (5.15)$$

To conclude, the Reynolds-independency of the small-scale streamwise velocity variance is observed after the correction scheme is applied, and it is seen to hold for the entire range of wall-normal locations investigated, showing a logarithmic decay. On the other hand, the large scales, with their Reynolds dependency, are seen to be the responsible for the increase of the inner peak of the inner-scaled streamwise velocity variance.

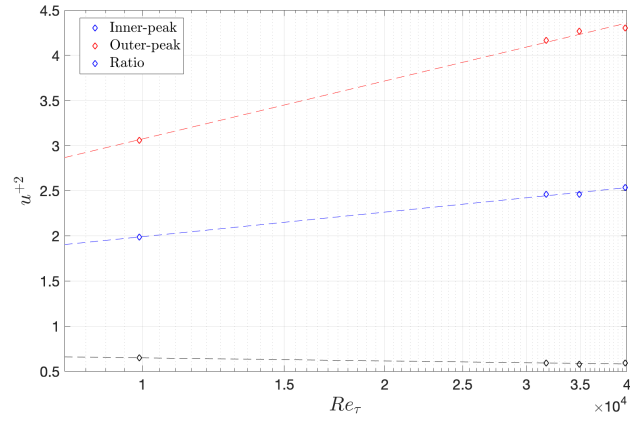


Figure 5.16: Inner-scaled inner and outer peak of the streamwise variance for the large-scale contributions. The black symbols show the ratio  $u_{LS}^{2+}|_{IP}/u_{LS}^{2+}|_{OP}$ . Dashed lines are the linear fits.

## Linear Coherence Spectra analysis

Wall-bounded turbulence is known to be organised in large- and very-large-scale motions. The most accepted theory describing their internal architecture is the pioneering work of Townsend (Townsend 1976). His attached eddies hypothesis suggests a hierarchical organisation of the self-similar vortices in the wall-normal direction, attached to the wall and developing in the streamwise direction for numerous lifetimes. In order to investigate the wall-attached, the self-similar and inner dynamics, two-point hot-wire measurements are performed in CICLoPE at two Reynolds numbers,  $Re_\tau = 1.2 \times 10^4$  and  $Re_\tau = 3.2 \times 10^4$ . The resulting coherence spectra will reveal the presence of self-similar wall-attached structures, and how their behaviour evolves with the Reynolds number.

### 6.1. Experimental set-up

To investigate the nature of the small and large-scale structures and how their coherence varies with the distance from the wall, two-point measurements are performed at the test section of the Long Pipe, at  $x/D \approx 123$ . One single-wire with a sensing length of 0.5mm and a diameter of  $2.5 \mu m$ , is fixed on the "global" traverse (see chapter 3) at a distance from the lower wall of the test section  $y = 0.2R$  which corresponds to the outer edge of the logarithmic region. The other one, with the same characteristics and mounted on the "small traverse" (see chapter 2), spans the region comprised between the wall and the fixed probe. The initial position of the moving probe is retrieved using the diagnostic plot following the method described in chapter 5. Both probes were simultaneously calibrated *in situ*, symmetrically placed at  $y=0.02m$  from the centerline, where  $U = U_{CL}$ . Data are acquired with the National Instrument NI-9215 Analog Input Module, installed on the cRIO 9068 chassis system. Two Reynolds numbers are tested:  $Re_\tau = 1.2 \times 10^4$  and  $Re_\tau = 3 \times 10^4$ . As in the experiment described in the previous chapter 5, the sampling frequency is set at  $f_s = 65kHz$ . Friction quantities are estimated by acquiring the static pressure from the wall taps along the pipe using the Initium digital pressure scanner described in 3. The temperature of the flow is acquired with a PT 100 thermistor to correct the hot-wire output voltage and compute the density. The centerline velocity is acquired with a Pitot probe mounted at  $y = 11D$ , since tests confirmed not to influence the measurements at the test section, connected

$Re_\tau$	$U_{CL}[\text{m/s}]$	$u_\tau[\text{m/s}]$	$dp/dx[\text{Pa/m}]$	$l_*[\mu\text{m}]$	$N_{pts}$
$1.2 \times 10^4$	11.4 [m/s]	0.41	0.87	$3.77e - 5$	22
$3 \times 10^4$	33.5[m/s]	1.03[m/s]	5.5	$1.47e - 5$	32

Table 6.1: Acquisition and flow parameters for the two Reynolds numbers tested.

d [ $\mu\text{m}$ ]	L [mm]	$L^+$	OHR	$f_s[\text{kHz}]$
2.5	0.5	13	0.8	65
2.5	0.5	34	0.8	65

Table 6.2: Wire and acquisition parameters for the two Reynolds numbers tested.

to the differential pressure transducer MKS Baratron 120AD ( $f_s = 5\text{Hz}$  for one minute). The friction quantities used for inner-scaling are computed acquiring the static pressure along the pipe using the Initium digital pressure scanner, at a sampling frequency of  $5\text{Hz}$  for a period of one minute. Since measurements can last for more than two hours, static pressure acquisitions are repeated throughout the tests. Run and flow parameters are listed in table 6.1 above.

## 6.2. Linear coherence spectrum

To investigate the scale-dependent (linear) coupling between the velocity signal in the log-region  $u(y_{ref}, t)$  and the fluctuations in the inner region  $u(y, t)$  of the pipe flow, the linear coherence spectrum (LCS)  $\gamma_L^2$  is used as a parameter:

$$\gamma_L^2 = \frac{\left| \langle \tilde{U}(y; \lambda_x) \tilde{U}^*(y_{ref}; \lambda_x) \rangle \right|^2}{\left| \langle \tilde{U}(y; \lambda_x) \rangle \right|^2 \left| \langle \tilde{U}(y_{ref}; \lambda_x) \rangle \right|^2} = \frac{\left| \Phi'_{uu}(y, y_{ref}; \lambda_x) \right|}{\Phi_{uu}(y; \lambda_x) \Phi_{uu}(y_{ref}; \lambda_x)}. \quad (6.1)$$

Where  $\tilde{U}(y; \lambda_x) = \mathcal{F} |u(y)|$  is the Fourier transform of  $u(y)$ , the asterisk  $*$  indicates the complex conjugate,  $\langle \rangle$  denotes ensemble averaging and  $||$  refers to the modulus. In the case of the second right-hand-side of eq.(6.1),  $\Phi'_{uu}$  denotes the cross-spectrum, while the denominator comprises the two energy spectra for the reference signal:  $\Phi_{uu}(y_{ref}, \lambda_x)$  and the one at  $y$  distance from the wall  $\Phi_{uu}(y, \lambda_x)$ . In order to obtain a physical interpretation of the scales using temporal data, the frequencies are transformed into wavelength  $\lambda_x = U_m/f$  invoking Taylor's hypothesis, where local mean velocity is taken as the convection velocity. By definition,  $0 \leq \gamma_L^2 \leq 1$  (where 0 is absence of coherence and 1

is perfect coherence) and it can be physically interpreted as the fraction of common variance shared by the fluctuations measured at the fixed location  $u(y_{ref})$  and the one in the inner region  $u(y)$ . Equivalently, as pointed out by Baars, Hutchins, and Marusic 2017, as the square of the correlation coefficient between two specific scales. In eq.(6.1) only the magnitude of the cross-spectrum is comprised, making it impossible to infer a consistent stochastic phase shift between the reference signal  $u(y_{ref})$  and  $u(y)$  from the value of  $\gamma_L^2$ . The information about the phase of a specific scale is, in fact, embedded in the phase of the cross-spectrum  $\Phi'_{uu}$ . Nonetheless, the linear coherence spectrum can indirectly measure the phase consistency across ensembles of pairs of  $u(y_{ref})$  and  $u(y)$ : if each pair used to compute the cross-spectrum contains a random phase shift for a given scale, that specific scale is not correlated and therefore  $\gamma_L^2$  is zero.

### 6.3. The influence of probe distance

To clarify the LCS, we consider an arbitrary pair  $u(y) - u(y_{ref})$  for a given Reynolds number. For instance, the signal at the reference position  $y_{ref}^+ \approx 5835$  ( $y_{ref} = 0.2R$ ) and a signal in the log region  $y^+ = 4000$ . The energy spectra and the LCS are shown in Fig.6.1 (black dashed line for the reference signal, and green line for the inner-region one) and Fig.6.2.

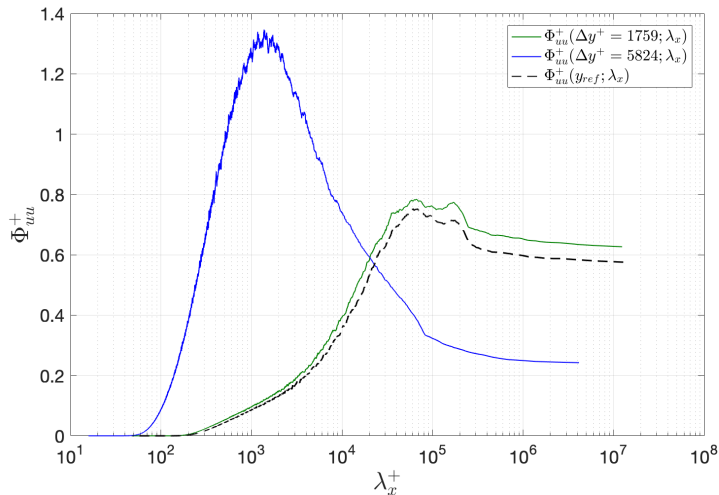


Figure 6.1: Premultiplied energy spectra as function of the inner-scaled wavelength. Dashed line is at reference position, solid lines are two different probe distances, for  $Re_\tau = 1.2 \times 10^4$

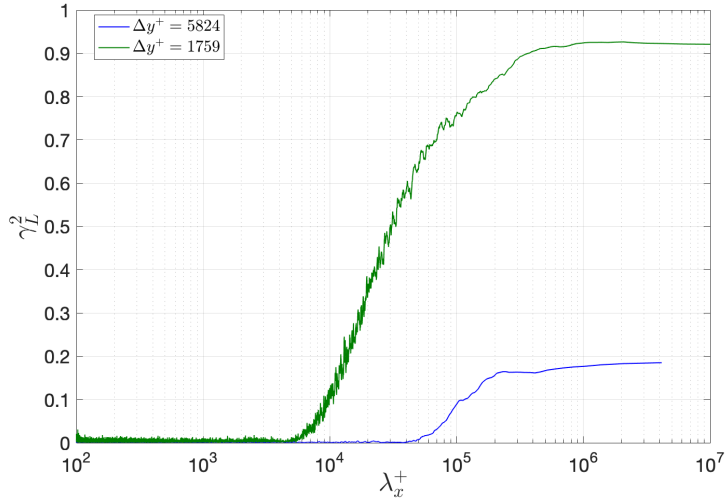


Figure 6.2: LCS as function of inner-scaled wavelength for two different probe distances, for  $Re_\tau = 1.2 \times 10^4$ .

Plotting the parameter reveals that, for this specific probe distance  $y^+ - y_{ref}^+$ , the largest scales are correlated to a degree of around 0.9, while it sensibly drops below 0.1 when  $\lambda_x^+ \leq 10^4$ . The effect of probe separation is investigated by combining the signal at  $y_{ref}$  with a signal in the inner-region (represented with the blue lines in Fig.6.1 and Fig.6.2). This trend of increasing coherence with increasing wavelength is already anticipated by Baars, Hutchins, and Marusic 2017, who justified it for any two-point measurements separated in space in a turbulent flow. Here, because of the smaller integral time scales of the smaller eddies, the correlation across a fixed distance between the two measuring points is lower. By increasing the distance between the probes (from  $\Delta y^+ \approx 1759$  in the first case, to  $\Delta y^+ \approx 5824$  in the second one), the correlation decreases noticeably at all scales, with the largest energetic scales still being more correlated than the small ones. By extending eq.(6.1) to the full range of wall-distances  $y$  explored (from beneath the inner-peak for both Reynolds numbers investigated, up to  $y/R < 0.2$ ), the LCS for each pair  $u(y) - u(y_{ref})$  is provided. In Fig.6.3 and Fig.6.4 the coherence spectrogram for the  $Re_\tau = 1.2 \times 10^4$  and  $Re_\tau = 3 \times 10^4$  are represented as a iso-contour map of  $\gamma_L^2(y, r_{ref}; \lambda_x)$  as a function of the inner-scaled wavelength  $\lambda_x^2$ . In both cases only the large-scale motions remain coherent with the near-wall region as the distance from the wall increases (in this case corresponding to decreasing distance between the probes).

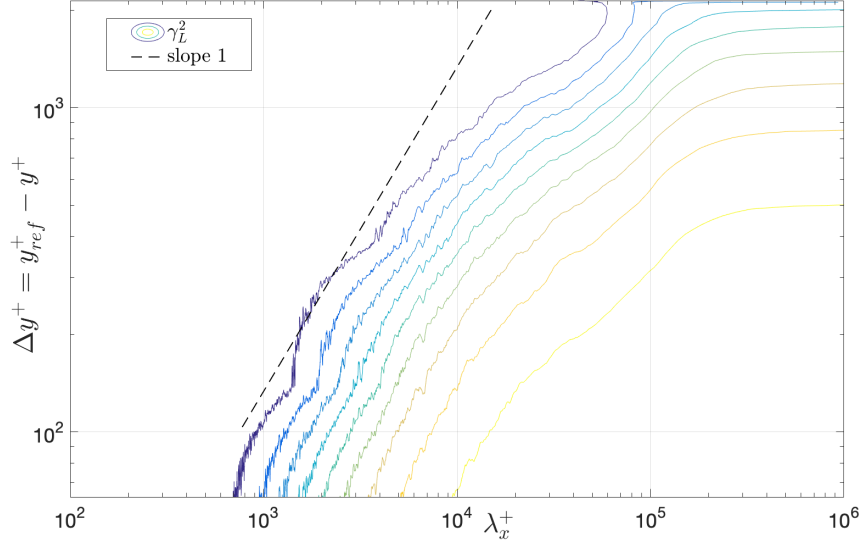


Figure 6.3: Coherence spectogram  $\gamma_L^2(y, y_{ref}; \lambda_x)$  relative to the reference location  $y_{ref} = 0.09R$ . Levels are 0.1:0.1:0.9, for  $Re_\tau = 1.2 \times 10^4$ .

In both Fig.6.3 and Fig.6.4 the dashed black line represents the line of unitary slope, reflecting the self-similar nature of the structures as suggested by Baars, Hutchins, and Marusic 2017 (where self-similar is intended in the geometrical sense). For both Reynolds numbers, the slope of the iso-contours does not agree perfectly with the line of slope 1, and this can be due to the different reference used in this experiment compared to Baars, Hutchins, and Marusic 2017. In his experimental work on turbulent boundary layers, the fixed probe is placed in the near-wall region while the moving one ranges from close to the wall to the outer region. Nonetheless, even in the present work it is possible to distinguish a region where the LCS iso-contours lines align with lines of constant  $\lambda_x^+$  or equivalently  $\lambda_x/\Delta y$ . In this area  $\gamma_L^2$  increases linearly with the wavelength. This is particularly clear when the parameter is plotted against the streamwise wavelength normalised with the distance between the two probes ( $\Delta y$ ) in Fig.6.5 and Fig.6.6 for both Reynolds.

For a fixed wall-distance  $y$ ,  $\gamma_L^2$  increases linearly with  $\log(\lambda_x)$  and decreases with  $\Delta y$  for a constant wavelength, reflecting the self-similar nature of the structures. The increase of  $\gamma_L^2$  is quantified by the following relation: (from Baars, Hutchins, and Marusic 2017):

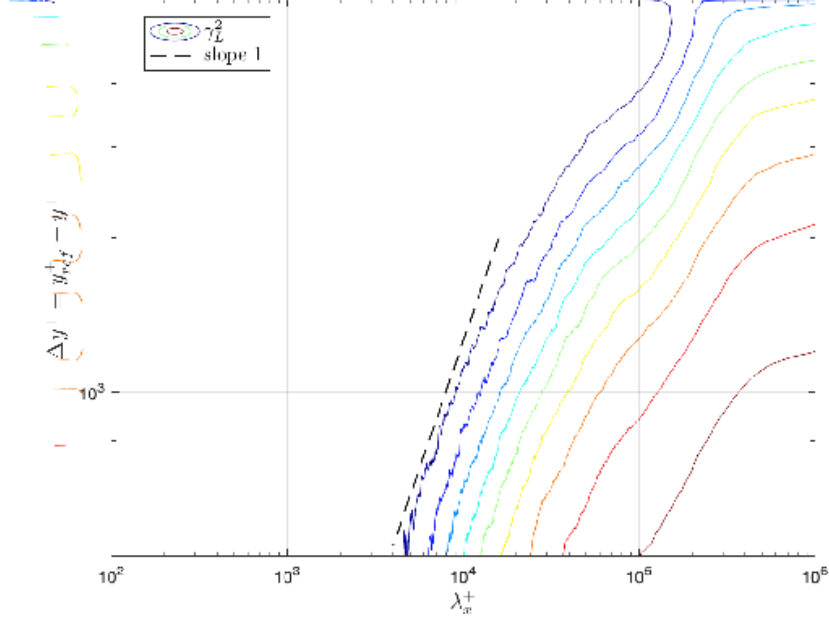


Figure 6.4: Coherence spectrogram  $\gamma_L^2(y, y_{ref}; \lambda_x)$  relative to the reference location  $y_{ref} = 0.09R$ . Levels are 0.1:0.1:0.9, for  $Re_\tau = 3 \times 10^4$ .

$$\gamma_L^2 = C_1 \ln\left(\frac{\lambda_x}{\Delta y}\right) + C_2 \quad (6.2)$$

, where  $\Delta y$  is the distance between the two probes. The relation describes the coherent structure in the area  $20 < \lambda_x/\Delta y < 100$  (visually inspected). As for the limits in terms of wall-distance, the behaviour is observed inside the logarithmic region for  $3Re_\tau^{1/2} < y^+ < 0.06Re_\tau$ . If the bounds are set as suggested by Marusic et al. 2013 at  $3Re_\tau^{1/2} < y^+ < 0.15Re_\tau$ , the area is slightly smaller than the one resulting in Baars, Hutchins, and Marusic 2017. This difference could be due to the different references taken in the two experiments (Baars, Hutchins, and Marusic 2017 and the current one) and the different geometry of the flow as well.

The representation of coherence spectrum for a specific combination of  $u(y_{ref})$  and  $u(y)$  in iso-contours is obtained by slicing the  $\gamma_L^2$  graph at the inner-region location  $y$ . In Fig. 6.7 and 6.8 the LCS for different wall-normal positions are represented for the two Reynolds numbers in normalised form.

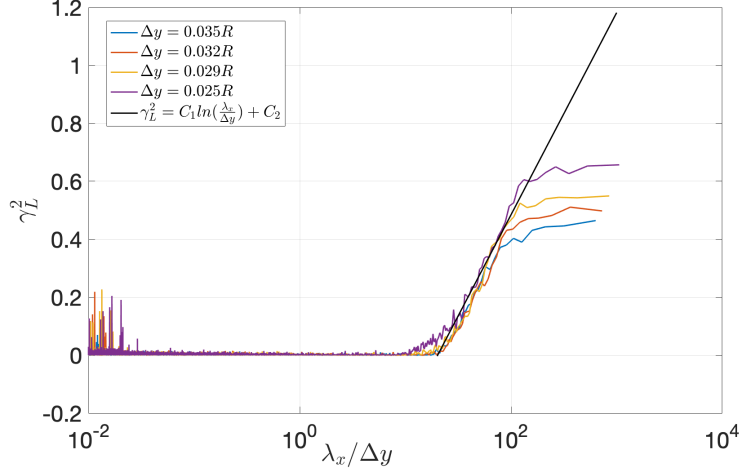


Figure 6.5: Linear coherence spectra  $\gamma_L^2(y, y_{ref}; \lambda_x^+)$  for  $Re_\tau = 1.2 \times 10^4$ . Black solid line represents the linear variation of  $\gamma_L^2$  with the  $\lambda_x/\Delta y$ .

Here,  $\gamma_L^2$  is normalised with the value at the plateau so to have each curve ranging from 0 to 1. For both Reynolds numbers the same pattern appears,  $\gamma_L^2$  peels off from zero at larger  $\lambda_x^+$  as the distance between the two probes decreases (moving the probe further and further away from the wall) until the probe enters the logarithmic layer. From here on, as the probe moves closer to the fixed one, the behaviour is inverted, with  $\gamma_L^2$  peels off from zero at decreasing  $\lambda_x^+$ . This is because as the probe distance increases, only the largest scales will remain coherent. As expected, as the probes move closer to each other, the coherence increases as the higher value of the plateau shows. The behaviour of  $\lambda_x^+$  with the probe-distance is represented in Fig.6.9, where the peel-off  $\lambda_x^+$  (taken as the value where  $\gamma_L^2$  is 20% of the plateau) is represented in function of  $\Delta y$ . Physically it means that from the logarithmic region, moving away from the wall, the correlation increases for smaller and smaller scales, despite remaining still way larger for the large scales. The peel-off  $\lambda_x^2$  decreases exponentially with the distance between the two probes (and inversely with the distance from the wall) following:

$$\lambda_x^2 = e^{\alpha \Delta y + \beta} \quad (6.3)$$

Considering the same range of probe-distances, if the constants of the fit  $\alpha$  and  $\beta$  nearly doubles as the Reynolds number increases ( $\alpha$  from  $\approx -43$  to  $-105$ ,  $\beta$  from  $\approx 18$  to  $\approx 31$ ), the exponential nature of the behaviour does not.

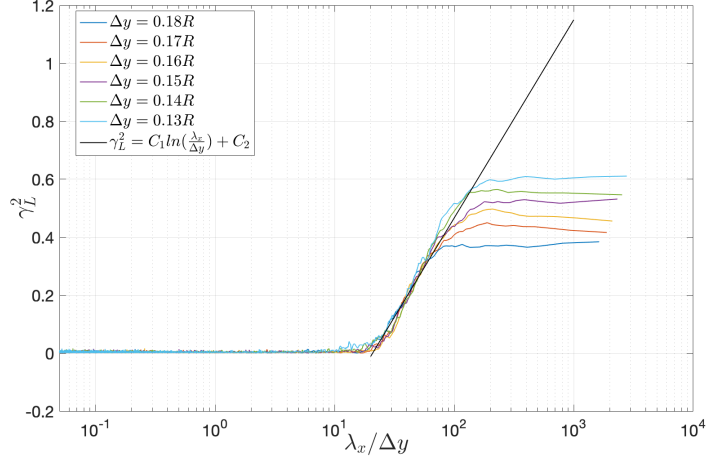


Figure 6.6: Linear coherence spectra  $\gamma_L^2(y, y_{ref}; \lambda_x^+)$  for  $Re_\tau = 3 \times 10^4$ . Black solid line represents the linear variation of  $\gamma_L^2$  with the  $\lambda_x / \Delta y$ .

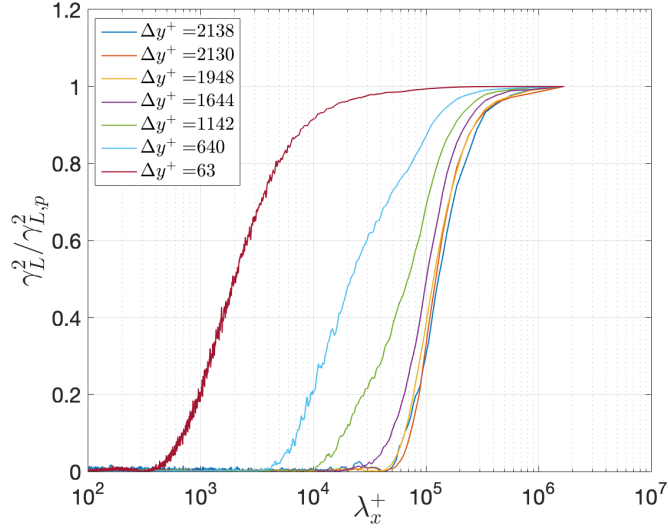


Figure 6.7:  $\gamma_L^2$  normalised with its value at its plateau for different probe-distances as function of inner-scaled wavelength,  $\lambda_x^+$ , for  $Re_\tau = 1.2 \times 10^4$ .

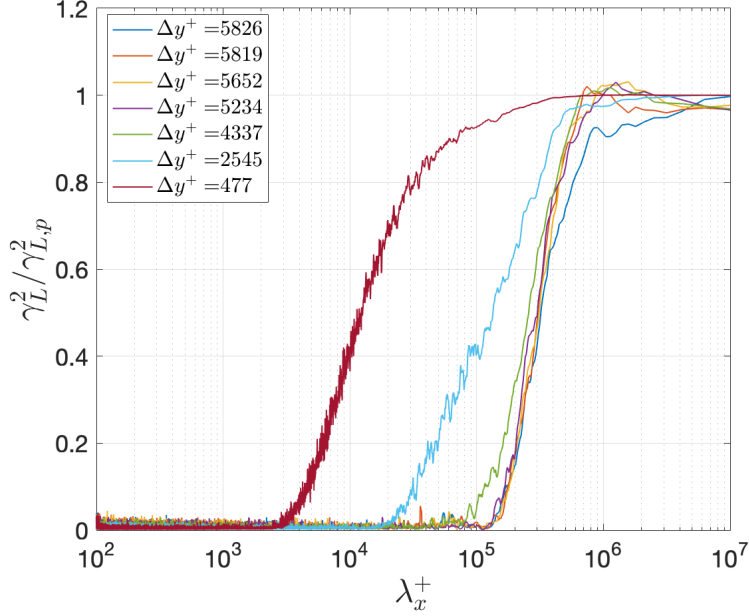


Figure 6.8:  $\gamma_L^2$  normalised with its value at its plateau for different probe-distances as function of inner-scaled wavelength,  $\lambda_x^+$ , for  $Re_\tau = 3 \times 10^4$ .

#### 6.4. Influence of Reynolds number

In order to see the effect of the Reynolds number on the linear-coupling of the scales, the LCS is compared in Fig.6.11. The comparison is in outer units ( $y/R$  and  $\lambda_x/\Delta y$ ) since for a fixed inner-scaled distance from the wall, increasing the Reynolds number has the same effect as decreasing the physical distance from the wall. This is confirmed by Fig.6.10 where the coherence at  $y^+ \approx 1500$  is shown: as the Reynolds decreases, the curve is shifted to the lower  $\lambda_x^+$  as when the probe is moved away from the wall. When outer-scaled the LCS is seen to collapse for the entire range of wall distances, with the only difference that at larger wavelengths, the highest Reynolds number shows the same coherence for location slightly further from the wall. The small discrepancies can be due to the smoothing of the data presented.

As for the influence of the Reynolds on the increase of  $\gamma_L^2$ , a linear-square fitting of eq.(6.2) to the data inside the domain leads to  $C_1 \approx 0.30$  and  $C_2 \approx -0.9$ , for both Reynolds numbers. As matter of facts, the profiles of  $\gamma_L^2$  taken inside the aforementioned boundaries, show a Reynolds number universality described by eq.(6.2) substituting the values of  $C_1$  and  $C_2$ . This suggests

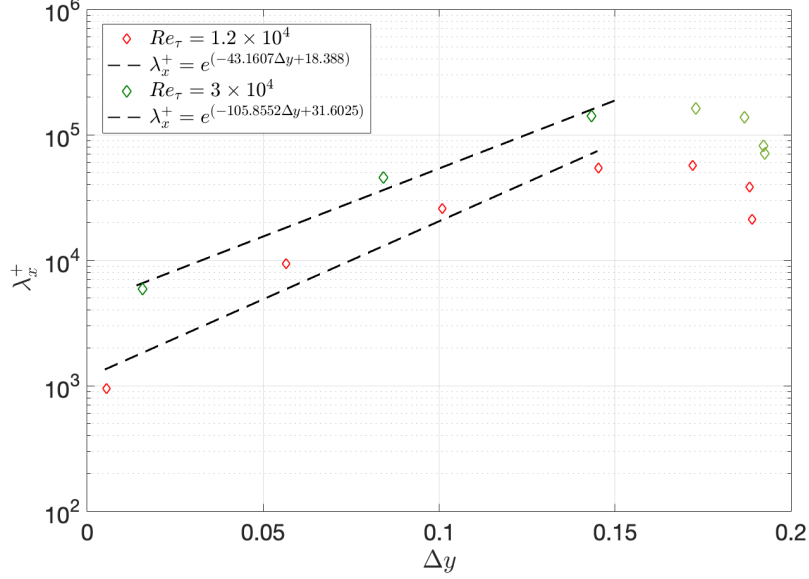


Figure 6.9: Peel-off zero  $\lambda_x^+$  as function of probe distance, for the two Reynolds numbers investigated. Dashed lines are the linear fit.

that, as for the turbulent boundary layer, also the coherent wall-attached structures are self-similar, consistent with the attached eddy hypothesis theorised by Townsend 1976. It is now possible to introduce the streamwise/wall-normal aspect-ratio of the self-similar eddy, defined by Baars, Hutchins, and Marusic 2017 as:

$$AR \equiv \frac{\lambda_x}{\Delta y} \Big|_{\gamma_L^2=0} = \exp\left(\frac{-C_2}{C_1}\right) \approx 20 \quad (6.4)$$

which represents also the inner-limit of the region where the self similar behaviour is observed. Being different from the value for turbulent boundary layer of  $\approx 14$ , it suggests a geometry dependency.

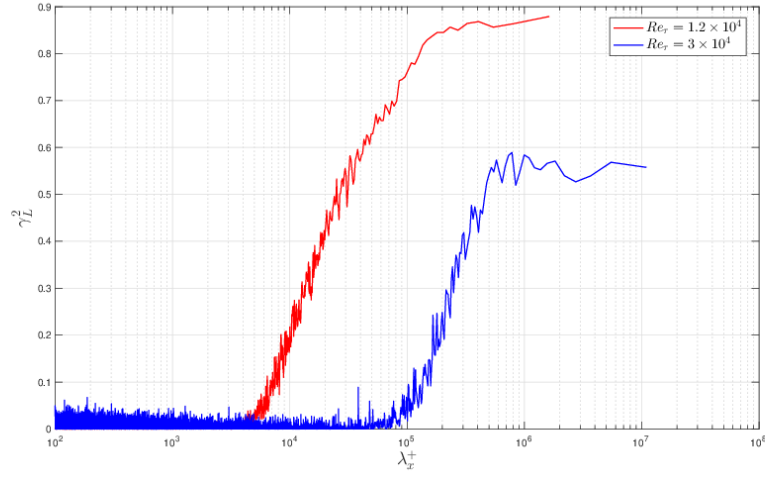


Figure 6.10:  $\gamma_L^2$  as function of inner-scaled wavelength  $\lambda_x^+$  at  $y^+ \approx 1500$  for  $Re_\tau = 1.2 \times 10^4$  and  $Re_\tau = 3 \times 10^4$ .

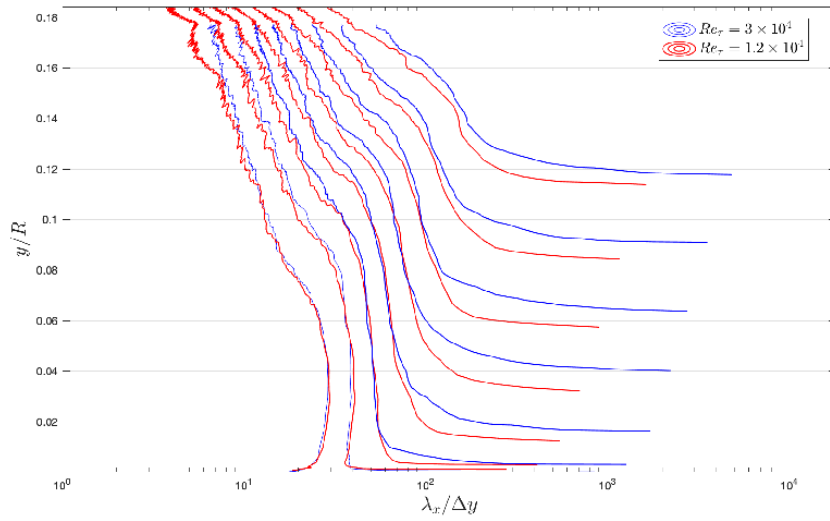


Figure 6.11: Iso-contour lines (0.1:0.1:0.9) of LCS as function of  $y/R$  and  $\lambda_x/\Delta y$  for  $Re_\tau = 1.2 \times 10^4$  (red) and  $Re_\tau = 3 \times 10^4$  (blue).



## CHAPTER 7

# Conclusions

The aim of this thesis was to investigate the phenomena related to friction for a fully developed turbulent pipe flow and expanding the knowledge on turbulent pipe flows at high Reynolds numbers. The topic is of particular interest for a vast range of industrial applications, since friction is the main responsible of energy consumption. In order to do so, three experimental campaigns were performed in the Long Pipe at the CICLoPE laboratory of University of Bologna. Thanks to its unique size, the facility guarantees accuracy so high to fully resolve all scales of turbulence using standard measurements tools. The thesis includes first the estimate and detailed uncertainty analysis of the  $\kappa_{CL}$ , a key parameter for CFD models used to predict friction, through measurements with a Pitot probe and the acquisition of static pressure drop along the pipe. Secondly, single-wire high-resolution measurements are performed at the test section to investigate the nature and dynamics of the structures responsible for friction, in the Reynolds number range  $9.9 \times 10^3$  up to  $3.9 \times 10^4$ . The main results are summarised mirroring the thesis objectives outlined in section 1.2.

- Centerline and static pressure measurements, for a range of  $Re_\tau$  from  $8.1 \times 10^3$  to  $3.9 \times 10^4$ , were performed together with a detailed uncertainty analysis to assess the statistical difference between  $\kappa$  and  $\kappa_{CL}$ . Since their value is closely related to the accuracy of the static pressure drop, we started from the empirical approach of Fiorini 2017 and conducted a systematic analysis. An iterative and robust procedure to choose the wall taps to retain in the linear fit to estimate the  $dp/dx$  is therefore performed, leading to a choice of 11 taps covering a distance of  $\approx 70m$  upstream the test section. The uncertainty analysis was based on a Monte Carlo method with two error distributions, a continuous (Gaussian and boxcar) and discrete (considering the extreme errors of the pressure transducer). If the lowest Reynolds number is dropped, considering only a regime where there is a sufficient scale separation (for  $Re_\tau > 10^4$ ), it results that for CICLoPE  $\kappa_{CL} = 0.44 \pm 0.03$ . In this case the accuracy is enough to shed light on the possible statistical difference between  $\kappa_{CL}$  and  $\kappa_{wall}$ . Interestingly enough, the range of  $\kappa_{CL} = 0.44 \pm 0.03$  includes the value of  $\kappa_{CL} = 0.438$  found by Zagarola and Smits 1998 for the Superpipe data. Despite the low uncertainty on

$u_\tau$ , solidly lower than 1% when the lowest Reynolds number is dropped, the uncertainty on  $\kappa_{CL}$  is seen to be strongly affected.

- The interaction between the small and large scales is investigated in the context of the inner-scaled streamwise velocity. The full fluctuating velocity signal is filtered into its large and small scales parts, using a spectral cut-off filter to separate the contribution to the broadband turbulence intensity of the small and large-scale structures. The value of the cut-off frequency is chosen on the basis of the work by Ganapathisubramani 2018. The present work, in line to what is showed for the boundary layers by Ganapathisubramani 2018, showed that the inner-scaled premultiplied spectra collapse after a certain frequency, that when inner-scaled is seen to be independent of the wall-distance. For the range of Reynolds numbers investigated here, from  $9.9 \times 10^3$  to  $3.9 \times 10^4$  the spectra are seen to collapse down to  $f^+ = 0.001$ . The growth of the inner peak is confirmed and linked to the linear increase large-scale' inner-peak with the logarithm of  $Re_\tau$ . As matter of facts, the inner-scaled small-scale streamwise velocity variance follows a universal scaling for the entire range of  $y^+$ , as contemplated by the classical theory. Further from the wall, in the overlap region the profile is seen to follow a logarithmic decay. A comparison with the behaviour of turbulent boundary layer, suggests that its constants are geometry dependent. In conclusion, the behaviour at the outer-peak location of the large-scale variance is related to the behaviour at the inner-peak by computing their ratio, observed to be constant at  $\approx 0.5$  for the entire range of Reynolds numbers.
- Universal, self-similar and wall-attached structures are identified in the turbulent pipe flow for a range of  $Re_\tau = 1.2 \times 10^4$  to  $Re_\tau = 3 \times 10^4$ . They are explained through the wall-attached eddies theory by Townsend in his attached eddy model. These structures are characterised by an aspect ratio of  $\approx 20$ , larger than what is observed by Baars, Hutchins, and Marusic 2016 for turbulent boundary layers. The results follow from the coherence spectra analysis from 2-point simultaneous single-wire measurements of fluctuating velocity. While one probe is fixed at  $y/R = 0.2$ , the other covers the range of wall-distances in between. This behaviour is observed in a region that is limited by  $\lambda_x/\Delta y \approx 20$ .

Overall, the results of the experimental campaigns described in this thesis give their contributions in settling some long-lasting controversies in the field, such as the universality of the von Kármán constant and the wall-attached self-similar structures in fully developed turbulent flows. Desirable future works includes the comparison with the results by Alfredsson, Örlü, and A. Segalini 2012, Klewicki, Chini, and Gibson 2017, Castro, A. Segalini, and Alfredsson 2013 on the outer peaks behaviour, by using the diagnostic plot. Moreover,

since CICLoPE is a large-scale facility, the data acquired could be used to propose a new correction scheme for the streamwise variance.





## Acknowledgements

The work presented in this thesis would have not been possible without the support of many valuable people. I now want to take the chance to express my gratitude.

First and foremost, I would like to thank my supervisor Alessandro Talamelli, who supported me and my project through the entire PhD. Thank you for the invaluable scientific teachings, the advices and the precious opportunities offered me, allowing me to grow both from the scientific and personal point of view. I will always be grateful for the opportunity to carry out my PhD in such unique facility and environment.

Thanks to Gabriele Bellani, for being a crucial and constant support during these three years. Thank you for your ever so precious encouragement, for coming up with endless ideas and for showing me how to be a scientist in and outside of the lab. Thank you for constantly motivate me to go beyond my limits, that is something I will always cherish.

Special thanks to Hassan Nagib from IIT, with whom I collaborated with and carried out a big part of the experiments whose results are presented in this thesis. Thank you for your contagious passion for science, for the unique opportunities you offered me throughout the years, for your trust and patience. Thank you for being much more than a mentor.

Thank you to professor Bharathram Ganapathisubramani, with whom not only I collaborated during part of the experimental campaign presented here, but also allowed me to work at the University of Southampton, showing me a rare example of hardwork and scientific knowledge.

I'd like to acknowledge Antonio Segalini and Francesco Picano. Their feedback was extremely helpful. Thank you to Ramis Örlü, Peter Monkewitz, Alessandro Rossetti and Andrea Cimarelli, for their help and countless advices.

Thanks to the technical staff: Ivano Amadori, Mauro Ricci and Paolo Proli, for helping me manufacturing pieces of the experimental set-ups and patiently discussing with me the most convenient and practical solution.

I would also like to acknowledge the Zonta Club. With your Amelia Earhart fellowship I was not only able to improve the quality of my research, but I met some incredible and inspiring women all around the world.

Thank you to my family. Your support and patience (*a lot*) was vital during the highs and lows of the PhD. Your constant examples of hardwork, humility and openness to always learn something from anyone, were key throughout my whole journey.

Last but not least, thank you to my friends, in particular to the girls and guys from Tecnopolo, with whom I shared the majority of my journey here. With every laugh and discussion during coffee breaks, I never felt alone, not even during the harshest of times. A special thanks goes to Luca: your unconditional support and deep understanding are definitely one-of-a-kind.

## Bibliography

- Adrian, R.J. (1979). “Conditional eddies in isotropic turbulence”. In: *The Physics of Fluids* 22.11, pp. 2065–2070.
- (2007). “Hairpin vortex organization in wall turbulence a”. In: *Physics of Fluids* 19.4, p. 041301.
- Adrian, R.J., C.D. Meinhart, and C.D. Tomkins (2000). “Vortex organization in the outer region of the turbulent boundary layer”. In: *Journal of fluid Mechanics* 422, pp. 1–54.
- Ahn, J. et al. (2015). “Direct numerical simulation of a 30R long turbulent pipe flow at  $Re_\tau = 3008$ ”. In: *Physics of Fluids* 27.6, p. 065110.
- Alfredsson, P.H. and R. Örlü (2010). “The diagnostic plot a litmus test for wall bounded turbulence data”. In: *European Journal of Mechanics-B/Fluids* 29.6, pp. 403–406.
- Alfredsson, P.H., R. Örlü, and A. Segalini (2012). “A new formulation for the streamwise turbulence intensity distribution in wall-bounded turbulent flows”. In: *European Journal of Mechanics, B/Fluids* 36, pp. 167–175.
- Baars, W.J., N. Hutchins, and I. Marusic (2016). “Spectral stochastic estimation of high-Reynolds-number wall-bounded turbulence for a refined inner-outer interaction model”. In:
- (2017). “Self-similarity of wall-attached turbulence in boundary layers”. In: *Journal of Fluid Mechanics* 823.
- Baidya, R. et al. (2019). “Simultaneous skin friction and velocity measurements in high Reynolds number pipe and boundary layer flows”. In: *Journal of Fluid Mechanics* 871, pp. 377–400.
- Bailey, S.C.C. et al. (2010). “Turbulence measurements using a nanoscale thermal anemometry probe”. In: *Journal of Fluid Mechanics* 663, pp. 160–179. DOI: 10.1017/S0022112010003447.
- Balakumar, B.J. and R.J. Adrian (2007). “Large-and very-large-scale motions in channel and boundary-layer flows”. In: *Philosophical Transactions of the Royal Society A: Mathematical, Physical and Engineering Sciences* 365.1852, pp. 665–681.
- Bendat, J. and A. Piersol (2011). *Random data: analysis and measurement procedures*. Vol. 729. John Wiley & Sons.

- Bradshaw, P. (1971). *An introduction to turbulence and its measurements*. Pergamon Press, New York.
- Bruun, Hans H (1995). *Hot-wire anemometry - principles and signal analysis*. Oxford science publications.
- Cantwell, B.J. (1981). “Organized motion in turbulent flow”. In: *Annual review of fluid mechanics* 13.1, pp. 457–515.
- (2019). “A universal velocity profile for turbulent pipe flows”. In: *J. Fluid. Mech.* 878.834-878.
- Castro, I.P., A. Segalini, and P.H. Alfredsson (2013). “Outer-layer turbulence intensities in smooth- and rough-wall boundary layers”. In: *Journal of Fluid Mechanics* 727, pp. 119–131.
- Chue, S.H. (1975). “Pressure probes for fluid measurement”. In:
- Clauser, F.H. (1954). “Turbulent boundary layers in adverse pressure gradients”. In: *J. Aero. Sci.* 21, pp. 91–108.
- Coles, D. (1956a). “The law of the wake in the turbulent boundary layer”. In: *Journal of Fluid Mechanics* 1.02, pp. 191–226.
- (1956b). “The law of the wake in the turbulent boundary layer”. In: *Journal of Fluid Mechanics* 1, pp. 191–226.
- Davidson, P.A., T.B. Nickels, and P.-Å. Krogstad (2006). “The logarithmic structure function law in wall-layer turbulence”. In: *Journal of Fluid Mechanics* 550, pp. 51–60.
- Del Álamo, J.C. and J. Jiménez (2009). “Estimation of turbulent convection velocities and corrections to Taylor’s approximation”. In: *Journal of Fluid Mechanics* 640, pp. 5–26.
- Fiorini, T. (2017). “Turbulent pipe flow - high resolution measurements in CICLoPE”. In: *PhD thesis*.
- Furuichi, N. et al. (2015). “Friction factor and mean velocity profile for pipe flow at high Reynolds numbers”. In: *Phys. Fluids* 27.9. DOI: 10.1063/1.4930987.
- Ganapathisubramani, B. (2018). “Law of the wall for small-scale streamwise turbulence intensity in high-Reynolds-number turbulent boundary layers”. In: *Physical Review Fluids* 3.10, p. 104607.
- Ganapathisubramani, B., E.K. Longmire, and I. Marusic (2003). “Characteristics of vortex packets in turbulent boundary layers”. In: *Journal of Fluid Mechanics* 478, pp. 35–46.
- Ganapathisubramani, B. et al. (2005). “Investigation of large-scale coherence in a turbulent boundary layer using two-point correlations”. In: *Journal of Fluid Mechanics* 524, pp. 57–80.
- Guala, M., S.E. Hommema, and R.J. Adrian (2006). “Large-scale and very-large-scale motions in turbulent pipe flow”. In: *Journal of Fluid Mechanics* 554, pp. 521–542.
- Head, M.R. and P. Bandyopadhyay (1981). “New aspects of turbulent boundary-layer structure”. In: *Journal of Fluid Mechanics* 107, pp. 297–338.

- Hultmark, M. et al. (2012). “Turbulent pipe flow at extreme Reynolds numbers”. In: *Phys. Rev. Lett.* 108.9. DOI: 10.1103/PhysRevLett.108.094501.
- (2013). “Logarithmic scaling of turbulence in smooth-and rough-wall pipe flow”. In: *Journal of Fluid Mechanics* 728, pp. 376–395.
- Hunt, J.C.R. and P. Carloti (2001). “Statistical Structure at the Wall of the High Reynolds Number Turbulent Boundary Layer”. In: *Flow, Turbulence and Combustion* 66.4, pp. 453–475.
- Hutchins, N. and I. Marusic (2007a). “Evidence of very long meandering features in the logarithmic region of turbulent boundary layers”. In: *Journal of Fluid Mechanics* 579, 1–=28.
- (2007b). “Large-scale influences in near-wall turbulence”. In: *Philosophical Transactions of the Royal Society A: Mathematical, Physical and Engineering Sciences* 365.1852, pp. 647–664.
- Hutchins, N. et al. (2009). “Hot-wire spatial resolution issues in wall-bounded turbulence”. In: *Journal of Fluid Mechanics* 635, pp. 103–136. DOI: 10.1017/S0022112009007721.
- Hutchins, N. et al. (2011). “Three-dimensional conditional structure of a high-Reynolds-number turbulent boundary layer”. In: *Journal of Fluid Mechanics* 673, pp. 255–285.
- Hutchins, N. et al. (2012). “Towards Reconciling the Large-Scale Structure of Turbulent Boundary Layers in the Atmosphere and Laboratory”. In: *Boundary-Layer Meteorology* 145.2, pp. 273–306.
- Jimenez, J. and A. Pinelli (1999). “The autonomous cycle of near-wall turbulence”. In: *Journal of Fluid Mechanics* 389, pp. 335–359.
- Katul, G. and B. Vidakovic (1996). “The partitioning of attached and detached eddy motion in the atmospheric surface layer using Lorentz wavelet filtering”. In: *Boundary-Layer Meteorology* 77.2, pp. 153–172.
- Kim, K.C. and R.J. Adrian (1999). “Very large-scale motion in the outer layer”. In: *Physics of Fluids* 11.2, pp. 417–422.
- Klewicki, J.C., G.P. Chini, and J.F. Gibson (2017). “Prospectus: towards the development of high-fidelity models of wall turbulence at large Reynolds number”. In: *Philosophical Transactions of the Royal Society A: Mathematical, Physical and Engineering Sciences*.
- Klewicki, J.C. and R.E. Falco (1990). “On accurately measuring statistics associated with small-scale structure in turbulent boundary layers using hot-wire probes”. In: *Journal of Fluid Mechanics* 219, pp. 119–142.
- Kline, S.J. et al. (1967). “The structure of turbulent boundary layers”. In: *Journal of Fluid Mechanics* 30.04, pp. 741–773.
- Kunkel, G.J. and I. Marusic (2006). “Study of the near-wall-turbulent region of the high-Reynolds-number boundary layer using an atmospheric flow”. In: *Journal of Fluid Mechanics* 548, pp. 375–402.

- Ligrani, P. M. and P. Bradshaw (1987). “Spatial resolution and measurement of turbulence in the viscous sublayer using subminiature hot-wire probes”. In: *Experiments in Fluids* 5.6, pp. 407–417.
- (1987). “Subminiature hot-wire sensors: Development and use”. In: *Journal of Physics E: Scientific Instruments* 20.3, pp. 323–332. DOI: 10.1088/0022-3735/20/3/019.
- Luchini, P. (June 2017). “Universality of the Turbulent Velocity Profile”. In: *Phys. Rev. Lett.* 118, p. 224501.
- Marusic, I., W.J. Baars, and N. Hutchins (2017). “Scaling of the streamwise turbulence intensity in the context of inner-outer interactions in wall turbulence”. In: *Physical Review Fluids* 2.10, p. 100502.
- Marusic, I. and G.J. Kunkel (2003). “Streamwise turbulence intensity formulation for flat-plate boundary layers”. In: *Physics of Fluids* 15.8, pp. 2461–2464.
- Marusic, I. and J.P. Monty (2019). “Attached eddy model of wall turbulence”. In: *Annual Review of Fluid Mechanics* 51, pp. 49–74.
- Marusic, I. et al. (2010). “Wall-bounded turbulent flows at high Reynolds numbers: Recent advances and key issues”. In: *Physics of Fluids* 22.6, pp. 1–24.
- Marusic, I. et al. (2013). “On the logarithmic region in wall turbulence”. In: *Journal of Fluid Mechanics* 716, R3.
- Mathis, R., N. Hutchins, and I. Marusic (2009). “Large-scale amplitude modulation of the small-scale structures in turbulent boundary layers”. In: *Journal of Fluid Mechanics* 628, pp. 311–337.
- McKeon, B.J., M.V. Zagarola, and A.J. Smits (2005). “A new friction factor relationship for fully developed pipe flow”. In: *Physics of Fluids* 538, pp. 429–443. DOI: 10.1017/S0022112005005501.
- McKeon, B.J. et al. (2004). “Further observations on the mean velocity distribution in fully developed pipe flow”. In: *Journal of Fluid Mechanics* 501, pp. 135–147.
- McNaughton, K.G. (2004). “Attached Eddies and Production Spectra in the Atmospheric Logarithmic Layer”. In: *Boundary-Layer Meteorology* 111.1, pp. 1–18.
- Miller, M.A., B. Estejab, and S.C.C. Bailey (2014). “Evaluation of hot-wire spatial filtering corrections for wall turbulence and correction for end-conduction effects.” In: *Experiments in Fluids* 55.1735.
- Millikan, C.B (1938). “A critical discussion of turbulent flows in channels and circular tubes”. In: *Proc. 5th Int. Cong. Appl. Mech.* Wiley/Chapman and Hall, New York-London, pp. 386–392.
- Monkewitz, P. A. (2017). “Revisiting the quest for a universal log-law and the role of pressure gradient in ”canonical” wall-bounded turbulent flows”. In: *Phys. Rev. Fluids* 2.

- Monkewitz, P.A., R.D. Duncan, and H.M. Nagib (2010). “Correcting hot-wire measurements of stream-wise turbulence intensity in boundary layers”. In: *Physics of Fluids* 22.9, p. 091701.
- Monty, J.P. (2005). *Developments in smooth wall turbulent duct flows*. University of Melbourne, Department of Mechanical and Manufacturing Engineering.
- Monty, J.P. et al. (2007). “Large-scale features in turbulent pipe and channel flows”. In: *Journal of Fluid Mechanics* 589, pp. 147–156.
- Mouri, H. (2017). “Two-point correlation in wall turbulence according to the attached-eddy hypothesis”. In: *Journal of Fluid Mechanics* 821, pp. 343–357. ISSN: 1469-7645.
- Nagib, H.M. and K.A. Chauhan (2008). “Variations of von Kármán coefficient in canonical flows”. In: *Physics of Fluids* 20.10. DOI: 10.1063/1.3006423.
- Nagib, H.M. et al. (2017). “Centerline Kármán ‘constant’ revisited and contrasted to log-layer Kármán constant at CICLoPE”. In:
- Örlü, R. (2009). “Experimental studies in jet flows and zero pressure-gradient turbulent boundary layers”. PhD thesis. KTH.
- Örlü, R., J.H.M. Fransson, and P.H. Alfredsson (2010). “On near wall measurements of wall bounded flows - the necessity of an accurate determination of the wall position”. In: *Progress in Aerospace Sciences* 46.8, pp. 353–387.
- Örlü, R. et al. (2017). “Reynolds stress scaling in pipe flow turbulence—first results from CICLoPE”. In: *Phil. Trans. R. Soc. A* 375.2089, p. 20160187.
- Perry, A.E. and C.J. Abell (1977). “Asymptotic similarity of turbulence structures in smooth-and rough-walled pipes”. In: *Journal of Fluid Mechanics* 79.04, pp. 785–799.
- Perry, A.E., S. Henbest, and M.S. Chong (1986). “A theoretical and experimental study of wall turbulence”. In: *Journal of Fluid Mechanics* 165, pp. 163–199.
- Pope, S.B. (2001). *Turbulent flows*.
- Prandtl, L. (1925). “Bericht über untersuchungen zur ausgebildeten turbulenz”. In:
- Romano, G.P. (1995). “Analysis of two-point velocity measurements in near-wall flows”. In: *Experiments in Fluids* 20.2, pp. 68–83.
- Schoppa, W. and F. Hussain (2002). “Coherent structure generation in near-wall turbulence”. In: *Journal of fluid Mechanics* 453, pp. 57–108.
- Segalini, A. et al. (2011). “Effect of the spatial filtering and alignment error of hot-wire probes in a wall-bounded turbulent flow”. In: *Measurement Science and Technology* 22.10, p. 105408.
- Segalini A. and Örlü, R. et al. (2011). “A method to estimate turbulence intensity and transverse Taylor microscale in turbulent flows from spatially averaged hot-wire data”. In: *Experiments in Fluids* 3.51, pp. 693–700.

- Smits, A.J., B.J. McKeon, and I. Marusic (2011). “High-Reynolds number wall turbulence”. In: *Annu. Rev. Fluid Mech.* 43, cited By 171, pp. 353–375. DOI: 10.1146/annurev-fluid-122109-160753.
- Smits, A.J. et al. (2011). “Spatial resolution correction for wall-bounded turbulence measurements”. In: *J. Fluid Mech.* 676, pp. 41–53. DOI: 10.1017/jfm.2011.19.
- Talamelli, A. et al. (2009). “CICLoPE - A response to the need for high Reynolds number experiments”. In: *Fluid Dynamics Research* 41.2. DOI: 10.1088/0169-5983/41/2/021407.
- Theodorsen, T. (1952). “Mechanism of turbulence”. In: *Proceedings of the Second Midwestern Conference on Fluid Mechanics*. Vol. 1719. Ohio State University.
- Tomkins, C.D. and R.J. Adrian (2003). “Spanwise structure and scale growth in turbulent boundary layers”. In: *Journal of Fluid Mechanics* 490, pp. 37–74.
- Townsend, A.A. (1976). *The structure of turbulent shear flow*. Cambridge university press.
- Tutkun, M. et al. (2009). “Two-point correlations in high Reynolds number flat plate turbulent boundary layers”. In: *Journal of Turbulence* 10, N21.
- Vallikivi, M., B. Ganapathisubramani, and A.J. Smits (2015). “Spectral scaling in boundary layers and pipes at very high Reynolds numbers”. In: *Journal of Fluid Mechanics* 771, pp. 303–326. DOI: 10.1017/jfm.2015.181.
- Willert, C.E. et al. (2017). “Near-wall statistics of a turbulent pipe flow at shear Reynolds numbers up to 40 000”. In: *Journal of Fluid Mechanics* 826, R5.
- Woodcock, J.D. and I. Marusic (2015). “The statistical behaviour of attached eddies”. In: *Physics of Fluids* 27.1, p. 015104.
- Wu, X. and P. Moin (2009). “Direct numerical simulation of turbulence in a nominally zero-pressure-gradient flat-plate boundary layer”. In: *Journal of Fluid Mechanics* 630, pp. 5–41.
- Wyngaard, J.C. (1968). “Measurement of small-scale turbulence structure with hot wires”. In: *Journal of Physics E: Scientific Instruments* 1.11, p. 1105.
- Zagarola, M.V. and A.J. Smits (1998). “Mean-flow scaling of turbulent pipe flow”. In: *Journal of Fluid Mechanics* 373, pp. 33–79.
- Zagarola, M.V. et al. (1996). “Experiments in high Reynolds number turbulent pipe flow”. In: *AIAA paper* 96-0654.
- Zanoun, E.-S., F. Durst, and H.M. Nagib (2003). “Evaluating the law of the wall in two-dimensional fully developed turbulent channel flows”. In: *Physics of Fluids* 15.10, pp. 3079–3089.
- Zúñiga Zamalloa, C. et al. (2014). “Spectral analogues of the law of the wall, the defect law and the log law”. In: *Journal of Fluid Mechanics* 757, pp. 498–513.